

Electronic Theses and Dissertations, 2004-2019

2015

Evaporative Vapor Deposition for Depositing 2D Materials

Kevin Gleason
University of Central Florida

 Part of the [Aerodynamics and Fluid Mechanics Commons](#)
Find similar works at: <https://stars.library.ucf.edu/etd>
University of Central Florida Libraries <http://library.ucf.edu>

This Masters Thesis (Open Access) is brought to you for free and open access by STARS. It has been accepted for inclusion in Electronic Theses and Dissertations, 2004-2019 by an authorized administrator of STARS. For more information, please contact STARS@ucf.edu.

STARS Citation

Gleason, Kevin, "Evaporative Vapor Deposition for Depositing 2D Materials" (2015). *Electronic Theses and Dissertations, 2004-2019*. 1422.
<https://stars.library.ucf.edu/etd/1422>

EVAPORATIVE VAPOR DEPOSITION FOR DEPOSITING 2D MATERIALS

by

KEVIN GLEASON
B.S. University of Central Florida, 2014

A thesis submitted in partial fulfillment of the requirements
for the degree of Master of Science
in the Department of Mechanical and Aerospace Engineering
in the College of Engineering and Computer Science
at the University of Central Florida
Orlando, Florida

Spring Term
2015

Major Professor: Shawn A. Putnam

© 2015 Kevin Gleason

ABSTRACT

The development of a new deposition technique called evaporative vapor deposition (EVD) is reported, allowing deposition and formation of atomically-thin, large area materials on arbitrary substrates. This work focuses on the highly popular monolayer material – graphene oxide (GO). A droplet of a GO solution is formed on a heated polymer substrate, and maintained at steady-state evaporation (all droplet parameters are held constant over time). The polymer substrate is laser patterned to control the droplet’s contact line dynamics and the droplet’s contact angle is maintained using a computer controlled syringe pump. A room temperature silicon wafer is translated through the vapor field of the evaporating GO droplet using a computer controlled translation stage. Dropwise condensation formed on the silicon wafer is monitored using both optical and infrared cameras. The condensation rate is measured to be $\sim 50\text{pL}/\text{mm}^2\cdot\text{s} - 500\text{pL}/\text{mm}^2\cdot\text{s}$ and dependent on the substrate translation speed and height difference between the droplet’s apex and substrate surface. Nano-sized GO flakes carried through the vapor phase are captured in the condensate, depositing on the translating wafer. Deposition rate is dependent on the stability of the solution and droplet condensate size. Characterization with Raman spectroscopy show expected shifts for graphene/graphite. The presented EVD technique is promising toward formation of large scale 2D materials with applications to developing new technologies.

ACKNOWLEDGMENTS

I cannot express my appreciation for all the support, encouragement, and knowledge my adviser, Dr. Shawn Putnam, has provided me. I am grateful for his excellent mentorship and guidance toward my academic success and the achievements I have received over the past years. As humble as he may be, the quality of all of his students outline his ability to train us all how to approach our research and produce great work. I look forward to future collaborations with him as I continue my degree at Yale.

I must acknowledge Shashank Saraf for his collaboration on this work. I am in debt to the help he provided me with preparing the graphene oxide solutions. With this, I must extend my gratitude to Dr. Sudipta Seal and the Advanced Materials Processing and Analysis Center (AMPAC) for the support on this work. Additionally, I must thank Richard Stadelmann and Dr. Nina Orlovskaya from the Department of Mechanical and Aerospace Engineering for granting me access to their Raman equipment.

I would also like to thank my thesis committee members Dr. Weiwei Deng and Dr. Lei Zhai, for their time and support. My thesis work greatly benefited from their ideas and recommendations.

I wish the best luck to all my labmates. Michael Jasiukowicz and Jaime Benavente, as we worked on the NASA project, both taught me more than they are aware of. Richard ‘Josh’ Murdock, whose astonishing success at UCF will surely carry through as he continues his academics at MIT/Harvard. As Mehrdad Mehrvand and Harish Voota finish up their degree here at UCF, I appreciate their collaboration and communication over the years.

Additional thanks to all my friends, family, and classmates; all who unknowingly contributed to my success. Lastly, thanks to the Department of Mechanical and Aerospace Engineering, Burnett Honors College, and the Office of Undergraduate Research for the

opportunities, support, funding, and guidance they all provided me throughout both my Honors in the Major undergraduate and Master's theses.

TABLE OF CONTENTS

LIST OF FIGURES	ix
LIST OF TABLES	xi
NOMENCLATURE	xii
CHAPTER 1: INTRODUCTION	1
1.1 Background	1
1.2 Research Focus and Motivation	2
CHAPTER 2: LITERARY REVIEW	4
2.1 First Production of Graphene	5
2.2 The Search for Methods of Fabrication	7
2.2.1 Chemical Exfoliation	7
2.2.1.1 Graphene Oxide	8
2.2.1.2 Reduced Graphene Oxide	9
2.2.2 Chemical Vapor Deposition	10
2.2.3 Liquid Exfoliation and Additional Methods	10
2.3 Properties of Graphene and Graphene Oxide	12
2.3.1 Electron Mobility	13
2.3.1.1 Functionalized Graphene	13
2.3.2 Thermal Properties	14
2.3.3 Raman Spectroscopy	15
2.4 The Liquid Meniscus	18
2.4.1 Heat and Mass Transfer	19
2.4.2 Material Deposition and Pattern Production	20

CHAPTER 3: STEADY STATE DROPLET EVAPORATION	22
3.1 Methodology	22
3.1.1 Substrate Fabrication	23
3.1.2 Droplet Evaporation Measurements	24
3.2 Steady State Evaporation Measurements	25
3.2.1 Controlling the Contact Line	26
3.2.2 Controlling the Contact Angle	28
3.3 Results for Steady State Droplet Evaporation	29
CHAPTER 4: VAPOR DEPOSITION OF GRAPHENE OXIDE	32
4.1 Methodology	32
4.1.1 Solution Preparation	33
4.1.2 Experimental Setup	34
4.1.3 EVD Procedure	35
4.2 Controlled Condensation Rates	36
4.2.1 Effect of Substrate Position on Droplet Evaporation Rates	37
4.2.2 Speed and Height Dependence on Condensation Rates	39
4.3 Raman Scans for Deposition Detection	42
4.3.1 Analysis of Graphene Visibility on Si/SiO ₂	43
4.3.2 Drop Casting for Baseline Reference	46
4.3.3 Results for Evaporative Vapor Deposition	49
4.3.3.1 Null Experiment with Deionized Water	50
4.3.3.2 Graphene Deposition	50
4.3.4 Raman Scans for Depth Testing	52
CHAPTER 5: IMPROVEMENTS IN VAPOR DEPOSITION	56
5.1 Laser Etching Silicon Wafers for Deposition ROI	56

5.2	New GO Solution for Increased Stability	58
5.3	Multi-Step Deposition Process on Single Substrate	60
5.4	Importance of Deposition Substrate Heat Sink	61
5.5	Re-evaluation of Condensation Rates Versus Substrate Height	63
5.6	Improved Deposition Results	66
CHAPTER 6: CONCLUSIONS		69
6.1	Overview	69
6.2	Future Work	70
REFERENCES		73

LIST OF FIGURES

Figure 2.1: Graphene atomic structure in relation to CNT and graphite.	5
Figure 2.2: Capillary flow in an evaporating droplet forming the coffee-ring effect.	11
Figure 2.3: Eigenvectors of graphene resulting in Raman activity.	16
Figure 2.4: Characteristics of Raman scans for determining graphene thickness.	18
Figure 3.1: Procedure for laser patterning polymer acrylic substrates.	23
Figure 3.2: Experimental setup used for droplet evaporation studies.	25
Figure 3.3: Modes of droplet evaporation on a horizontal substrate.	26
Figure 3.4: Effectiveness in controlling a droplets contact line dynamics.	28
Figure 3.5: Reproducibility in maintaining steady state evaporation.	30
Figure 4.1: Stability of GO in water, experiencing agglomeration over time.	33
Figure 4.2: Experiment setup for evaporative vapor deposition.	35
Figure 4.3: Deposition substrate position's effect on droplet evaporation rate.	38
Figure 4.4: Height and speed dependence on condensation formation.	40
Figure 4.5: Images captured during an EVD experiment.	41
Figure 4.6: Refractive indices of Si and SiO ₂	44
Figure 4.7: Visibility of monolayer graphene for various SiO ₂ thicknesses.	46
Figure 4.8: Drop casting deposition technique for benchmark Raman scans.	47
Figure 4.9: Raman scans to determine the quality of the deposited GO.	49
Figure 4.10: Results of an EVD experiment.	51
Figure 4.11: Raman scans at different focal distances showing changes in intensity.	53
Figure 4.12: Results for determining thickness of EVD deposited GO.	55
Figure 5.1: Laser patterning Si wafers for a defined ROI during deposition.	57

Figure 5.2: Stability of GO solution with sulfite functionalization.	59
Figure 5.3: Multi-speed deposition for range of material thickness on single wafer.	61
Figure 5.4: Heat sink inclusion to maintain wafer at room temperature	62
Figure 5.5: Image analysis procedure for measuring condensation rates	64
Figure 5.6: Substrate height dependence on condensation rate.	65
Figure 5.7: Improved deposition with a highly stable GO dispersion.	67
Figure 5.8: More dispersed, less concentrated deposition of GO within ROI. . . .	68

LIST OF TABLES

Table 4.1	Overview of various solutions prepared throughout this work.	32
-----------	--	----

NOMENCLATURE

A	Area
h	Apex Height
i	Imaginary Number ($\sqrt{-1}$)
l_c	Capillary Length
\dot{m}_{evap}	Evaporation Rate
\dot{m}_{pump}	Syringe Pump Infuse Rate
n	Refractive Index
R	Contact Radius
T	Temperature
T_s	Substrate Temperature
t	Thickness
V	Volume
W	Watts
z	Height

Greek

γ	Surface Tension
Δ	Difference/Change in
κ	Thermal Conductivity
λ	Wavelength
θ	Contact Angle

Acronyms

<i>n</i> D	<i>n</i> -Dimensional
AFM	Atomic Force Microscopy
CCA	Constant Contact Angle
CCR	Constant Contact Radius
CNT	Carbon Nanotube
CVD	Chemical Vapor Deposition
DI	Deionized
EVD	Evaporative Vapor Deposition
FLG	Few Layer Graphene
GO	Graphene Oxide
G _t O	Graphite Oxide
HOPG	Highly Oriented Pyrolytic Graphite
IR	Infrared
MWCNT	Multi Wall Carbon Nanotube
PVA	Polyvinyl Alcohol
RGO	Reduced Graphene Oxide
ROI	Region of Interest
SEM	Scanning Electron Microscopy
SWCNT	Single Wall Carbon Nanotubes
TEM	Transmission Electron Microscopy
TMD	Transition Metal Dichalogenides
XPS	X-ray Photoelectric Spectroscopy

CHAPTER 1: INTRODUCTION

1.1. Background

Since its first experimental discovery in 2004, the production and characterization of graphene (along with other two-dimensional crystal materials) are a high interest research topic. To introduce, graphene is a single atom thick layer of carbon atoms; the building block for other carbon based materials such as carbon nanotubes (a *rolled-up* graphene sheet), fullerenes or buckyballs (a *sphere* of graphene), and graphite (a *stack* or *cluster* of graphene). While graphene gets the most publicity (presumably due to its electron mobility capabilities and various quantum phenomena [1]), other 2D materials such transition metal dichalcogenides (e.g., MoS₂ & WSe₂), metal halides (e.g., MoCl₂ & CrCl₃), among others [2] all open a new field of condensed-matter physics due to their unique properties compared to its bulk equivalent. Researchers have remained optimistic in the progression toward applications implementing the unique properties of these 2D materials, yet the greatest hindrance is their lack of reliable production.

Despite the current low-yield production methods, graphene research has made significant development over a ~ 10 year period. Experimental results showed graphene with electron mobilities as high as $200,000\text{cm}^2/\text{V}\cdot\text{s}$ [3], thermal conductivity nearing $5,000\text{W}/\text{m}\cdot\text{K}$ [4], and an elastic modulus over 1000GPa [5]. These astonishing properties lead to the seemingly limitless applications of graphene (or graphene based materials) including: (1) supercapacitors, (2) energy storage, (3) improvements in thermal management, (4) diverse composite materials, (5) high accuracy gas sensors, (6) polymer composites, etc. For example, high fidelity sensors are important for tracking both biological and chemical contamination in a launch vehicle (i.e., rocket) during assembly and launch [6, 7]. Monolayer graphene [8] and MoS₂

[9] have shown extreme sensitivity to various gas exposures (able to detect single molecules [10]). Beyond space mission contamination, such sensors can improve the safety of persons working with highly toxic chemicals by ensuring no leaks into the environment or determining concentration of gases in harsh environments not suitable for most equipment (such as inside a combustion chamber). The immense abilities 2D materials have demonstrated led researchers across a wide range of disciplines to further explore them.

1.2. Research Focus and Motivation

As mentioned, the greatest limitation and frustration in current 2D material research is the lack of idealized fabrication techniques. The simplest technique, mechanical exfoliation, produces high quality, pristine crystals; yet is extremely low yield with no scalability. This method includes the ‘scotch tape’ method (a repeated adhesion-peeling procedure with adhesive tape) used to first discover graphene in stable form [11]. Also, this method is extremely tedious (one can easily rationalize) and requires a lot of effort to simply determine if any graphene (or other 2D material) is present. Chemical treatments propose methods for large scale production of wafer sized 2D materials, but tends to strip their unique unrivaled properties such as electron mobility [12]. Chemical Vapor Deposition (CVD) is the currently the most promising for industrializing 2D materials. Although, due to the high temperatures needed for CVD ($\sim 1000^\circ\text{C}$), material deposition is limited to specific substrates that can withstand such temperatures (typically, copper or nickel) [13]. Additionally, some surface functionalities of these 2D materials may be lost at high temperatures, thus further mitigating the advances of CVD techniques. Liquid exfoliation opens low temperature techniques such as drop casting and dip coating, yet non-uniform deposition is inevitable due to droplet capillary flow and substrate surface imperfections leading to the production of the *coffee-ring* effect.

The work in this thesis is directed to developing a new deposition technique, with advantages over current methods. Liquid exfoliated solutions can be synthesized for producing a large quantity of monolayer graphene through light ultrasonication, yet current liquid deposition techniques are not able to produce films with a uniform thickness (thus not able to form large scale monolayer materials on substrates). The proposed hypothesis to overcome this pattern production is to avoid the liquid meniscus (i.e., the solid-liquid-vapor contact line) which results in the non-uniform deposition. Additionally, if 2D materials can be ‘grown’ from *vaporized* materials (i.e., CVD), why would this not occur for an *evaporated* solution? It is hypothesized that the vapor phase of a solution (e.g., water) will carry a solvent (e.g., graphene) provided the particle is small enough. Evaporating a solution versus vaporizing a solid materials significantly lowers the deposition temperature ($\sim 1000^\circ\text{C}$ to $< 100^\circ\text{C}$), thus allow deposition to any substrate. Combining these hypotheses, the proposed work in this thesis presents the ability to deposit 2D materials transported in the vapor phase of an evaporated nanofluid. This proposed technique allows for low temperature deposition of 2D materials utilizing liquid exfoliated solutions with no restrictions/limitations to the substrate the material is being deposited to. The particle size deposited is limited to the maximum the vapor phase can carry (a single vapor molecule is not believed to have the energy to transport materials much larger/heavier than the vapor molecule itself), thus avoiding non-uniform deposits of thicker/larger particles. Importantly, the proposed thesis work is easily scalable for advances in large scale production of 2D materials in the industry.

CHAPTER 2: LITERARY REVIEW

Graphene has a relatively small history prior to 2004, when the first experimental study of graphene was reported [11]. Early theoretical studies [14, 15] looked at single layers of graphite to explain various anisotropic properties. For example, the atomic spacing between atoms is 1.42\AA (in-plane, \parallel) and 3.37\AA (out-of-plane, \perp), so planar interactions may be disregarded in some cases. This approximation showed the electrical conductivity between the two directions orders of magnitudes different [14]. It was believed that any single atomically thin material is thermodynamically unstable, and will form into a curved structures (e.g., CNTs and fullerenes). Proceeding its discovery, it is still debated whether single graphene layers become intrinsically stable by ‘crumpling’ (i.e., wave-like; the surface of the ocean on a semi-calm day) [1].

From past theorists, large two-dimensional crystalline structures were believed to be thermodynamically unstable [16, 17]. The instability is caused by the thermal fluctuations in 2D crystals which are comparable to the atomic length scale. Thus, unstable atomically thin layers will decompose [1] or stabilize by forming into a three-dimensional structures (e.g., CNTs, fullerenes, or soot) shown in Fig. 2.1 [1, 11]. While fullerenes may be discussed as 0D, and CNTs as quasi-1D, they are undoubtedly a 3D structure. Epitaxial growth of single atomic layers has been demonstrated [18, 19], but these single layers are stabilized as being a part of the bulk material [1]. Thus, these atomic layers were not considered to disprove the instability of monolayers. Graphene’s simple experimental existence created an enormous spark of interest, which continued to expand following the astonishing properties monolayer materials exhibit toward a wide range of applications.

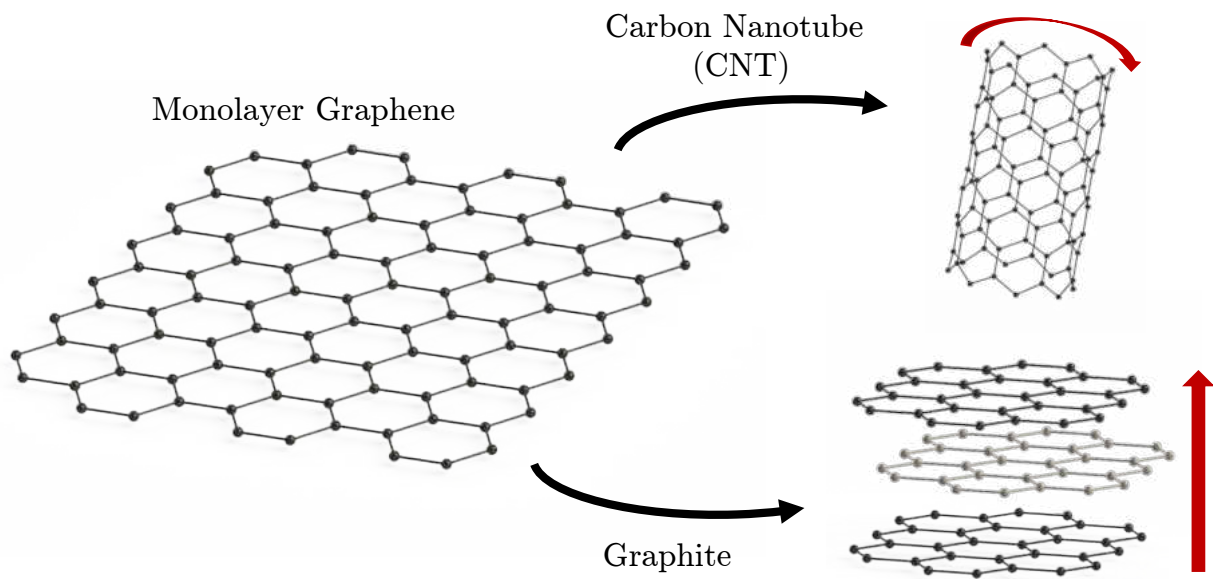


Figure 2.1: Visual representation of monolayer graphene with hexagonal carbon structure. Other common carbon allotropes include CNTs, which may be considered a *rolled-up* graphene sheet, and graphite, planar stacking of individual sheets of graphene in ABA... order.

2.1. First Production of Graphene

In a bit of a surprise, Konstantin Novoselov, Andre Geim, and coworkers have found the first two dimensional material through a relatively elementary technique [11]. Not only were monolayer 2D crystals found, but were of high quality. Through repetitions of mechanical exfoliation (peeling) of highly oriented pyrolytic graphite (HOPG), the graphite sheets were peeled apart to obtain sheets atomically thin. With a small mesa-like sample of HOPG, scotch tape was used to peel graphite flakes from the surface (in less academic terms, this method is referred to as the ‘Scotch Tape’ method). The flakes were transferred to a silicon wafer by dipping in an acetone solution. The thinnest flakes (typically less than 10nm) had a stronger adhesion to the wafer due to van der Waals forces, thus only the larger flakes were wash away into the solution. The stability of 2D crystals may still be argued to exist only in a meta-stable state having been extracted from a 3D material, and remain in small

sizes. Although, Geim and Novoselov [1] argue the thermal fluctuations may be relaxed for larger crystal dimensions though slight crumbling (i.e., exhibiting a wave-like surface) [20]. The monolayer graphene flakes were viewed using various techniques including: (1) optical microscope, (2) atomic force microscopy (AFM), (3) scanning electron microscopy (SEM), and (4) transmission electron microscopy (TEM). While this method may be portrayed as a trial and error process, it has shown to produce high quality monolayer flakes as large as $10\mu\text{m}$ (with ‘few layer’ graphene sizes of $\sim 100\mu\text{m}$).

One possible explanation for the lack of graphene (or any atomically thin materials) prior to 2004 may be because it was simply overlooked, not by its instability to other 3D structures as theorized. Summarized briefly by Novoselov and Geim [11], few layer graphene (FLG) is completely invisible in an optical microscope. Using a 300nm SiO_2 wafer, discolorations on the surface were a result of shifted light based on the flakes thickness. Different graphene flake thicknesses were detectable based on the color (e.g., blue was $\sim 4\text{nm} - 10\text{nm}$ and white/light blue was $\gtrsim 50\text{nm}$). Additionally, FLG flakes are rare with the mechanical exfoliation technique and can easily be missed being surrounded by larger graphite flakes [1]. Even so, 1-5 layer graphene films are $\lesssim 2\text{nm}$ and remained optically invisible. Monolayers were easily identifiable in AFM and SEM images, and found when comparing these images and noticing features that become detected. A later study by Blake et al. [21] overviewed the contrast of graphene for a range of SiO_2 thicknesses, reporting the importance of the thickness of SiO_2 for optical viewing. For example, under white light, FLG can be visible on 300nm SiO_2 yet completely invisible on 200nm SiO_2 . The maximum contrast was shown at SiO_2 thickness of $\sim 90\text{nm}$, although the standard remains 300nm (which still exhibits reasonable contrast). Nevertheless, the delayed discovery comes as no surprise having been optically transparent on most substrates.

2.2. The Search for Methods of Fabrication

Proceeding the success of mechanical exfoliation for producing graphene monolayers, a wide range of alternatives are sought for reliable large scale production [22]. Researchers have remained optimistic in the progression toward applications implementing the unique properties of these 2D materials, yet remain hindered to fabrication techniques. The simplest technique, mechanical exfoliation, produces high quality, pristine crystals; yet is extremely low yield with no scalability. Chemical treatments propose methods for large scale production of wafer sized 2D materials, but tends to strip the unique unrivaled properties of 2D materials such as electron mobility. Chemical Vapor Deposition (CVD) is the currently the most promising for industrializing 2D materials. Although, due to the high temperatures needed for CVD ($\sim 1000^{\circ}\text{C}$), material deposition is limited to specific substrates that can withstand such temperatures. Additionally, some surface functionalities of these 2D materials may be lost at high temperatures, thus further mitigating the advances of CVD techniques. Liquid exfoliation opens low temperature techniques such as drop casting and dip coating, yet non-uniform deposition is inevitable due to droplet capillary flow and substrate surface imperfections leading to the production of the coffee-ring effect. Each technique has its advantages and disadvantages. This section overviews how each of these techniques developed, and the efforts to control/minimize their limitations.

2.2.1. Chemical Exfoliation

Chemical exfoliation involves intercalating graphite with bulk molecules (i.e., creating a structure with a sequence of ABABA...). With intervened molecules, the intercalated graphite can be agitated to separate the graphene layers [23, 24]. Early attempts were not able to obtain free-standing graphene using chemical exfoliation because of the uncontrollable characteristics [1]. Although, the agitation technique remains the key for large scale

production because of the weak out-of-plane attraction forces of graphite allow for easy separation (based on up-to-date methods [2]). One example involves the intercalate element of potassium, which synthesized results in either KC_8 or KC_{24} [24] and exfoliated with ethanol. This method left nanoscrolls of graphite that were ~ 50 layers thick. Other methods of exfoliation include thermal expansion of sulfuric acid (as an intercalation compound), although also lack the complete separation of individual sheets (consisting of $\gtrsim 100$ layers) [12]. The most successful chemical treatment involves oxygen functionalized graphite, where a mild sonication treatment can exfoliate individual sheets. [25–30].

2.2.1.1. Graphene Oxide

Stankovich et al. [12, 28, 31] found graphene sheets exfoliated from graphite to be difficult and lacked reproducibility. Thus, a new route for graphene from exfoliated graphite oxide (G_tO) had risen and demonstrated high potential toward large scale production [12, 25, 28, 29]. Graphite oxide is an oxygenated treatment of graphite, functionalized with hydroxide, epoxide, ether, carboxylic acid, among others (the exact structure remains debated [32–35]). Typically, graphite oxide is produced through a treatment named the Hummers method [36] (or a modified Hummers method [37]). The details of these processes are not discussed in this work. Importantly, the resulting functionalized graphite becomes hydrophilic. The hydrophilicity allows easy intercalation of water molecules, thus graphene oxide (GO) nanosheets (including monolayers) can be exfoliated through sonication of a G_tO -water solution. Additives have shown to increase the stability of the GO dispersion, remaining well dispersed for months [26, 31, 38].

The addition of functional groups is expected to increase the thickness of monolayer GO, measuring larger than pristine graphene. Stankovich et al. [12] measured GO sheets of $\sim 1\text{nm}$ with ATM (compared to 0.34nm for pristine graphene), and believed these to be atomically

thin. The increase in thickness is attributed to the presence of oxygen covalent bonds causing an out-of-plane displacement of sp^3 hybridized carbon atoms. Paredes et al. [26] studied the dispersion and stability of GO in various organic solvents in addition to water. Good dispersions were achieved for a numerous solvents, with some remaining stable for up to three weeks. High polarity solvents also resulted in good dispersions, although the factors inducing long term stability were unclear. Monolayer dispersions of GO in aqueous solutions show potential for nanofillers and polymer matrix nanocomposites, leading to further efforts in synthesis techniques to increase compatibility with polymers [26, 39, 40].

2.2.1.2. Reduced Graphene Oxide

Unfortunately the interesting properties of monolayer graphene are lost when graphene is functionalized (e.g., becoming electrically insulating). Post-exfoliation treatments can reduce the functionalization, becoming reduced graphene oxide (RGO). These treatments have shown to partially restore the lost properties due to functionalization, although cannot compete with pristine graphene [12]. Additionally, the sheets have formed a large number of defects undergoing this post-treatment [41]. While the additional step for obtaining RGO allows for more versatile nanosheets, the hydrophilicity property is also lost when de-functionalized. Thus, water-based solutions of RGO have a high tendency to agglomerate (irreversibly). Stability can be maintained by polymer-coated nanoplatelets [31], or exfoliation in polar aprotic solvents [28]. Nevertheless, the high-throughput technique for FLG-like RGO and its edge functionalities keeps its a high interest material for applications toward electromechanical and biological sensors [42–44].

2.2.2. Chemical Vapor Deposition

The most successful technique for large scale production of graphene is through chemical vapor deposition (CVD). To brief, the CVD process involves precipitation of carbon on a metal substrate in a high temperature ($\sim 1000^\circ\text{C}$) vacuum environment. A rapid quenching causes the precipitated carbon atoms to form graphene layers. The cooling rate and carbon concentration control the quality and thickness of deposited graphene [22, 45, 46]. This fabrication technique has shown to be reproducible and produce high crystalline films centimeters in lateral dimension. [13, 47].

Li et al. [13] produced uniform graphene sheets as large as 1cm^2 grown on thin copper films using a CVD technique. The copper was beneficial over nickel (a commonly used base substrate) because the growth on copper is self-limiting. Therefore, extending the exposure to CVD did not result in multiple layer graphene growth (i.e., remaining monolayer). In the case of nickel as the base substrate, thicker graphitic layers are known to form [46, 47]. As a result, the experimental process and cooling rate strongly dictate the number of graphene layers and quality (i.e., amount of defects) [46]. Kim et al. [47] grew cm^2 -sized graphene sheets on nickel, although the flake sizes remained small and had folding defects. Chae et al. [45] had similar issues with wrinkle formation, having to search for ‘optimal’ exposure temperatures and Acetylene/Hydrogen concentrations for FLG. Nevertheless, the resulting sheets grown on nickel are easily etched or stamped onto arbitrary substrates [47, 48]; also demonstrating high quality thermal, electrical and mechanical properties [47, 49].

2.2.3. Liquid Exfoliation and Additional Methods

Other work has been put forth for simple, reproducible, and large scale production of graphene. Using the hydrophilicity of GO, methods of deposition using a liquid exfoliated solution (typically from ultrasonication) remains a growing focus [50]. Versatility remains

crucial, thus seeking various solvents (beyond water) and additives for well dispersed and exfoliated nanosheets [26, 31, 40, 51]. This theory of liquid exfoliation is applicable to any layered materials with strong (weak) in-plane (out-of-plane) bonds [2]. Other than graphene, examples of layered materials that may be separated into single nanosheets include transition metal dichalcogenides (TMDs) such as molybdenum disulfide (MoS_2) and tungsten diselenium (WSe_2). These 2D TMDs, however, are not single atomic thick sheets due to their atomic structure (e.g., exhibiting ABA ABA ABA... structures) [44]. While graphene holds the highest popularity (partly due to being the first monolayer material experimentally measured), all 2D materials hold very unique properties over bulk (3D) materials. Potential applications of 2D materials (beyond graphene) include polymer-based composites, electronics, and transistors, among many others [2, 28].

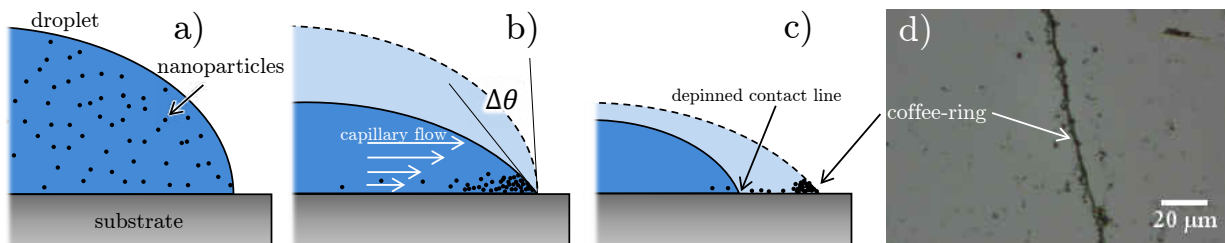


Figure 2.2: Drawing showing the effect on capillary flow on nanoparticle suspensions in an evaporating droplet. The nanoparticles in an evaporating droplet, (a), will be driven toward the droplets contact line by the capillary flow, (b), as the contact line remains pinned. Once the contact line depins, (c), the nanoparticles remain deposited on the substrate in a large collection, (c), while few are deposited with a moving contact line, (c) and (d).

With liquid exfoliated monolayer dispersions, various deposition techniques including: (1) drop casting, (2) dip coating, (3) spin coating and (4) Langmuir techniques (Langmuir-Blodgett and Langmuir-Schaefer) have been attempted to produce large-scale monolayers materials [29, 44, 52–54]. Drop casting and dip coating both utilize evaporation of the solvent, where the solute (e.g., graphene or other nanoparticles) remains on the substrate.

Deposition of uniform films remains a challenge due to the capillary flow of an evaporation fluid directing the solute to the contact line (solid-liquid-vapor interface), termed ‘coffee-ring effect’ (see Fig. 2.2 [55]). This phenomenon is still under investigation [56–59]. Kim et al. [53] used the Langmuir-Blodgett technique (i.e., a vertical deposition), and found that larger graphene flakes tend to migrate toward the liquid-vapor interface while the smaller flakes sank. This size-dependent amphiphilicity allowed separation based on flake size, where deposition of smaller flakes led to a more uniform film. Shih et al. [54] also reported a separation method using the coffee-ring effect. Smaller flakes were more influenced by the capillary flow, depositing at the contact line. The larger flakes were found along inner rings. Monolayer and FLG can be found within the coffee-ring, but scalability remains a hurdle.

Another method is based on the well-established CNT growth [60–62]. Production of CNTs, which can be viewed simply as *rolled up* graphene sheets, is more well-known and understood than graphene. Finding ways of cutting open or unzipping CNTs may benefit significantly from the large quantity of past research on CNTs. While this production is more controllable, the electrical quality of unzipped CNTs still lack compared to pristine, mechanically exfoliated graphene [60].

2.3. Properties of Graphene and Graphene Oxide

A large contribution to the production of monolayer materials is due to the astonishing properties they exhibit. Interestingly, these unique properties are largely maintained with the addition of a second layer. Therefore, there must be a thickness limit which separates 2D materials from 3D. Partoens and Peeters [63] sought this 2D to 3D transition based on the electronic structure. To no surprise, there is no deterministic transition between 2D graphene and 3D graphite. Although, it was adapted that this transition is 10 layers as the electronic structure of 11+ layers are within 10% of bulk graphite [63]. Therefore, *graphene*

may be referred as $\lesssim 10$ layers (although typically termed graphene, bi-, tri- and few-layer graphene for 1, 2, 3, and 4-10 layers thick, respectively). Since its experimental discovery in 2004, a significant amount of research has been done regarding various properties of graphene including electrical, mechanical, thermal, among others.

2.3.1. Electron Mobility

The electrical conductivity, related to the electron mobility, is astonishing for isolated graphene flakes. This was predicted due to graphite (stacks of graphene) having strongly anisotropic electrical properties [14]. Bolotin et al. [3] reported electron mobility of elevated monolayer graphene as high as $230,000\text{cm}^2/\text{V}\cdot\text{s}$. While suspended devices always exhibit high mobilities, exceptional values ($\sim 2000 - 10,000\text{cm}^2/\text{V}\cdot\text{s}$) are commonly reported [11, 13, 47, 64–66]. Although, due to 2D scattering for planar graphene, ‘1D’ CNTs and some semiconductors tend to have higher mobilities ($15,000 - 60,000\text{cm}^2/\text{V}\cdot\text{s}$ and $\sim 77,000\text{cm}^2/\text{V}\cdot\text{s}$, respectively) [1, 11].

Beyond mechanical exfoliation, the process of producing graphene strip the electrical properties. As a result, a large focus remains on production of graphene while maintaining high quality crystals in hopes of approaching similar properties of pristine graphene. CVD grown graphene on nickel, transferred to arbitrary substrates, have reported values of $2000 - 4000\text{cm}^2/\text{V}\cdot\text{s}$ [47, 64]. Cao et al. [64] explained that wrinkling/folding resulted in lower values. Lower temperatures (near 0K) allow for higher values of $\sim 4000\text{cm}^2/\text{V}\cdot\text{s}$ [47]. Li et al. [13], found slightly higher values $4050\text{cm}^2/\text{V}\cdot\text{s}$ with CVD on copper foils.

2.3.1.1. Functionalized Graphene

While production of functionalized graphene (i.e., GO) has progressed significantly, the large interest in monolayer is lost becoming electrically insulating. Although, further treat-

ment of these functionalized graphene materials (i.e., GO becoming RGO) partially restores to graphene-like properties. Electron mobility have reported values of $\sim 0.01 - 10 \text{cm}^2/\text{V}\cdot\text{s}$ [67, 68]. Shih et al. [54] measured values as high as $400 \text{cm}^2/\text{V}\cdot\text{s}$ with bi- and tri-layer graphene flakes exfoliated in iodine halogen solutions. While this cannot compete with pristine graphene, it demonstrates a potential future for GO/RGO monolayer fabrication techniques.

2.3.2. Thermal Properties

Following the high thermal conductivity (κ) of carbon allotropes (CNTs and diamond), measured values of monolayer graphene come at no surprise. Elevated graphene have values within $3000 \text{W}/\text{mK}$ and $5000 \text{W}/\text{mK}$ (the upper limit is higher than the accepted values for CNTs, yet still significantly trailing diamond) [4, 69], although is reduced to $\sim 600 \text{W}/\text{mK}$ when supported [70]. All carbon allotropes all demonstrate the highest thermal conductivity, due to the strength of carbon-carbon bonds [70]. The κ - T relation was investigated by Seol et al. [70], finding that the maximum peak of pyrolytic graphite (nearing $3000 \text{W}/\text{mK}$) is at $T \approx 140 \text{K}$, while supported graphene at a higher temperature of $T \approx 300 \text{K}$ (with conductivity of $\sim 600 \text{W}/\text{mK}$). Therefore, the reduction in conductivity (based on photons) is attributed to the interactions of the substrate. Additionally, the thermal properties of functionalized graphene are orders of magnitude lower [71], as with the electrical properties.

Koh et al. [72] reviewed the temperature and thickness of graphene thermal conductance. For 1-10 layers of graphene, the measured thermal conductance remained constant. Meaning, the heat transport remains governed by the substrate/graphene interface even for monolayer ($\sim 0.4 \text{nm}$ thick) materials (i.e., remains distinctive). Koh et al. have a disagreement in the κ - T relation, reporting nearly constant conductance over $50 \text{K} \leq T \leq 500 \text{K}$, while Seol et al. found a decreasing κ for $T \lesssim 150 \text{K}$ [70]. Although, similar conclusions are made regarding

the substrate interference in photon interactions, limiting the conduction rate. Concluding, while graphene has outstanding thermal properties and could be a top choice for thermal management devices, the heat conduction is limited by the graphene/substrate interface.

2.3.3. Raman Spectroscopy

While production of graphene is of high interest, the physical detection of graphene and knowledge of the number of graphene layers under study remained difficult yet crucial. From theory, the thickness of a monolayer graphene (as well as FLG) is known. AFM has the ability to measure thicknesses of $\sim 0.4\text{nm}$ (the thickness of monolayer graphene), but not practical to scan large, cm^2 -sized regions. Optical imaging was found to be assisted with oxidized Si wafers (SiO_2) [65], but still remains a difficult challenge and can easily be overlooked. TEM, while excellent for imaging down to the lattice structure [73], is a destructive technique. Raman spectroscopy was found to display subtle yet unique shifts based on the number of graphene layers [74–76], and thus became a quick technique for measuring/detecting graphene.

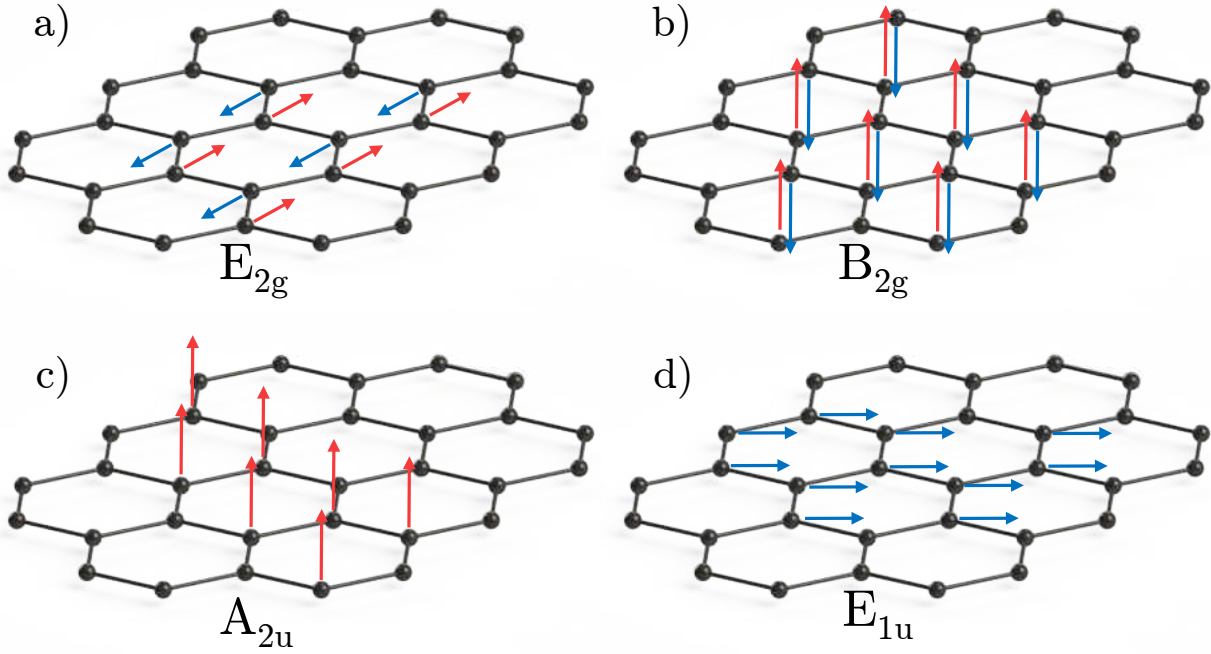


Figure 2.3: Various vibrational modes (eigenvectors) of graphene/graphite. Optical vibrations are shown in (a) and (b), and planar translations are in (c) and (d). The E_{2g} is the only Raman active mode, resulting in first-order and second-order Raman shifts at $\sim 1580\text{cm}^{-1}$ and $\sim 2750\text{cm}^{-1}$, respectively.

To overview, atoms/molecules gain energy from interaction to light causing them to vibrate. The vibrational modes cause a photon energy shift (termed *Raman Scattering*), and these shifts are measured. The collection of shifts provide insight on the components in the material. The vibrational modes (eigenvectors) of graphene are demonstrated in Fig. 2.3. The E_{2g} and B_{2g} eigenvectors (Figs. 2.3a and 2.3b, respectively) are optical vibrations while the A_{2u} and E_{1u} eigenvectors are planar translations (Figs. 2.3c and 2.3d, respectively). Only the E_{2g} mode is Raman active, giving a first-order peak at $\sim 1580\text{cm}^{-1}$ and second-order peak at $\sim 2750\text{cm}^{-1}$ [77]. These peaks are the G-band and 2D-band (or G') peaks, respectively. The A_{1g} mode (in-crystal-plane longitudinal acoustic vibrations) is thought to be the reason for a third peak at $\sim 1350\text{cm}^{-1}$ shift (named the D-band peak) [78], though this was found to be present for graphene with defects/disorder (e.g., GO with oxygen functionalized carbon or holes in the lattice structure from missing carbon atoms) [76, 77]. The D-band peak is

also present due to edge effects [78]. Thus, the intensity of the D peak is an identification to the quality/defect density of the graphene crystal.

From the properties of carbon (graphene/graphite), Raman scans not only detects the presence of graphene on a substrate by observation of the G and 2D peaks but the crystalline quality as well. While the crystalline quality is important, knowing the thickness or number of layers is necessary when characterizing the properties of graphene and FLG. Over the years, subtle yet distinctive Raman peak qualities were identified for unambiguous identification of graphene layers [74–76, 79], and outlined in Fig. 2.4. When comparing the G-band peak for graphene layers $1 \leq n \leq 10+$, a slight downshift in peak frequency was observed as the number of layers increased (a $3\text{-}6\text{cm}^{-1}$ difference between monolayer and HOPG) [74, 75]. This decrease in frequency follows a linear trend relative to the inverse number of graphene layers, $1/n$. The 2D-band shape is more sensitive to the number of layers [74–76], as shown in Fig. 2.4. Once established, a simple observation of the 2D-band may be sufficient to determine the number of layers. Other methods include comparing the relative intensity of the G-band and 2D-band [64], the G-band and the Raman shift from Si/SiO₂ substrate [76], or the D' band at $\sim 1600\text{cm}^{-1}$ (which merges with the characteristic G-band) [80].

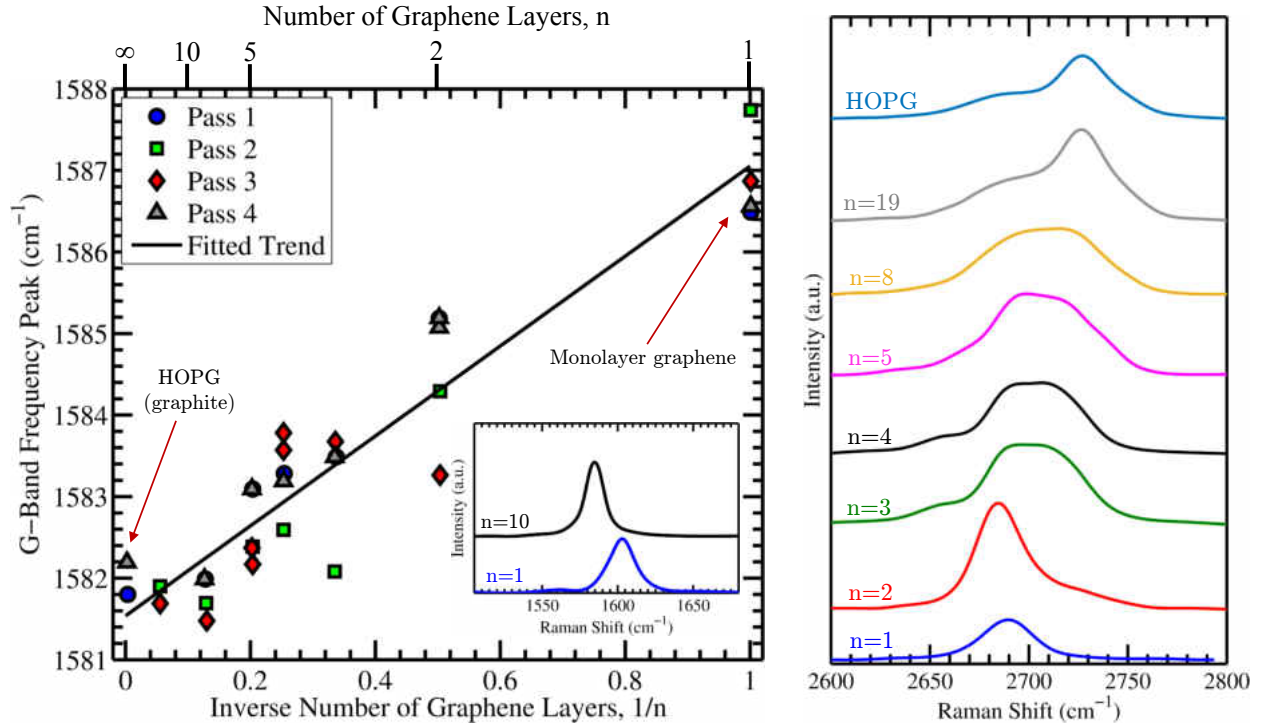


Figure 2.4: The G-band frequency is a method of detecting the number of graphene layers, slightly decreasing by $5\text{-}6\text{cm}^{-1}$ as the number of layers increases from 1 to >10 (i.e., graphite). The 2D-band shape is another a clear indicator for determine the number of graphene layers. Figure adapted from Refs. [75, 76].

2.4. The Liquid Meniscus

Slightly diverging from the history and production/characterization of graphene, this section will review various aspects of engineering the liquid meniscus. The liquid meniscus is the curved liquid-vapor interface that is formed when the liquid is in contact with a solid, dictated by surface tension forces (i.e., Young-Laplace equation [81]). The liquid meniscus plays an important role in engineering applications such as heat and mass transport [82], direct material deposition [44, 52], and pattern formation [55, 83]. A review on the multiphase phenomenon that occurs in relation to the liquid meniscus, and how various small-scale engineering applications (e.g., deposition of graphene presented in this thesis) manipulate/exploit them.

Liquid meniscus engineering is very common in microfluidics, leading toward the development of Micro-total analysis systems (μ TAS) and Lab-on-a-chip (LOC) devices [84, 85]. For example, applied electric fields can alter the surface tension forces [86] or electrostatic pressure in the vicinity of the solid-liquid-vapor contact line [87]. These applied forces can cause deformations in the liquid meniscus, or manipulate entire droplets under higher electric fields [88]. Further applications of manipulating the liquid meniscus includes self-cleaning surfaces [89]. Making a surface superhydrophobic (water repelling), droplets easily capture particles on the surface with minimal adhesion forces (i.e., easily removed/washed off); termed the *Lotus effect*. In the reverse, this electrical energy contained in a fluid can be extracted and used for energy harvesting [90].

2.4.1. Heat and Mass Transfer

Small droplets have a high interest in thermal sciences, able to extract high heat fluxes. It is reported that a droplet's thermal resistance at the liquid-vapor interface is 10-50 times greater than at the solid-liquid interface (i.e., near the contact line) [91]. Pioneer work by Wayner and coworkers [82, 92, 93] report the evaporation characteristics and heat flux along the liquid meniscus, splitting the meniscus into three regions: (1) absorbed film, where a liquid film (nanometer thick) is absorbed into the solid and no evaporation occurs; (2) thin-film/transition, where maximum evaporation and heat flux occurs; and (3) bulk/thick meniscus, where the curvature becomes nearly constant, with increasing thermal resistance and decreasing heat flux and evaporation rate. This suggests that increasing the contact line (i.e., the thin-film transition region where maximum evaporation/heat flux occurs) while reducing a droplets surface area (i.e., the bulk meniscus) is crucial for enhancing heat removal in evaporation based cooling systems [94]. This hypothesis is well supported with the numerous studies on effectiveness in spray cooling, where tiny droplets cover a surface to be

cooled [95, 96]. Studying single droplets, it has been shown that the droplets evaporation rate efficiency decreases with decreasing contact line length [94, 97]. Although, a droplets evaporation rate is proportional to a droplets total surface area (i.e., the total liquid-vapor interface) [97], the contact line length dictates the phase-change transfer rates.

2.4.2. Material Deposition and Pattern Production

Liquid exfoliated graphene (or any other 2D materials) became a simple method for obtaining monolayer materials, but has its limitations like every production technique. Through the work by Deegan et al. [55, 98], the *coffee-ring* effect has become well known and studied [56–59]. Methods for controlling/mitigating this non-uniform deposition include anisotropic particles [59] or nano-structured surfaces [56]; although some experiments do not have this option (e.g., EVD of graphene in this thesis cannot be replaced with other anisotropic shaped nanoparticles). One hypothesis to mitigate the coffee-ring formation is to force a receding contact line. For example, if the liquid meniscus were extended (by pulling the contact line away from the bulk fluid), surface tension forces will pull the contact line into a favorable/equilibrium position. By increasing the liquid meniscus length (effectively, ‘thinning’ out), particles cannot collect and will remain loosely packed and deposit more uniformly [59]. By ‘engineering’ the dip coating method, evaporation rate and meniscus extensions can be controlled to form uniform depositions of 2D materials [44, 52].

Early successors of dip coating monolayer materials was reported by Liu et al. [44], depositing another highly popular 2D material – molybdenum disulfide (MoS_2). A pre-heated Si wafer was vertically dipped in an ammonium thiomolybdates $[(\text{NH}_4)_2\text{MoS}_4]$ solution. The deposited material thickness was controlled by the substrate temperature (therefore, the evaporation rate) and the pulling speed (i.e., the liquid meniscus extension length). After thermal decomposition, the deposit was reduced to MoS_2 . Homogeneous deposition of

trilayer was achieved, with sparse bilayers. Various characterizations (e.g., Raman, XPS, and electron mobility) concluded this thermolysis dip coating process produced highly crystalline MoS₂, comparable to mechanical exfoliation, that is simple and scalable. Recent work by Jeon et al. [52] showed uniform deposition of GO with a horizontal dip coating technique, which was found to be applicable for various other materials as well [99]. Focusing on the film thickness (i.e., the extended liquid meniscus) which can be tuned with the substrate translation speed and solutions capillary number, uniform depositions were comparable to spin coating. With a AFM measured thickness of 4nm, the deposition was determined to be 3-4 graphene layers thick.

Efforts in engineering the liquid meniscus expand beyond thin film deposition – specifically, pattern production in biomedical applications [83]. Using uniquely helical shaped macromolecule phage (bacterial virus), Chung et al. [83] reported a dip coating process that replicated natural formation of tissue. The liquid meniscus evaporating in a stick-slip mode led to twisted structures, aligning perpendicular to the pull direction when the meniscus is pinned and parallel when in motion. The pull speed is found to control formation of single spiraling ‘fingers’ to tightly packed nanofilaments. This self-templating pattern production can be fabricated for a variety of applications in biomedical materials and tissue engineering. It is believed that the stick-slip mechanism resulting in the non-uniform deposits (i.e., coffee-ring effect) [100]. While some work has shown to mitigate these effects, the famous ‘no-slip condition’ in fluid mechanics [101] along with all real surfaces exhibiting some nano-scale surface roughness cause this behavior. This has led to the hypothesis that uniform deposition of 2D materials (on a large scale) will never be ideal. Thus, the formation of the research presented in this thesis on depositing 2D materials from the liquid phase without engineering the liquid meniscus.

CHAPTER 3: STEADY STATE DROPLET EVAPORATION

Steady state droplet evaporation is defined as a droplet that is controlled such that all its parameters (contact radius R , contact angle θ , apex height h , and volume V) remain constant. A droplet may be assumed spherical in shape, provided the radius of the droplet (i.e., the characteristic length) remains less than the capillary length (for water, $l_c \approx 2.7\text{mm}$). Therefore, through spherical geometric relations, the droplet is fully defined by only two parameters. For this study, the contact radius and apex height are measured directly using a custom LabVIEW code [94]. The contact angle and droplet volume are calculated using Eq. (3.1).

$$V = \frac{\pi h}{6}(3R^2 + h^2) = \frac{\pi R^3}{3 \sin^3 \theta}(2 - 3 \cos \theta + \cos^3 \theta) \quad (3.1)$$

The experimental setup mimics previous studies [102, 103]. A substrate is laser patterned to restrict motion of a droplets contact line, providing a predetermined contact line length and area. Additionally, a fluid channel is created within the substrate to form droplets using a bottom-up methodology. This allows precise control of the droplets volume (as well as contact angle and apex height) throughout the experiment without affecting the evaporation rate. Based on numerical modeling [104], the evaporation rate (\dot{m}_{evap}) for a droplet evaporating with a constant contact radius may be accurately predicted. Therefore, once a droplet is formed, the pump infuse rate (\dot{m}_{pump}) is set to equal the predicted evaporation rate (i.e., $\dot{m}_{\text{pump}} = \dot{m}_{\text{evap}}$) to maintain a constant volume steady state evaporating droplet.

3.1. Methodology

The following studies detail the substrate fabrication technique, its exceptional ability to control the contact line dynamics during evaporation and ability to maintain steady state

droplet evaporation over extended periods of time. Steady state droplet evaporation is important toward uniform deposition of materials (discussed later), by maintaining a steady vapor convection field surrounding the droplet.

3.1.1. Substrate Fabrication

A polymer acrylic substrate (1in. diameter) is used for all droplet evaporation studies. First the substrate surface is painted with an opaque thin film (for a future step, the laser ablation process) as shown in Fig. 3.1b. Next, a fluid channel is created within the substrate through a two-step drilling process, using a custom micro-drill press. A $\sim 500\mu\text{m}$ in diameter channel is drilled perpendicular to the surface normal of the substrate (from one edge to the center of the substrate). This channel is made large enough to insert a stainless steel syringe needle. A second channel ($200\mu\text{m}$ in diameter) is created normal to the substrate surface (intersecting the horizontal channel). This channel is represented in Fig. 3.1c. Importantly, the microfluid channel is drilled post-application of the opaque film to avoid contamination within the channel during the films application.

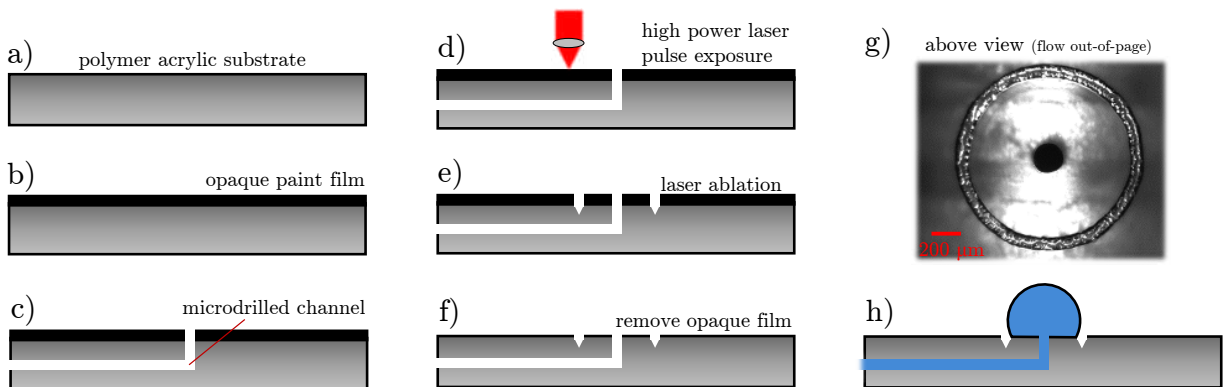


Figure 3.1: Procedure used to fabricate substrates used for steady state droplet evaporation. The surface of a clear polymer acrylic substrate (a) is painted with a black opaque film (b). A two step drilling process creates an inner substrate fluid channel (c). The substrate is mounted to a motorized translation stage and exposed to high powered laser pulses (d), causing the substrate to ablate (e). The opaque paint is chemically removed (f). An image of a fabricated substrate (g) and demonstrating its application (h).

The substrate is placed on a motorized (2D) translation stage, and a custom LabVIEW code ‘prints’ the desired circular trench shape onto the substrate (concentric with the micro drilled hole, shown in Fig. 3.1g.). To detail, a simple grey-scale image is imported into the code, and the motorized stage translates the substrate following the imported shape. When the substrate is in position, the substrate is exposed to a short femtosecond laser pulse (140fs pulse width at 80MHz, with a power of ~ 1.7 Watts) to ‘print’ each pixel from the imported image. Because the acrylic substrate is transparent, an opaque film is applied to the surface to absorb the laser. The high powered laser focused to $\sim 50\mu\text{m}$ in diameter spot size acts as an extreme heat source, causing the substrate to ablate (vaporize) under exposure (see Figs. 3.1d and 3.1e). Parameters such as the opaque film thickness, laser power, and exposure duration determine the size of the ablated spot. Although, increased exposure or higher laser power may cause the acrylic substrate to deform/melt in the surrounding area due to heat conduction. For typical substrate patterning, an exposure of $500\mu\text{s}$ provided a spot size of $\sim 50\mu\text{m}$. Once the pattern is printed on the substrate, the painted film is chemically removed and the substrate is cleaned with ethanol to remove any remaining debris.

3.1.2. Droplet Evaporation Measurements

An overview of the experimental setup used for all droplet evaporation studies is shown in Fig. 3.2. A glass syringe ($100\mu\text{L}$) placed on a syringe pump facilitates the supply fluid to the substrate through a stainless steel needle inserted into the substrate. The substrate is placed on a 100Ω electric heater to heat the substrate, and its temperature is maintained using a temperature controller. A custom LabVIEW code operates for data collection [94, 103]. An *in-situ* optical camera captures images of the droplet, and an image analysis is performed to determine the droplets parameters based on a spherical curve fit of the droplets liquid-vapor interface. The optical imaging setup includes a line-replaceable Mitutoyo objective for high

magnification ($2\times$, $5\times$, and $20\times$ magnifications provide $6.76\mu\text{m}/\text{pixel}$, $2.71\mu\text{m}/\text{pixel}$, and $0.675\mu\text{m}/\text{pixel}$ respectively). The code also allows the user to control the syringe pump flow rate, within $0.04\text{nL}/\text{s}$ and $\sim 3000\text{nL}/\text{s}$ with accuracy of $0.03\text{nL}/\text{s}$.

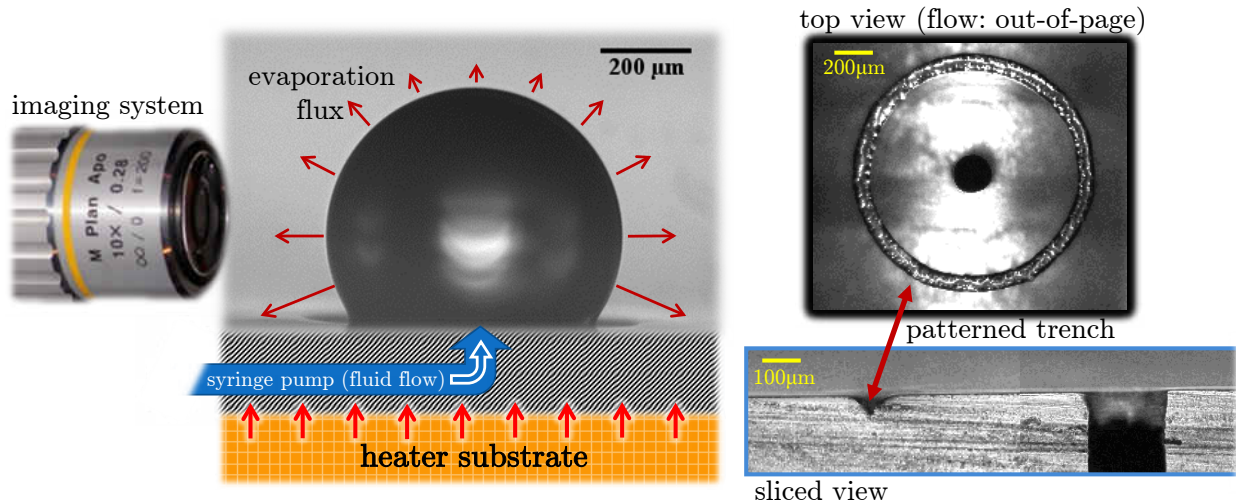


Figure 3.2: Experimental setup used for droplet evaporation studies on a heated substrate. The droplet formed on the laser pattern substrate is illustrated further from Fig. 3.1. A sliced view (cut substrate) shows the depth caused by the ablation process.

3.2. Steady State Evaporation Measurements

A droplet evaporating on a horizontal substrate (termed *sessile droplet*) is characterized by the dynamics of the contact line. The three common modes include: (i) constant contact radius (CCR), experiencing a decreasing contact angle; (ii) constant contact angle (CCA), with a moving contact line; and (iii) mixed mode, which is simply a combination of the other two modes. A fourth mode is occasionally discussed, where an oscillations between a CCR mode and a rapid decreasing in contact radius (a *depinning* contact line, causing a rapid increase in contact angle) and termed ‘stick-slip’ [105–107]. Each of these modes are shown in Fig. 3.3, along with experimental data showing each mode of evaporation. Microdroplets are a high interest in thermal management applications due to their ability to remove large

heat fluxes [94, 103, 108]. Therefore, tracking the contact line dynamics remains at high interest, yet the challenge of predicting the transition between each mode of evaporation remains [107, 109].

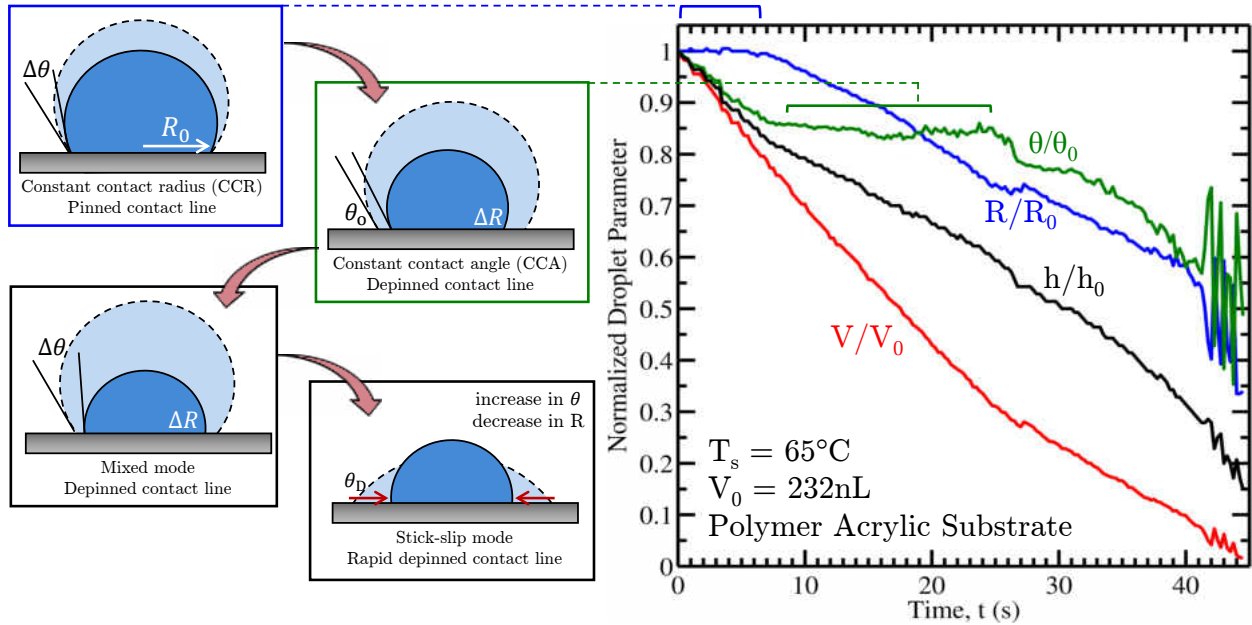


Figure 3.3: Representation of a droplet evaporating on a polymer substrate, heated to 65°C. Drawings represent the various modes of contact line dynamics that are present during periods of an evaporating droplet.

3.2.1. Controlling the Contact Line

The laser patterned trench on the substrate surface acts as a barrier, restricting further advancement of a moving contact line. It is known that surface roughness attributes to droplet experiencing a CCR mode of evaporation [110–112]. The laser patterned trench acts as a significantly rough region to keep the contact line pinned at a desired length for an extended period of time. Therefore, each experiment performed maintains identical contact line length and area for systematic comparisons between each data set. No effect on

evaporation rate is expected for the characteristic length scale of the trench in the following experiments based on the Knudsen number order of magnitude analysis [102].

A droplet on a flat surface will exhibit a contact angle based on the surface tension forces of the solid-liquid-vapor environment as predicted by Young’s equation [81],

$$\gamma_{sv} = \gamma_{sl} + \gamma_{lv} \cos \theta. \quad (3.2)$$

For the polymer acrylic substrates used throughout this study, the experimentally measured contact angle of pure deionized water is $72 \pm 1^\circ$. The patterned trench pins the contact line to allow larger contact angles (which would cause an advancing contact line due to the surface tensions forces in Eq. (3.2)). Additionally, once the contact line comes in contact with the trench, the strong pinning forces allow for contact angles less than the equilibrium (which would normally cause a receding contact line per Eq. (3.2)).

Figure 3.4 illustrates this, showing contact angles of $22^\circ \lesssim \theta \lesssim 145^\circ$. Shown complimentary, are experimental results of droplet evaporation with a fixed contact area and length. When comparing Figs. 3.3 and 3.4d, the latter shows significant improvement toward simplifying the contact line dynamics during evaporation, and allows for accurate predictions. While the upper and lower bounds of this range can be unstable (based on the quality of the pattern produced), this methodology demonstrates its exceptional abilities to control the contact line dynamics

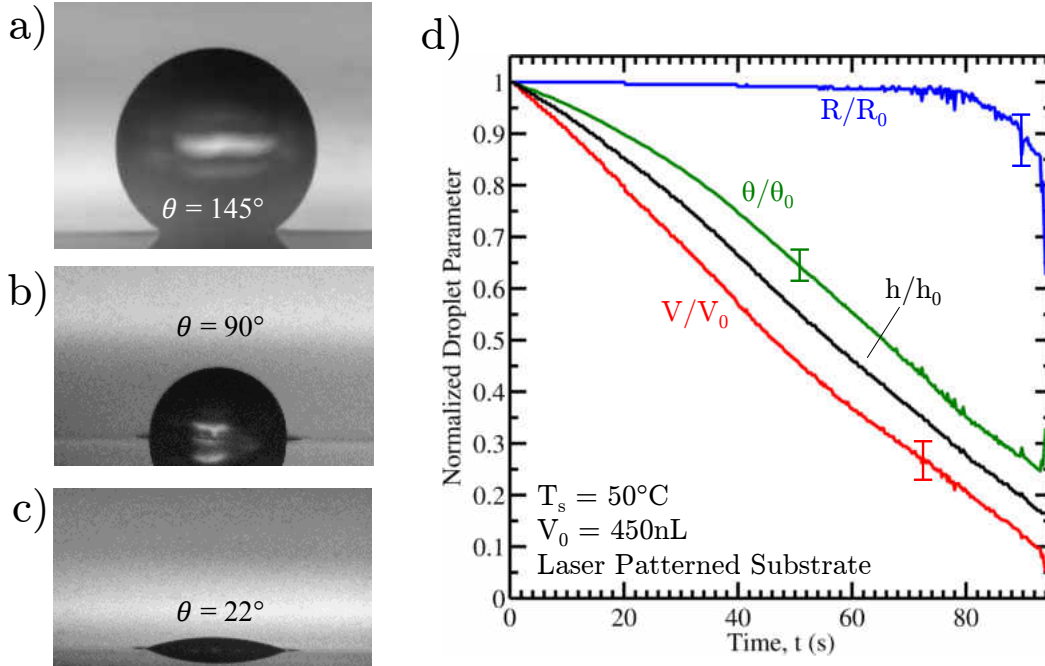


Figure 3.4: The laser patterned substrate demonstrates exceptional abilities to control the contact line. Contact angles of $22^\circ \lesssim \theta \lesssim 145^\circ$ can be achieved with a fixed contact line length and contact area, shown in (a)-(c). The contact line remains pinned for a majority of an evaporating droplets lifetime, shown in (d). Error bars represent largest deviation of five experiments.

3.2.2. Controlling the Contact Angle

Experiments of static, sessile droplets and the dynamics of the contact line during evaporation have demonstrated the accurate control of the contact line with the patterned substrate. As previously mentioned, only two droplet parameters are necessary to fully define a droplets geometry (see Eq. (3.1)). Therefore, controlling the contact angle with a pinned contact line necessarily fixes the droplets apex height and volume. Implementing the inner substrate fluid channel, a ‘bottom-up’ method to form the droplets on the substrate allows fluid to be continuously added to a droplet. Because the fluid is being fed through the solid-liquid interface, the evaporation rate is not effected (as the evaporation can only occur at the liquid-vapor interface. Additionally, past studies show that the inner region of the solid-liquid interface (i.e., not the contact line) has no influence on the droplet [113].

As the contact line remains fixed at a predetermined length, the amount of fluid supplied to form the droplet dictates what the contact angle will be. So, while the volume of the droplet is actually controlled (therefore, defining the contact angle and apex height), it is customary to discuss the contact angle a droplet exhibits (in addition to the dynamics experienced during evaporation). Therefore, the amount of fluid supplied to the droplet is presented as the method from controlling the contact angle and the droplets volume is the parameter that becomes fixed.

3.3. Results for Steady State Droplet Evaporation

To confirm the ability to form well controlled droplet to a predetermined contact angle (where the contact line lengths is defined by the patterned substrate), three tests were performed to form a droplet with a contact angle of $\theta \cong 109 \pm 1^\circ$ and maintain steady state droplet evaporation at $T_s = 60^\circ\text{C}$. The patterned substrate has a pattern radius of $R \approx 1200\mu\text{m}$, thus the droplet volume is maintained at $\sim 2.4\mu\text{L}$. A high infuse rate is used to quickly form the droplet, which is near a factor of 10 greater than the predicted evaporation rate ($\dot{m}_{\text{pump}} \approx 10\dot{m}_{\text{evap}}$). For a droplet heated to $T_s = 60^\circ\text{C}$ and contact radius of $R \approx 1200\mu\text{m}$ is predicted to have an evaporation rate of $\sim 14\text{nL/s}$ [104]. Therefore an infuse rate of $\dot{m}_{\text{pump}} = 100\text{nL/s}$ is used. This infuse rate is sufficient enough to overcome the evaporation rate and form the droplet with the desired contact angle, $\theta = 109^\circ$, within ~ 30 seconds.

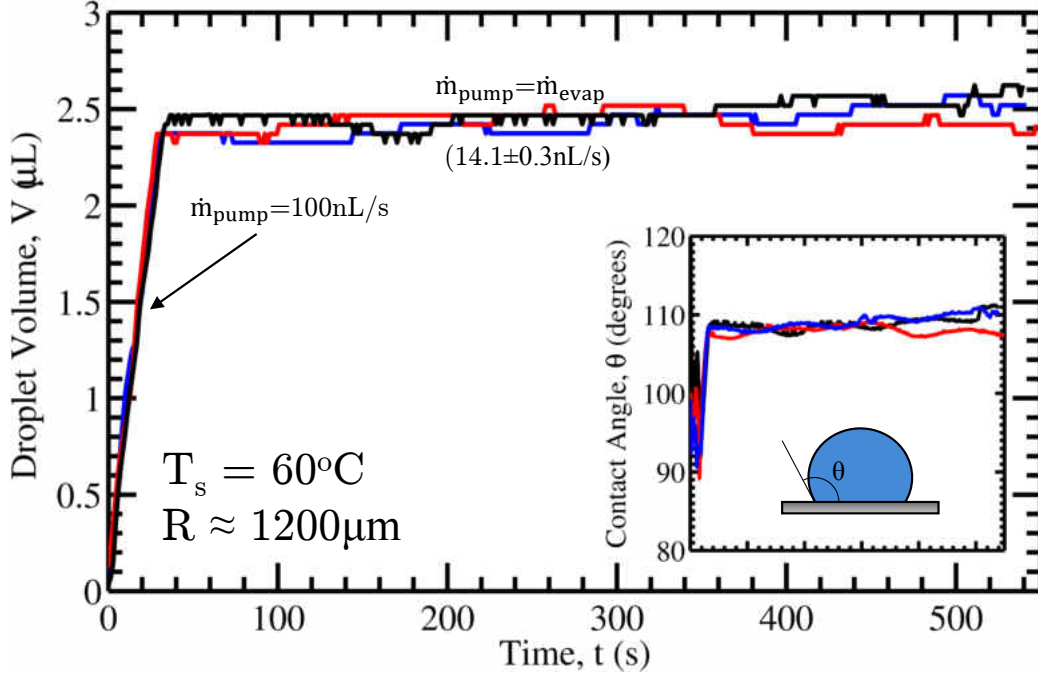


Figure 3.5: Three identical experiments are performed, forming a droplet with an infuse rate of $\dot{m}_{\text{pump}}=100\text{nL/s}$. Once the droplet reached a desired condition ($V \cong 2.5\mu\text{L}$), the pump flow rate was reduced to match the predicted evaporation rate ($\dot{m}_{\text{evap}}=14.1\pm 0.3\text{nL/s}$). Accuracy to achieve the desired steady state condition and reproducibility of steady state evaporation demonstrated.

The formation and steady-state evaporation results for three identical experiments are shown in Fig. 3.5. The volume of the droplet is kept at $2.45\pm 0.15\mu\text{L}$ (i.e., volume fluctuations are within 6%), where each colored line (black, blue, and red) represent a different test. The inset shown in Fig. 3.5 also shows the measured contact angle throughout each experiment (color legends are identical to the volume data). Through a slight trial and error process, the stability of a steady state evaporating droplet with an infuse rate of $14.1\pm 0.3\text{nL/s}$ maintains a steady state droplet ($R \approx 1200\mu\text{m}$, $\theta = 109\pm 1^\circ$). Numerical models [104] are used to get within a reasonable range of the evaporation rate. A few experiments are performed to adjust to a slightly lower (higher) evaporation rate experienced, causing an increasing (decreasing) droplet volume over time. The ability to accurately form droplets of a desired contact angle, and the reproducibility in these experiments are demonstrated well.

For the focus of this thesis, where a graphene oxide solution (with water as the solvent) is used, these results remain relevant. Graphene oxide has reports of surface energy of 62.1 mJ/m² [114, 115] (near water at 72mJ/m²); small concentrations are not expected to have a major effect on the surface tension/energy of the GO-water droplets [53, 116]. The graphene flakes may slightly reduce the evaporation rate due to ‘blocking’ evaporation path at the liquid-vapor interface [117], although the graphene oxide concentrations are kept low (≤ 0.1 wt.%). Nevertheless, reduction in evaporation rate is compensated with a lower pump infuse rate which is discovered through a slightly more extensive trial and error process as done with pure water droplets.

CHAPTER 4: VAPOR DEPOSITION OF GRAPHENE OXIDE

With the ability to maintain a steady state evaporating droplet, the following efforts detail the implementation of this experiment to develop a new method of large area 2D materials on arbitrary substrates using Evaporative Vapor Deposition (EVD). First, a review of the experimental setup and equipment used is discussed. Following, analysis of controlling the rate of condensation rates on the deposition substrate is presented, including an analysis of the effect placing a substrate above an evaporating droplet has on the droplet’s evaporation rate. These topics are important for future development of uniform, monolayer material deposition. Finally, deposition results are presented, and characterized with Raman.

4.1. Methodology

Table 4.1: Overview of various solutions prepared throughout this work, including the GO-water concentration amount and additives included (if any). Comments are listed as positives/negatives for each solution.

Solution	Concentration	Additives	Comments
A	0.1 wt.%	–	Very high concentration. Microfluid channel became clogged as solution evaporates.
B	0.05 wt.%	–	Good concentration. GO adheres to acrylic substrate, clogging microchannel over time.
C	0.05 wt.%	NaCl	High agglomeration rate. Reduced adhesion to acrylic substrate, no microchannel clogging.
D	0.05 wt.%	Sulfite	Increased stability with $-\text{SO}_3$ functional groups [118], See Chapter 5.

4.1.1. Solution Preparation

Graphene oxide solutions are prepared using liquid exfoliated graphite oxide powder. Ultra high purity water (resistance of $>18\text{M}\Omega$) is used as the solvent to reduce/eliminate precipitation of GO due to charged particles (ions) [119, 120]. The G_tO -water solution is ultrasonicated at 2W for 10-15 minutes. Various solutions were created, varying the GO concentration and additives for stability (see Table 4.1). Pure water and graphene oxide solutions in concentrations of 0.1 wt.% and 0.05 wt.% (termed Solutions A and B, respectively). Sodium Chloride (NaCl) is added to a solution of 0.05 wt.% (Solution C) to reduce adhesion to acrylic materials (i.e., the substrate the droplet is evaporating on). Long term stability for Solutions A and B is not observed, and agglomeration rate is accelerated in Solution C due to NaCl additive [119]. Noticeable precipitation is visible after ~ 2 hours after sonication for Solution C, while Solutions A and B exhibit slightly longer dispersion stability (see Fig. 4.1). Therefore, solutions are sonicated using a ultrasonicator prior to each experiment performed, assuring good dispersions during evaporative deposition.

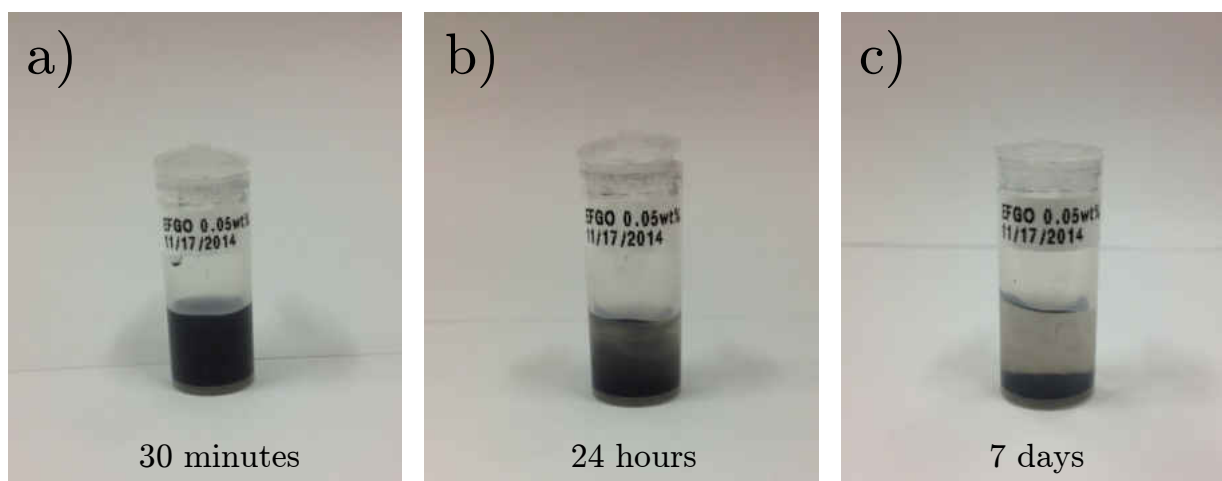


Figure 4.1: Images showing the stability of pure GO-water solution (Solution B). Time stamps represent time after sonication. Good dispersions is shown in (a), and noticeable precipitation is seen in (b). After sufficient time, the solvent and solute are significantly separated, (c).

4.1.2. Experimental Setup

The previously discussed steady state evaporation studies transitions to the current discussion on EVD. Additional components are included in the experimental setup, and overviewed in Fig. 4.2. Droplets are still formed on heated laser patterned substrates using the bottom-up methodology, as shown in Fig. 3.2. The droplet is a solution of liquid exfoliated GO, as detailed in Table 4.1. A motorized stage is positioned to translate a silicon wafer (replaceable with any arbitrary substrate) above the steady state evaporating graphene oxide solution. The motorized stage is a custom assembled assembly of two stepper motors (one for vertical positioning, and the other for linear translation parallel to substrate surface). The stepper motors have a 4 in. travel distance, with a resolution of $\sim 60\text{nm}$ (16 steps/ μm).

An infrared (IR) camera (FLIR SC7000) is mounted to record images from a vertical view (looking down on the droplet). The IR camera displays contour temperature plots for images, providing insight to the temperature distribution along the droplet's liquid-vapor interface and its effect on the surrounding substrate area (see Fig. 4.2). Most importantly, silicon exhibits high transmittance in the infrared spectrum [100], becoming nearly/completely transparent to the IR camera. Therefore, the IR camera provides a visual technique for determining of the amount of condensation formed on the passing silicon substrate, even though the condensate forms on the back facing side.

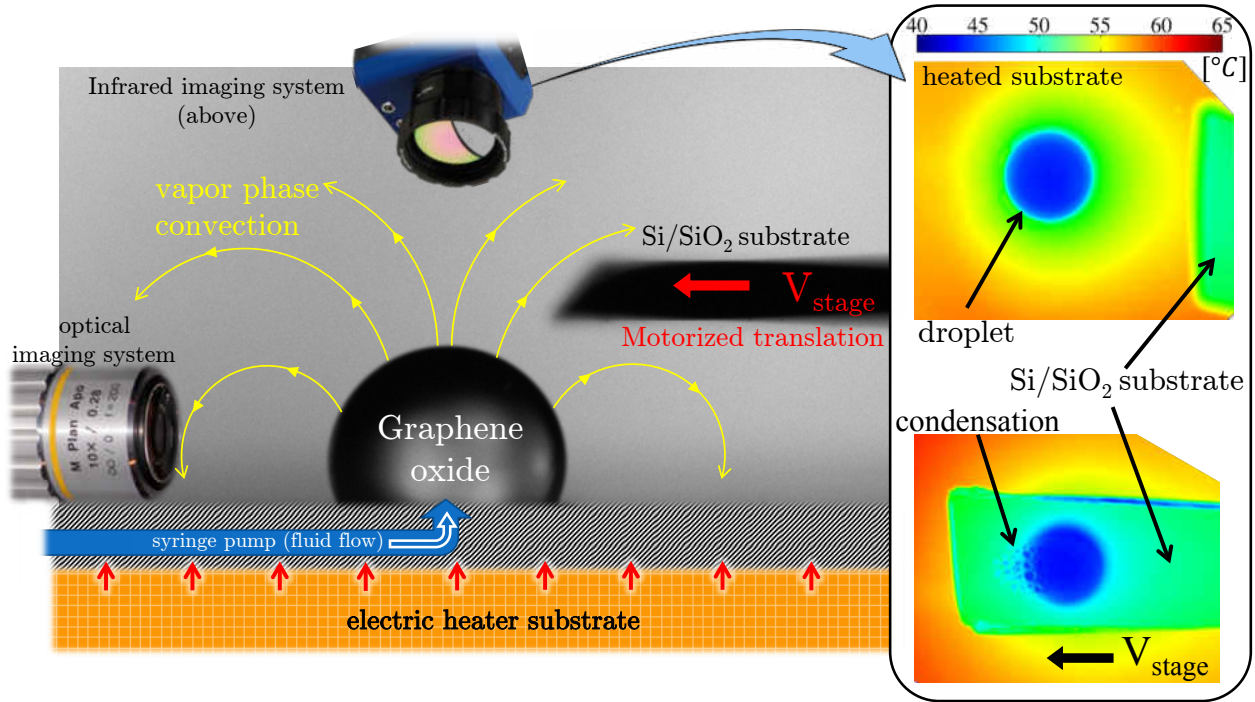


Figure 4.2: Experiment setup for evaporative vapor deposition. The setup is identical to that of droplet evaporation studies (see Fig. 3.2) with additional components. A silicon wafer is mounted to a motorized translation stage, and an IR camera records imaged from above. A sample IR image is shown, a droplet evaporating on a heated substrate and local cooling in both the droplet and substrate surrounding the droplet are noticeable. Visible condensate is visible on a translating Si substrate.

4.1.3. EVD Procedure

A fresh ultrasonicated GO-water solution is inserted into a glass 100 μ L gas tight syringe. The syringe is attached to a laser patterned substrate, which is cleaned using a bath sonicator proceeding past experiments. Placing into position, the syringe is connected to the syringe pump and the substrate is mounted to the electric heater to elevate the temperature to a desired condition. A fresh silicon wafer is attached to the motorized translation stage, and translated into position. A moderate infuse rate (50nL/s – 100nL/s) is used to form a droplet on the heated substrate, and switched to a reduced flow rate to maintain a steady state evaporating droplet at a desired contact angle ($\dot{m}_{\text{pump}} = \dot{m}_{\text{evap}}$, where the value is dependent on the droplets contact angle and substrate temperature T_s). Once the droplet becomes

stable (i.e., volume fluctuations are within $\sim 6\%$), a command is sent to the motorized stage to translate a specified horizontal distance and speed. It is discovered through extensive testing, that the deposition rate and condensation rate are highly dependent on (1) the height difference between the droplet apex and silicon wafer (deposition substrate); (2) the translation speed of the silicon wafer; and (3) the substrate temperature/droplet evaporation rate (both are coupled to each other).

4.2. Controlled Condensation Rates

Controlling condensation rates is an important aspect when ‘engineering’ this EVD technique for large scale, uniform deposition of materials. To produce uniform deposited materials, the reduction/suppression of dropwise condensation will overcome the coffee-ring effect (discussed previously). Throughout this work, there was no detection of deposited GO when condensation is not present. It is believed there is a thermodynamic energy limit that exist for graphene (or any atomic/nano-sized particles) to tag along with the vapor molecules. This energy barrier is overcome with the short transfer gap between the evaporating droplet and nuclei formed on the above substrate (hypothesized to be similar to an electrical discharge). Another hypothesis is the energy barrier associated with the GO flake adhering to the substrate. The air molecules on the substrate surface must be removed as the GO flake replaces them. This process is overcome by the vapor molecules condensing, forming droplets over time. Any GO particle can be readily captured and deposited onto the surface as the small condensate evaporates. Regardless of the physical phenomenon which occurs, no deposition is achieved/detected when no condensation is present. While the theory explaining this hypothesis is not discussed, attempts to provide arguments for this is done experimentally by controlling the condensate nuclei size and report the effect on deposition. It is hypothesized that maintaining the smallest droplets (nm in radius) mitigates the capil-

lary flow effects causing the non-uniform deposition at the liquid-vapor interface [44, 53, 55]. Thus, presenting a uniform, liquid solution based deposition technique.

4.2.1. Effect of Substrate Position on Droplet Evaporation Rates

Experiments are performed to evaluate the possible effect placing a substrate above an evaporating droplet has on the droplet's evaporation rate. This is crucial toward the stability of maintaining a steady state evaporating droplet. While steady state evaporation studies are not the focus of this research, past work [104] is used for predicting the evaporation rate. A quick verification that the substrate has no influence is beneficial for producing steady state droplets by using work done previously [97].

Three main experiments were performed. While these tests were reproduced for further verification, presenting the main cases will be sufficient for the present studies (again, steady state droplet evaporation is not the main focus of this work). These three cases include: (i) no substrate placed above an evaporating droplet; (ii) a Si wafer placed $\sim 1.5\text{mm}$ above the apex of an evaporating droplet (this will represent a substrate at a 'moderate' distance away, an intermediate to no substrate and EVD experiments); and (iii) a Si wafer placed $\sim 500\mu\text{m}$ above the apex of an evaporating droplet (this will simulate EVD experiments). The base substrate (the substrate which the droplet is evaporating on) is elevated to a temperature of $T_s = 60^\circ\text{C}$, which will be used during EVD experiments. The results for producing a steady state evaporating droplet with a contact angle of $\theta = 109^\circ$ is shown in Fig. 4.3, where the blue, red, and black curved represent cases (i), (ii), and (iii), respectively. Images captured during an experiment for case (i) and (ii) are also shown in Fig. 4.3. Notice the condensation forming on the substrate located above the droplet for case (ii).

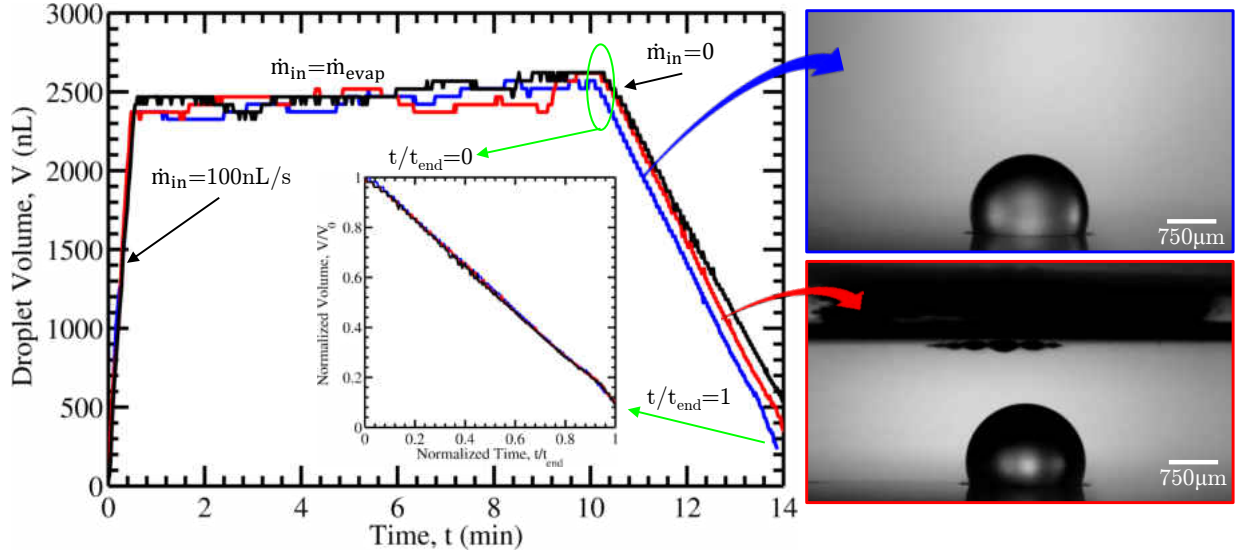


Figure 4.3: An analysis of the possible effect of positioning a substrate above an evaporating droplet on the evaporation rate. The plot shows the attempts to replicate an EVD by forming a droplet with a contact angle of $\theta \cong 109^\circ$ ($V \cong 2400\text{nL}$). Tests include no above substrate (blue curve), a substrate $\sim 1.5\text{mm}$ above the droplet’s apex (red curve) and $\sim 500\mu\text{m}$ above the droplet’s apex (black curve). Steady state droplet evaporation stability is not effected, and each data set for droplet evaporation rates (see inset) collapse to one curve.

As shown by the data, the stability to maintain steady state evaporating droplet is not effected with the placement of a substrate above the evaporating droplet. In these studies, an infuse rate of $14.1 \pm 0.3\text{nL/s}$ is used to maintain steady state. The volume fluctuations remain within 6%, which is determined to be an acceptable amount as the resulting fluctuations in the apex height are minimal in regards to the distance between the above substrate. Once the experiment time has reached 10 minutes (the predicted amount of time which will be used during EVD), the pump is terminated and the droplet is left to evaporate completely. When measuring the evaporation rate, and normalizing the three experiments (see inset in Fig. 4.3), the evaporation rate all match well with each other and the infuse rate used. For case (iii) (no optical image shown, but represented by the black data curve in Fig. 4.3), larger condensate formed compared to case (ii) shown in Fig. 4.3. Comparing to case (i) with no substrate, it is predicted the vapor concentration surrounding the evaporating droplet is higher (i.e., closer to saturation thus having a smaller gradient). Reducing the vapor concentration gradient

between the environment and liquid vapor interface will cause a reduction in evaporation rate when diffusion is dominant (e.g., droplet evaporation at room temperature) [55, 102, 121, 122]. The dominance of diffusion is mitigated at elevated substrate temperatures, thus less influential to vapor concentration gradients. The normalized evaporation curves all collapse to one (see Fig. 4.3 inset), further proving the substrate has no effect on the droplets evaporation rate at elevated substrate temperatures.

4.2.2. Speed and Height Dependence on Condensation Rates

Of course, there is a position such that the translating substrate may be considered ‘far field,’ such that its presence has no effect on the vapor convection patterns induced by the evaporating droplet. As the substrate moves from ‘far field’ to an influential position (‘near field’), the vapor will begin to condense on the substrate (assuming the substrate is stationary). Alternatively, a substrate translating in the ‘far field’ will cause a larger area of condensate, effectively reducing the condensation rate over a local area. In this case, the condensate will evaporate before it will accumulate/coalesce to form visible droplets. As the translation speed slows, the effective condensation rate over a local area increases (while the evaporation rate remains constant) causing droplets to form. Further reduction of the translation speed simply increases the local condensation rate and forms larger droplets. Therefore, there is a strong coupling between the substrates distance and its translating speed to the condensation rate on the substrate being deposited.

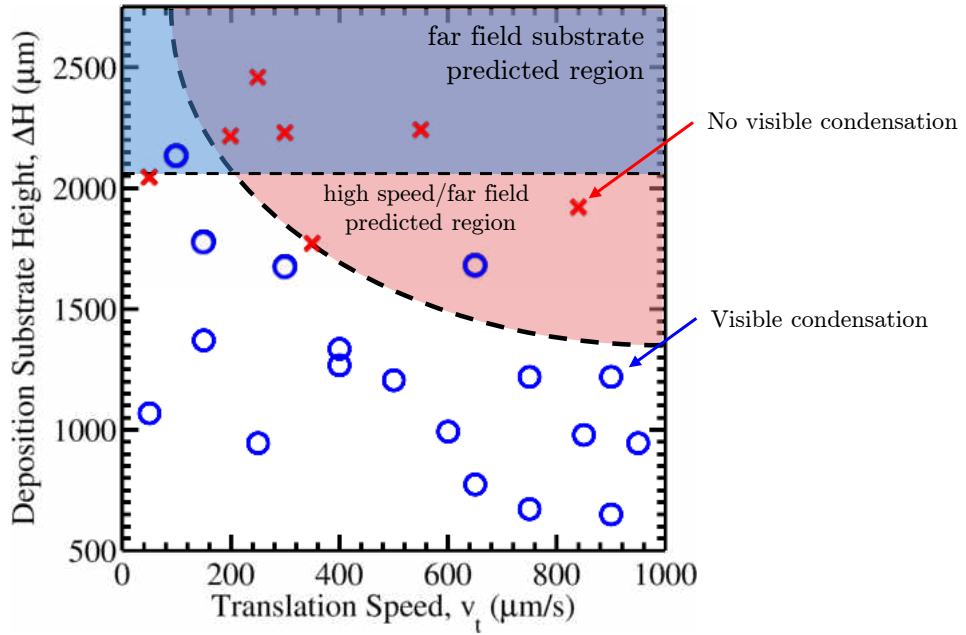


Figure 4.4: Experimental data collected for determining the approximate limitations for obtaining condensation on a translating substrate. Shaded regions are included as the predicted limitations of a ‘far field’ substrate and a combination of high translation speed and far field such that no vapor condenses onto the translating substrate.

These ‘far field’ regions are predicted experimentally. By performing various tests with different height distances and translation speeds, the experiment is marked as either *visible condensation* or *no visible condensation*. Compiling the data, estimations of the ‘far field’ regions may be predicted as shown in Fig. 4.4. At approximately 2mm from the droplet’s apex, the substrate did not accumulate any visible condensation (regardless of speed). The speed and height dependence is more difficult, and may include a larger transition region (where nucleation may or may not occur for the same conditions). Nevertheless, this region is approximated to the best knowledge, as shown in Fig. 4.4.

There is a speed and height dependence on the size of the condensed droplets, which is a more crucial study for this work. As condensation droplet size is the main focus of this study, a careful selection of speed and height will produce large or small droplets (where small droplets are beneficial toward uniform deposition). For example, three experiments

performed at different translation speeds and height are shown in Fig. 4.5. The size of droplets condensed onto the silicon substrate can be seen clearly in the IR images. For a slow translation speed ($10\mu\text{m/s}$, see Fig. 4.5a), droplets as large as $V \cong 12\text{nL}$ accumulated from condensation. With a higher height difference and faster translation speed, the condensate size reduced to $V \lesssim 2\text{nL}$ (see Fig. 4.5b). Further increasing translation speeds kept droplet nuclei volume $V \lesssim 15\text{pL}$ with a droplet radius of $R \lesssim 30\mu\text{m}$ (see Fig. 4.5c).

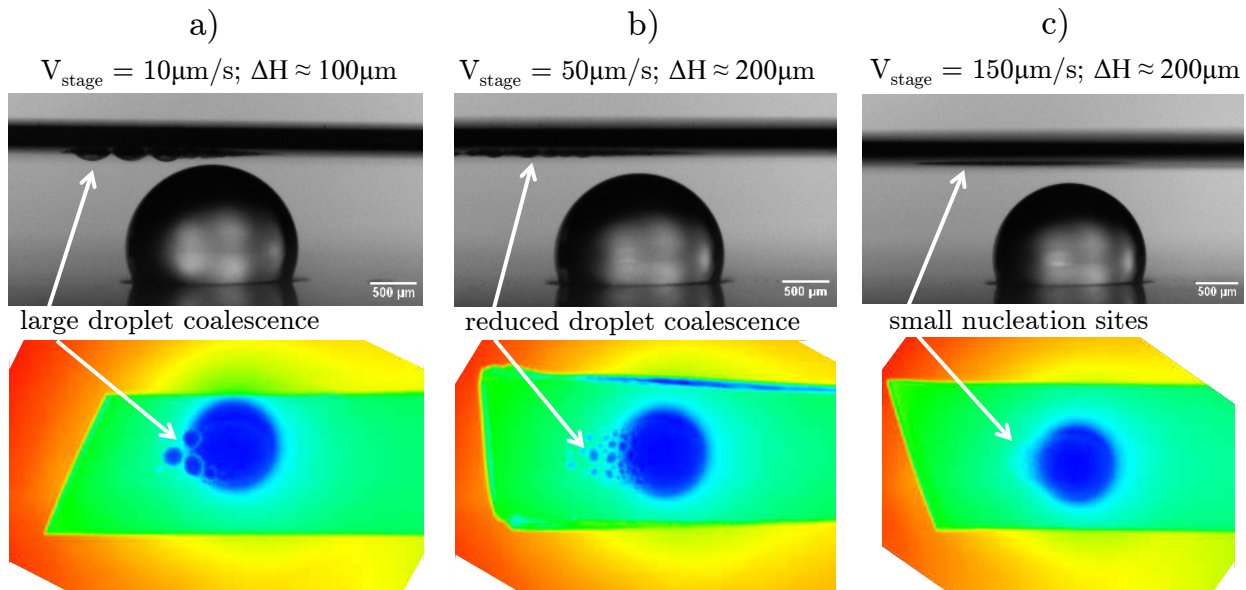


Figure 4.5: Images captured during experiments to demonstrate the range of condensate formation on a silicon substrate. Top images are optical imaging of a steady state evaporating droplet, and bottom images are IR images taken from above at the same time instant. As the speed increases from (a) $10\mu\text{m/s}$ to (c) $150\mu\text{m/s}$, the condensation rate is reduced to minimize droplet coalescence.

Although these general transition regions (based on Fig. 4.4) are rough approximations based on experimental data, it provides some assistance in being able to predict if large droplets will form (i.e., slow speed and small height difference) or small droplets (i.e., fast and/or large height difference) will be present. Avoiding extensive and rigorous experimental testing and backing with theory, this is a sufficient approximation for the present study

(where a large focus is simply proof of concept of evaporative vapor deposition of materials). In further (future) studies, where this methodology is being developed and fine-tuned for producing large scale monolayer materials, an in-depth investigation of controlling the condensation rates and nucleation size will benefit deposition production greatly.

4.3. Raman Scans for Deposition Detection

Characterizing the deposited GO flakes (e.g., size, quality, thickness, etc.) is crucial toward further implementation, and quick tests/verifications are necessary. As past reports have discussed, there are a wide variety of techniques for studying graphene although are impractical for *searching* for graphene. Optical contrast of monolayer materials is minimal, even which carefully selected SiO₂ substrate selection [65]. AFM is highly impractical to scan substrate sized regions (on the order of cm²), and TEM imaging is a destructive test [73]. Thus, the rise of Raman spectroscopy for detecting graphene has been a major contribution toward graphene studies [74–76].

For this work, a Renishaw inVia Raman Spectroscope, 60mW laser at a wavelength of $\lambda = 532\text{nm}$ is used. A low powered laser is beneficial, avoiding possible burning of the deposited material. Tests were performed with various laser powers, where a reduced laser power produced a lower signal intensity. Because no damage was found using the highest laser power setting, max power is used for its high signal/noise ratio. The wavelength is important when trying to characterize graphene/GO flakes (e.g., monolayer vs. bi- and tri-layer graphene) as minor deviations are present between different laser wavelengths [74]. Although, the main characteristic peaks of graphene/graphite remain at $\sim 1350\text{cm}^{-1}$, $\sim 1580\text{cm}^{-1}$, and $\sim 2700\text{cm}^{-1}$.

4.3.1. Analysis of Graphene Visibility on Si/SiO₂

One of the biggest challenges in detecting graphene (especially flakes at atomic thicknesses) is its lack of optical contrast. This is believed to be a major contribution to its late discovery despite past efforts to experimentally produce it [11, 21]. It was reported that careful selection of the substrate (namely 90nm or 300nm SiO₂ on Si wafers) darkens monolayer graphene flakes to be optically visible. Even so, the visibility of graphene on these ‘ideal’ substrates remains faint.

Refractive index theory details why the contrast is influenced by the thickness of the SiO₂ thickness, and can be used to seek possible alternatives to increase monolayer graphene contrast. A simple schematic of a monolayer graphene flake on a Si/SiO₂ substrate is shown in Fig. 4.6. Graphene (monolayer, with a film thickness of $t \cong 0.34\text{nm}$) has a light refractive index (n) of $n_1 = 2.6 - 1.3i$ [123]. The complex component of the refractive index is excitation, relating to the absorption of light as it passes through (whereas the real component is related to how light passes through). This value may be approximated as a constant, therefore independent of thickness and wavelength (importantly, this theory is useful for analysis of monolayer graphene to bulk graphite). The refractive indices of silicon (Si) and silicon oxide (SiO₂) are functions of wavelength (see Figs. 4.6b and 4.6c) [124].

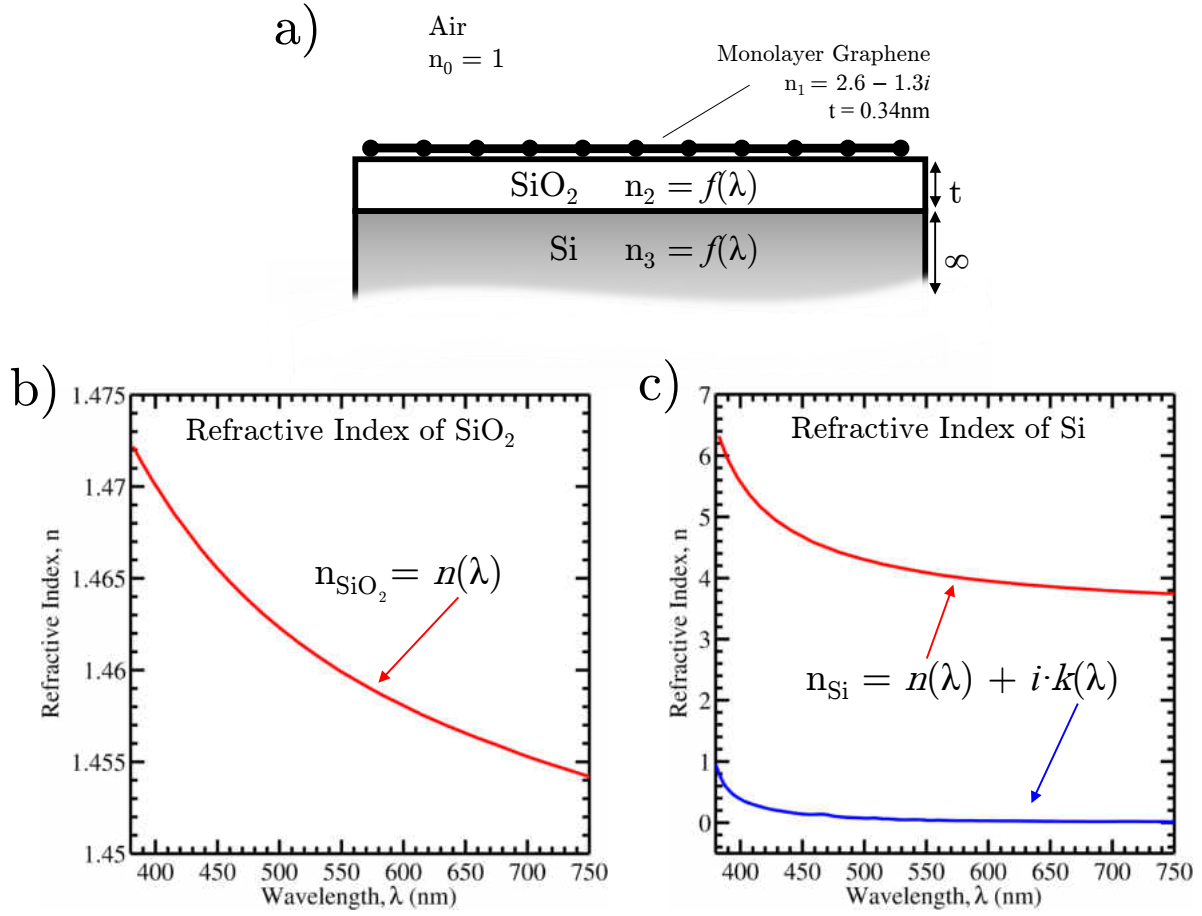


Figure 4.6: a) Schematic representing a monolayer of graphene on a Si/SiO₂ substrate. The refractive index for monolayer graphene is $n = 2.6 - 1.3i$ and air is $n = 1$. SiO₂ and Si are functions of the light wavelength, shown in (b) and (c), respectively.

To determine the contrast of monolayer graphene on a Si/SiO₂ substrate, an analysis of the intensity of reflected light ($I(n_1)$) is calculated through geometry of light refractions and the phase shift during optical transmittance [21], shown in Eq. (4.1)

$$\begin{aligned}
 I(n_1) = & \left| \left(r_1 e^{i(\Phi_1 + \Phi_2)} + r_2 e^{-i(\Phi_1 - \Phi_2)} + r_3 e^{-i(\Phi_1 + \Phi_2)} + r_1 r_2 r_3 e^{i(\Phi_1 - \Phi_2)} \right) \right. \\
 & \left. \times \left(e^{i(\Phi_1 + \Phi_2)} + r_1 r_2 e^{-i(\Phi_1 - \Phi_2)} + r_1 r_3 e^{-i(\Phi_1 + \Phi_2)} + r_2 r_3 e^{i(\Phi_1 - \Phi_2)} \right)^{-1} \right|^2 \quad (4.1)
 \end{aligned}$$

with the relative refractive indices (r_j) as

$$r_j = \frac{n_{j-1} - n_j}{n_{j-1} + n_j}, \quad j = 1, 2, 3, \quad (4.2)$$

and the phase shifts represented as

$$\Phi_j = \frac{2\pi n_j t_j}{\lambda}, \quad j = 1, 2. \quad (4.3)$$

The refractive index (n_j) and the thickness (t_j) corresponds to the material shown in Fig. 4.6. For example $n_1 = 2.6 - 1.6i$ for graphene, with a thickness $t_1 = 0.34\text{nm}$. The silicon is the base substrate, therefore its thickness (300–600 μm in the present studies) may be approximated as $t \rightarrow \infty$ compared to graphene and SiO_2 layers. This eliminates the phase shift associated with the Si layer, Φ_3 .

Equation (4.1) is evaluated, and the results are shown in Fig. 4.7. The contrast ratio contour plot provides a visual of the level of contrast of monolayer graphene on various SiO_2 thicknesses at a given light wavelength. A color plot is included along the wavelength axis to relate to the colors in the visible spectrum (e.g., $\sim 750\text{nm}$ wavelength corresponds to red light, and $\sim 450\text{nm}$ wavelength corresponds to blue). The blue curve (right y-axis) represents the average contrast over the visible spectrum (i.e., the approximate contrast of graphene under white light). Contrast dependence on wavelength is shown for SiO_2 thicknesses of 0nm, 90nm, 300nm, and 500nm. This shows the difficulty in visually finding graphene, as the contrast intensity on pure Si ($\text{SiO}_2 = 0\text{nm}$) is near zero. A maximum contrast is at an SiO_2 thickness of $\sim 90\text{nm}$, although the industry standard is 300nm [4, 11, 64, 74, 79]. In this study, pure Si ($\text{SiO}_2 = 0\text{nm}$) and Si with thermally grown 500nm SiO_2 are used. The contrast of monolayer graphene on 500nm SiO_2 is slightly less than the standard 300nm SiO_2 , although the present study is not focused on idealizing the method to produce monolayers.

Therefore, typical depositions result in FLG and bulk thin film graphite flakes which are easily viewed on any substrate under a microscope.

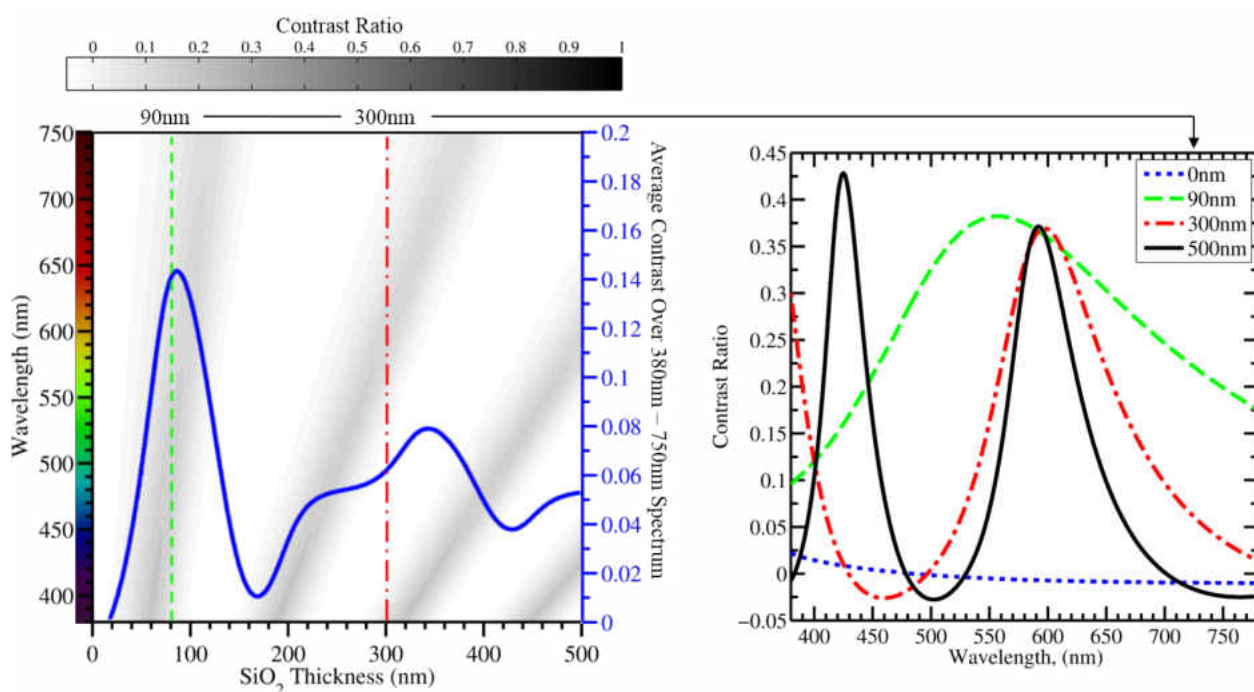


Figure 4.7: The contrast of monolayer graphene on Si/SiO₂ substrates, based on the thickness of SiO₂ and wavelength of light. (Left) The averaged contrast over the entire visible spectrum is represented as the blue curve, where the grey-scale background is the modeled contrast at each wavelength. (Right) Contrast of graphene as a function of light wavelength, for a fixed SiO₂ thickness. Note the maximum contrast at ~90nm, and nearly invisible at 0nm.

4.3.2. Drop Casting for Baseline Reference

To provide a baseline reference for Raman detection of GO from vapor deposition, a GO droplet was drop casted on a clean silicon wafer. Silicon is an ideal substrate due to its single strong Raman shift (with a second order, relatively strong shift) which does not interact with the Raman shifts of graphene/graphite [76]. The drop casting method is reviewed in Fig. 4.8a, and the results are shown in Figs. 4.8b and 4.8c. Drop casting is manually placing a GO droplet on a silicon substrate and letting it evaporate. As discussed previously, this

results in the *coffee-ring* effect. Scans are performed on a clean Si, FLG (the inner region of the coffee-ring), and bulk graphite (on the dominant coffee-ring) shown in Fig. 4.8. The Raman scans match the expected scans when comparing to literature [74]. Silicon has a very strong Raman shift at $\sim 522\text{cm}^{-1}$, with a second order shift over $\sim 925\text{-}975\text{cm}^{-1}$ as shown in the blue curve in Fig. 4.8c.

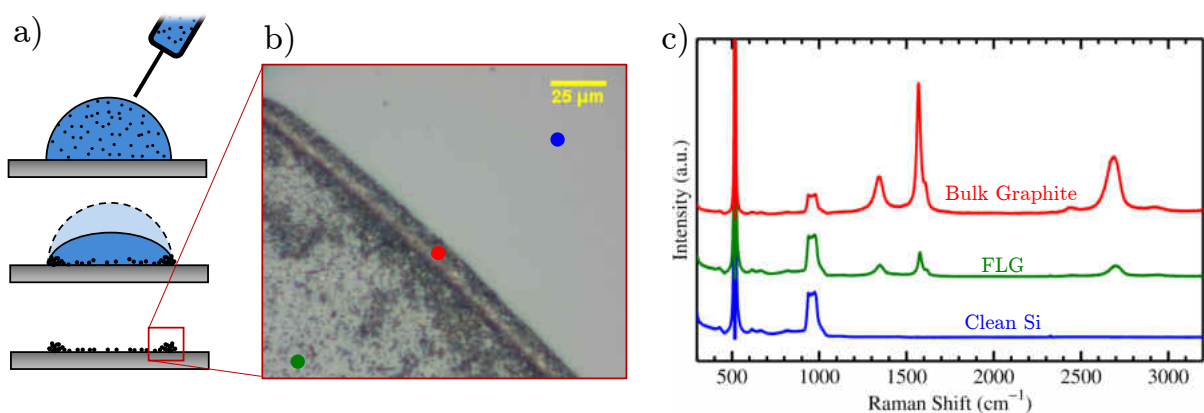


Figure 4.8: a) Overview of the drop casting deposition technique, resulting in the coffee-ring effect. b) Optical image of the dominant coffee-ring formation from drop casting a 0.1wt.% GO solution. Colored spots represent location of the Raman scan shown in c). c) Raman scans performed to compare Si, FLG and bulk graphite with literature. The Si peak is off-axis for clarity of all other peaks.

Scanning deposited GO regions caused a decrease in intensity of the Si peaks, which is dependent on the thickness of the deposit. This is demonstrated by the decrease in second order Raman shift in Si ($\sim 925\text{-}975\text{cm}^{-1}$ range) in Fig. 4.8c. Additionally, the intensity of graphene/graphite Raman shift increases with increasing deposition thickness (i.e., bulk graphite has higher intensity than FLG). Comparing with literature, all three dominant peaks are captured for GO. These peaks are the D-band (at $\sim 1350\text{cm}^{-1}$), the G-band (at $\sim 1580\text{cm}^{-1}$), and the 2D-band (at $\sim 2700\text{cm}^{-1}$). This also sets the baseline for future experiments; comparing various other parameters such as curve fitting the 2D-band for ap-

proximate thickness of the GO flake [74], and relative intensity of the D-band and G-band for quality (i.e., amount of defects or oxygen functionalization) [76, 80, 125].

For example, there is a minor peak visible at $\sim 1620\text{cm}^{-1}$, which is termed the D' (see Fig. 4.9c). This peak is not commonly discussed in literature, and not always present due to being buried in the G-band shift. Eckmann et al. [80] recently reported its significance in classifying the type of graphene defect – based on the relative defect intensity ratio. The defect ratio being the ratio of intensity between the D and D' , $I_D/I_{D'}$. Higher defect intensity ratios are present for sp^3 functionalized graphene flakes (i.e., GO as in Fig. 4.9b), while lower defect intensity ratios are measured for graphene flakes with holes (i.e., the honeycomb carbon structure missing carbon atoms, see Fig. 4.9a). These ‘hole’ defects can be caused by overexposure to ultrasonication [118], where energies sufficiently high can break in-plane bonds (as opposed to breaking the much weaker out-of-plane van der Waals forces to separate the graphene sheets). The small uncharacteristic peak present at $\sim 2330\text{cm}^{-1}$ is caused by nitrogen (N_2) in the atmosphere [125], which is occasionally captured with Raman scans presumably based on the length of exposure or the signal to noise ratio.

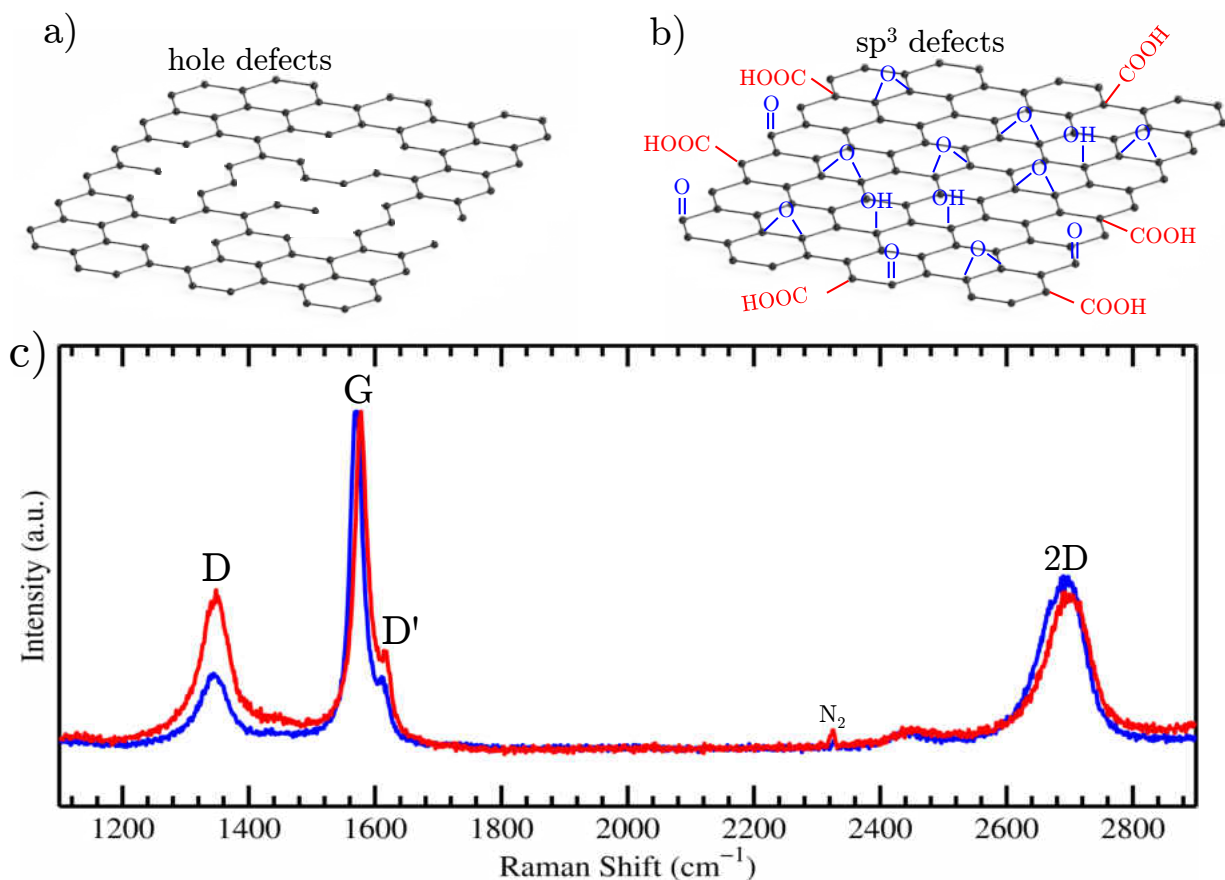


Figure 4.9: The quality of the deposited GO flakes, in regards to the defects, can be identified based on the intensity of the Raman shift. The D-band (at 1350cm^{-1}) with respect to the G-band (at 1580cm^{-1}) estimates the amount of defect. Hole defects (a) and sp^3 functionalization defects (b) are indicated by the intensity of the D/D' Raman shift, (c). Raman data in (c) is normalized with respect to the G-band intensity.

4.3.3. Results for Evaporative Vapor Deposition

The resulting deposition achieved through the developed EVD technique is summarized. First, an EVD experiment using pure Deionized (DI) water is done as a control/benchmark. This experiment, which is predicted to show no graphene deposition, is crucial for affirming that the deposited material source is the evaporating droplet and not captured as contamination from the environment. Proceeding, the results of EVD with graphene oxide is presented. Characterization of deposited GO is included, along with possible concerns and improvements to increase throughput and uniformity.

4.3.3.1. Null Experiment with Deionized Water

An experiment is performed without any graphene dispersion as a validation/benchmark. The setup in this work is not ideal due to not performing deposition in a clean room. As a result, there is dust and other contamination being deposited onto the substrate (e.g., dust from the environment). While unlikely, it could be possible that a contaminant gathered from the surrounding environment exhibits the same peaks as graphene (i.e., carbon-carbon bonds). Therefore, a benchmark experiment without GO is performed simply by performing a EVD experiment with the droplet of GO solution replaced with pure DI water (i.e., with all other components identical to an EVD experiment, as shown in Fig. 4.2). Scanning the deposited region, all particles did not exhibit the characteristic Raman shift of graphene, thus refuting the possibility that graphene, or any other carbon based material with identical Raman shifts, is captured from the surrounding environment.

4.3.3.2. Graphene Deposition

Silicon wafers are cut to an appropriate size for deposition. The cut Si wafers are placed in an ultrasonic bath to remove any dust or Si debris that adhered to the substrate during the preparation. To avoid any possible ‘false positive’ detection, wafers are never used in multiple experiments. After EVD, the wafer is properly labeled and stored for potential future re-analysis.

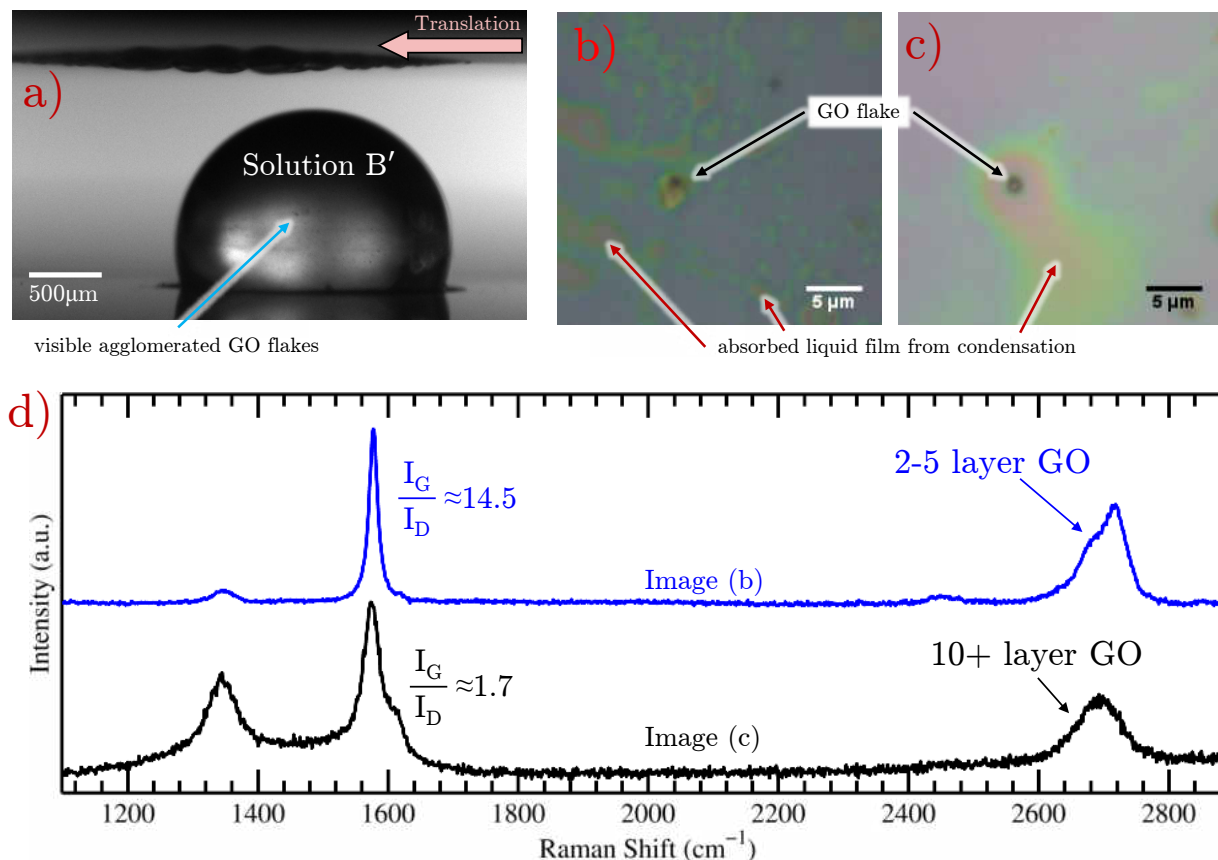


Figure 4.10: Results of an Evaporative Vapor Deposition of graphene oxide (a), with moderately high condensation. Optically visible GO flakes (b) and (c) are found. The Raman scan (d) is normalized to the G-band intensity. (b) shows good crystalline quality with a high I_G/I_D ratio, and the 2D-band shows characteristics of 2-5 layer GO. The surrounding discoloration is presumably due to the absorbed thin film from the condensation, and showed no Raman shift.

Preliminary results from an EVD experiment is shown in Fig. 4.10, using a droplet of Solution C (see Table 4.1). Due to the addition of NaCl (decreasing long term stability), visible agglomeration is shown to occur during the experiment (see Fig. 4.10a). This is expected to reduce the amount of deposition, but still successful as shown in Figs. 4.10b and 4.10c. Surrounding the GO flakes (consistent throughout the condensation region shown in Fig. 4.10a), discoloration in the Si wafer is visible. This is presumably due to the absorbed liquid thin film meniscus of DI water (the solvent) which does not evaporate [82, 126]. This

region showed no Raman activity, and no significant alterations in the Si intensity/shift was measured.

The main region of interest (ROI) is the deposited GO flake. The Raman shift (Fig. 4.10d) showed the expected D-, G-, and 2D-band shifts of graphene. A high I_G/I_D ratio demonstrates good crystalline quality for Fig. 4.10b (lacking hole/ sp^3 defects, shown in Fig. 4.9). Additionally, the characteristic shape of the 2D-band matches closely with reported 2-5 graphene layers [74]. The 2D-band for Fig. 4.10c exhibits a smoother, single Gaussian-like broad curve; characteristic of bulk graphite (>10 layers). In its current development, this EVD technique is not able to produce specific GO thicknesses/quality. Nevertheless, demonstration that different quality deposition is achieved opens for further development for controlling these deposition qualities.

4.3.4. Raman Scans for Depth Testing

Raman spectroscopy may also be used for determining an *approximate* thickness of materials. Based on the location on/in a material that a Raman laser is focused at, the intensity of the materials vibrational modes (i.e., Raman shift) will change. For example, when a laser is focused on the surface of a material the resulting Raman shift will be much more intense compared to a signal where the laser is focused just above/below the material (causing a more diffuse laser beam and larger scattering). This is illustrated in Fig. 4.11. At one distance, the Raman laser is focused on the deposited graphene (shown in blue) and provides a high shift intensity of the D-band, G-band, and 2D-band. At the substrate is raised (increase in z-location, focusing the laser on the Si substrate) the intensity of the Si Raman shifts (first and second order shift at $\sim 522\text{cm}^{-1}$ and $\sim 1000\text{cm}^{-1}$, respectively) increases and the graphene peaks decrease. Comparing the intensity evolution over a wide range on substrate vertical positions, the maximum is the position where the laser beam

is focused; thus a reference where the surface of the material/substrate is. Therefore, the position for a maximum Raman shift of a base substrate can be compared to the position for maximum Raman shift of a deposited material (on the substrate) – the difference in vertical position will provide an approximate thickness of the deposited material.

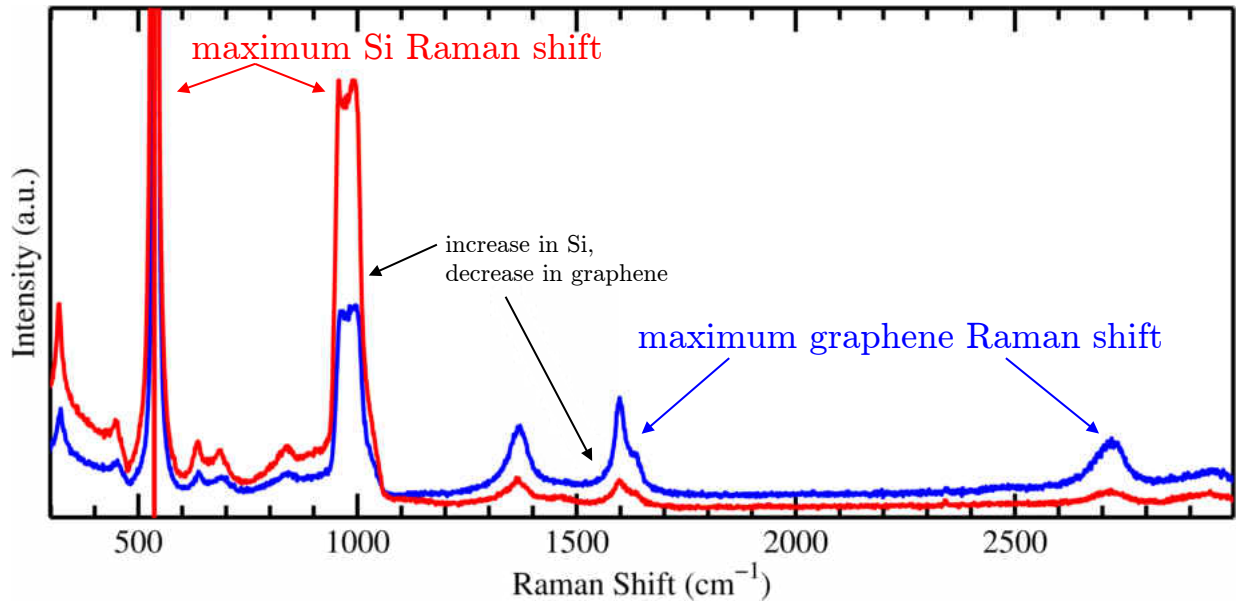


Figure 4.11: Raman scans at two different focal distances, demonstrating the decrease in a substrate’s Raman shift (Si) as a result of an increase in a deposited material’s Raman shift (graphene).

Further investigation is done regarding approximate EVD deposited graphene thicknesses. A visual representation of the technique is provided in Fig. 4.12a. Two sample scans are shown in Fig. 4.12b, focusing on the main characteristic Raman shifts of graphene and silicon (the G-band at $\sim 1580\text{cm}^{-1}$ and the first order shift of Si at $\sim 522\text{cm}^{-1}$). The red plot represents a Raman scan which measured a maximum intensity of Si, and the blue curve represents a Raman scan which measured the maximum graphene shift at a position of $\Delta z \cong 600\text{nm}$. As expected, the Raman shifts of these two materials are inversely proportional to each other (as the vertical distance is changed). To demonstrate an increase in thickness of

graphene will cause a larger displacement Δz needed to achieve the maximum shifts, a ‘thick’ graphene flake (see Figs. 4.12c and 4.12d) and a ‘thin’ graphene flake (see Figs. 4.12d and 4.12e) are tested. Additionally, the evolution of the intensity of Si and all graphene Raman shifts are plotted over a range of z-positions. The intensities of each shift is normalized with the maximum shift of that peak (e.g., G-band/G-band_{max}) for clarity during comparison. The ‘thicker’ graphene flake is determined based on the increase in contrast (i.e., darker) compared to a ‘thinner’ flake. The results in Figs. 4.12c and 4.12e match expectations. A darker ‘thicker’ flake shows a larger displacement between the maximum Si and graphene Raman shifts compared to the ‘thinner’ flake. Also, all graphene peaks follow the same trend; the D-band, G-band, and 2D-band all collapse to one curve when normalized. Therefore, any deterministic peak of the substrate/material can be analyzed to determine its vertical position where the laser is focused.

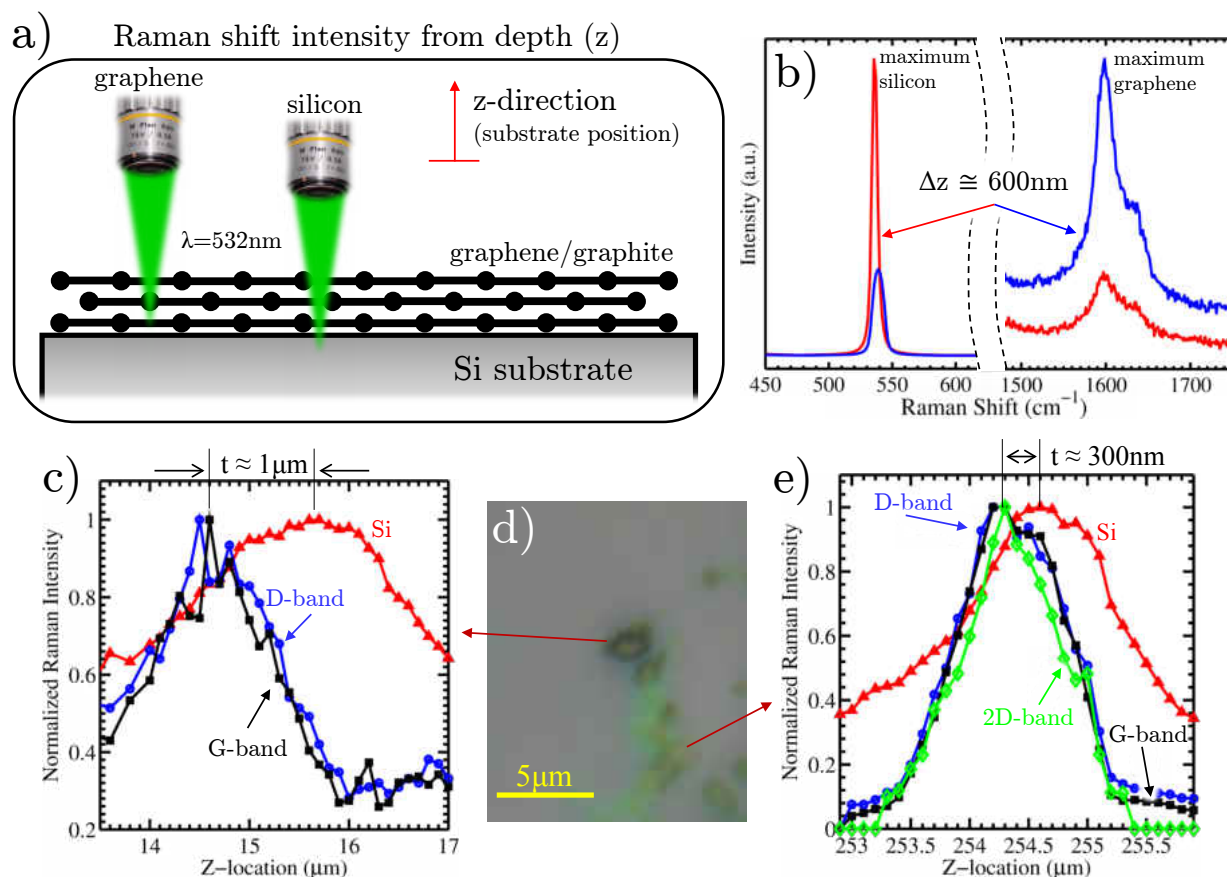


Figure 4.12: Raman scans for approximate graphene thickness. a) A schematic demonstrating the technique used for measuring approximate thickness of GO deposits, along with z-location orientation. b) Raman shift intensity differences based on focus location (red is focused on Si, blue is focused on graphene). d) Optical image showing different thickness deposits (based on darkness of the material), and resulting Raman scans showing the thickness of (c) a thicker/darker flake and (e) thinner/lighter flake. The difference in location of maximum Si shift intensity and *any* graphene shift provides the thickness

This technique proves to be more useful for thicker materials (compared to $\lesssim 1\text{nm}$ of FLG), at least for the equipment used in this study. The resolution of the translation stage with the Raman spectroscope is 100nm. Therefore, this technique is able to determine the thickness of a material within $\pm 100\text{nm}$. This, of course, is well beyond the resolution needed for determining thickness of FLG (which is expected to be $\sim 1\text{-}10\text{nm}$ [1, 11]). As the development of this EVD technique is still largely in the development phase, a majority of the GO deposits are larger agglomerated clusters (i.e., much thicker than FLG); thus a useful technique is for this work.

CHAPTER 5: IMPROVEMENTS IN EVAPORATIVE VAPOR DEPOSITION

Proceeding the preliminary results, demonstrating the ability to deposit graphene through the vapor phase, efforts are put toward refining and expanding the results. Importantly, efforts are put toward localizing the deposition regions and performing additional characterization of the deposited GO materials (e.g., XPS and AFM). Localizing the deposition region will not only reduce the time needed scanning large regions for graphene (or any deposited material) but important for implementing this technique in various applications. Additionally, further characterization techniques (beyond Raman) are proposed to gain a better understanding of the deposited materials and ultimately provide unambiguous vapor deposition results.

5.1. Laser Etching Silicon Wafers for Deposition ROI

Creating a Region of Interest (ROI) is highly beneficial for reducing the Raman scanning area for detecting graphene deposition. Additionally, localizing the deposition is beneficial for other characterization techniques such as AFM and XPS, which might not have the luxury of step by step magnification, or an in-situ optical camera like Raman. Therefore, an ROI is defined by laser etching squares on Si (overviewed in Fig. 5.1). As stated previously, Si is IR transparent [100], therefore the laser etched ROI can be clearly seen from the back side (see Fig. 5.1c) ensuring the deposition is occurring centered in the ROI.

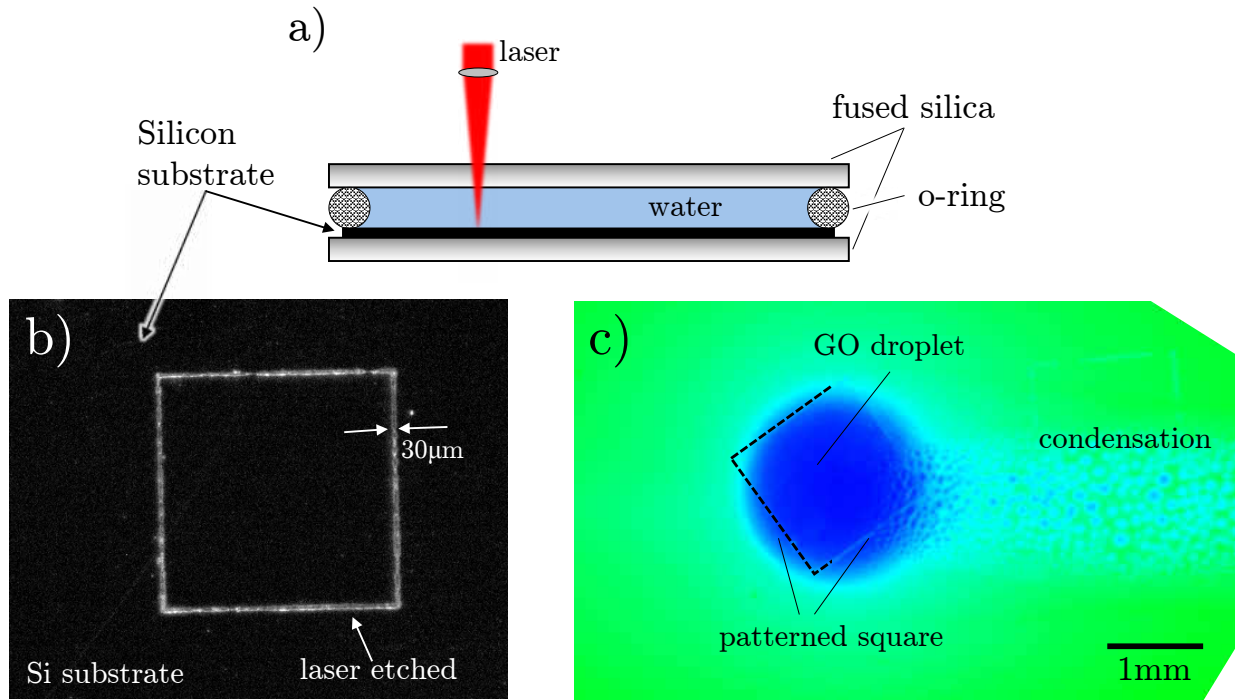


Figure 5.1: Overview of laser etching Si wafers for defining a ROI during deposition. (a) Schematic showing the process for water assisted laser etching wafers. (b) A laser etched square on Si, 1.5mm×1.5mm. (c) The laser etched square position during EVD experiment, and the location of condensation/deposition centered on this ROI.

A different approach for laser etching Si wafers is used compared to the process used for acrylic polymer substrates detailed previously (see Fig. 3.1). The Si wafer is not transparent to the laser wavelength ($\lambda = 786\text{nm}$), but highly reflective [100]. Additionally, its high thermal conductivity will require significantly higher laser pulse energies to ablate the surface [127, 128]. Therefore, the application of an opaque film is necessary as with the acrylic polymer substrates; but introduces further complications due to contamination (even proceeding proper cleaning procedures). Instead, a water assisted laser etching approach is implemented, which in some ways is analogous to the opaque film. The Si wafer is exposed to the laser submerged in a DI water fluid cell instead of applying the opaque film (see Fig. 5.1a). An optically transparent fused silica glass window encapsulates the water bath and Si substrate. It is hypothesized that focusing the laser on the Si/H₂O interface vaporizes the

water, creating a highly accurate water-jet cutter. A Si laser etched square is shown in Fig. 5.1b, with an approximate etching width of $\sim 30\mu\text{m}$. The resulting etching causes can be seen in the IR camera, show during an EVD experiment, in Fig. 5.1c. To verify the laser etching does not contaminate the substrate, Raman scans of the ROI after performing a proper cleaning procedure [129] is performed. The optical images shows no visible defects/objects (e.g., dust or other) and scans over arbitrary locations showed no distinct shift. Therefore, it is affirmed the laser etching process does not affect the Si wafer ROI and deposition will occur as it has in previous studies without a laser etched ROI.

5.2. New GO Solution for Increased Stability

Graphene dispersions in water are not stable, quickly agglomerating due to being hydrophobic [28]. Graphene oxide (graphene with oxygen functional groups such as epoxide, carbonyl, and carboxyl) becomes hydrophilic, thus readily dispersible in water. Although, GO still agglomerates in the presents of ions [120], thus highly pure DI water must be used. Nevertheless, the agglomeration rate remains relatively high (for Solutions A and B used in this work, see Table 4.1) and must be re-sonicated after a few hours. The experimental setup used in this work benefited with the addition of NaCl (Solution C, see Table 4.1), although significantly increased the agglomeration rate (deemed not unusable for EVD ~ 30 minutes after sonication). The lack of long term stability is a significant issue, deposition rates becomes highly limited if only larger clusters are present. Thus, a new solution (Solution D, see Table 4.1) was synthesized. Si and Samulski [118] reported a highly dispersible solution by chemically reducing GO (removing residual oxygen functional groups) and introduces sulfite ($-\text{SO}_3^-$) which reduces the agglomeration between graphene sheets. The synthesis procedure reported [118] is followed, and refer the reader for the details.

As shown in Fig. 5.2, the stability of the GO solutions is significantly improved. No significant agglomeration occurs over a week after ultrasonication (Figs. 5.2a, 5.2b, & 5.2c); a significant improvement compared to other solutions discussed previously (see Figs. 4.1 and 5.2d). Stability allows longer EVD experiments for higher deposition concentrations due to both (1) minimizing bulk graphene clusters too large for vapor molecules to transport from forming and (2) long duration depositions (i.e., large scale/area deposition). A secondary benefit of the sulfonated GO synthesis is the partial restoration of electrical conductivity, which can be further restored (post deposition) to $\sim 1/4^{\text{th}}$ pristine graphene [118]. Overall, Solution D shows significant improvements for stability and is better suited for future applications.

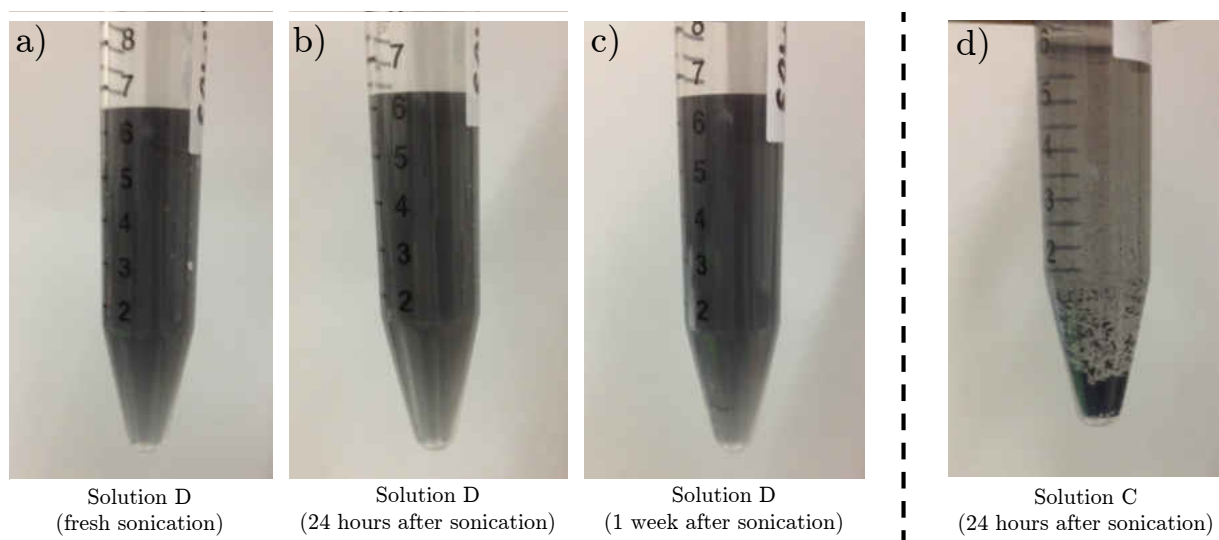


Figure 5.2: Long term stability of GO solution with sulfite groups (Solution D) compared to a GO-NaCl solution (Solution C). Importantly, (b) and (d) represent two solutions both 24 hours after sonication. Solution C (with NaCl additive) has a majority of GO precipitated while no noticeable precipitation forms for Solution D (with $-\text{SO}_3$).

5.3. Multi-Step Deposition Process on Single Substrate

Versatility in material deposition (controlling size, thickness, etc.) is important to gain interest in a wide variety of disciplines. In some cases, applications may require localized deposition. This includes deposition within a defined location (with no deposition elsewhere) and various material thicknesses on a single wafer. For example, fabricating a ‘master’ wafer that has well defined and diverse graphene thicknesses across the wafer may benefit as a calibration substrate for future research development. Additionally, limiting a multi-step post processing after deposition to a single cycle (versus repeated for multiple substrates) can significantly increase production output and reduce resources used.

To test/demonstrate the ability to achieve this with EVD, a single strip is patterned with multiple ROI in a series. The substrate is translated over the evaporating GO droplet (as shown in Fig. 4.2). Once the first ROI is no longer within the vicinity of the droplet (such that no condensation will occur, empirically estimated), the translation speed is increased. The increased translation speed (at a fixed ΔH) will decrease the droplet condensation size (much like the preliminary results presented previously, see Fig. 4.5). This process can be repeated over the entire length of the substrate, creating multiple regions of deposition based on the size of droplet condensation (shown in Fig. 5.3). This methodology provides a direct comparison of droplet condensation rate/size to deposition amount/quality. As all parameters (droplet size, vapor field convection pattern, dispersion quality, etc.) are identical between each region, post-analysis can compare uniformity of deposition and concentration of GO deposited side-by-side. This effort is to test the hypothesis that (1) large condensation droplets will result in deposition identical to drop casting and (2) minimizing droplet condensation size will mitigate the *coffee-ring* effect, producing uniform materials.

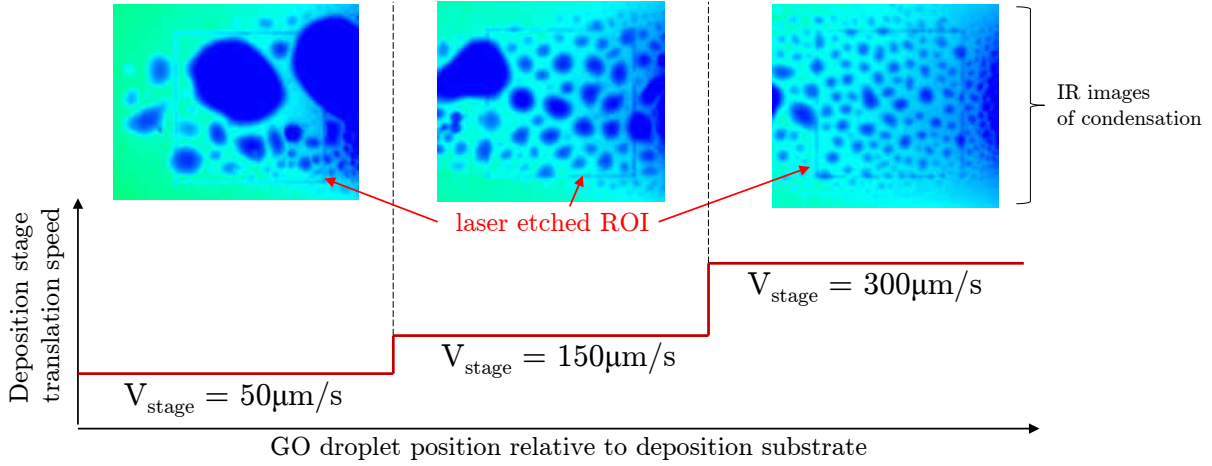


Figure 5.3: Multiple ROI are etched on a single Si wafer in series, each undergoing a deposition at a different rate. After depositing at a speed v_1 , a the translation speed is increased (decreased) to v_2 decreasing (increasing) the condensation rate for a different material thickness. This process can be repeated to obtain various material thicknesses on a single wafer.

5.4. Importance of Deposition Substrate Heat Sink

Upon further testing, the importance of a heat sink being attached to the translating silicon wafer became apparent. In efforts to improve the mounting system for the silicon wafer, revers tweezers were attached to the translation stages (see Fig. 5.4a). A non-adhesive mounting approach is a more efficient for quick installation; most importantly, it will keep the wafer surface clean (leaving no argument for contamination over the entire surface). Performing identical experiments performed in Chapter 4 (specifically, Section 4.3.3.2), the wafer did not accumulate condensation (see, Fig. 5.4c) – regardless of the height above the apex and translation speed (including stalled).

Analysis of the IR images captured show subtle localized heating within the standard condensation trail (see, Figs. 5.4b & 5.4d). This heating is created by the vapor phase (at a temperature below the substrate surface temperature, yet above room temperature [104]). While this heating is minimal ($\sim 1^\circ\text{C}$ based on IR measurements), it is hypothesized that the vapor is increasing the surface to the saturation temperature – thus remaining as

vapor. To correct this issue, the wafer is mounted to a heat sink to maintain the wafer at a room (sub-saturation) temperature (shown in Fig. 5.4c). The heat sink is simply a large thermal mass block of aluminum, left to equilibrate at room temperature (20°C). Effectively, the base mount of the Si wafer is held at room temperature. The Si wafer has a high thermal conductivity ($\sim 150\text{W/mK}$), thus the localized cooling by the vapor phase does not have enough energy to overcome the heat dissipation by the heat sink to cool the substrate to sub-saturation temperatures. An alternative to mounting a heat sink includes cooling the substrate (e.g., with a thermoelectric cooler), increasing the condensation rate (thus, possibly increasing the deposition rate).

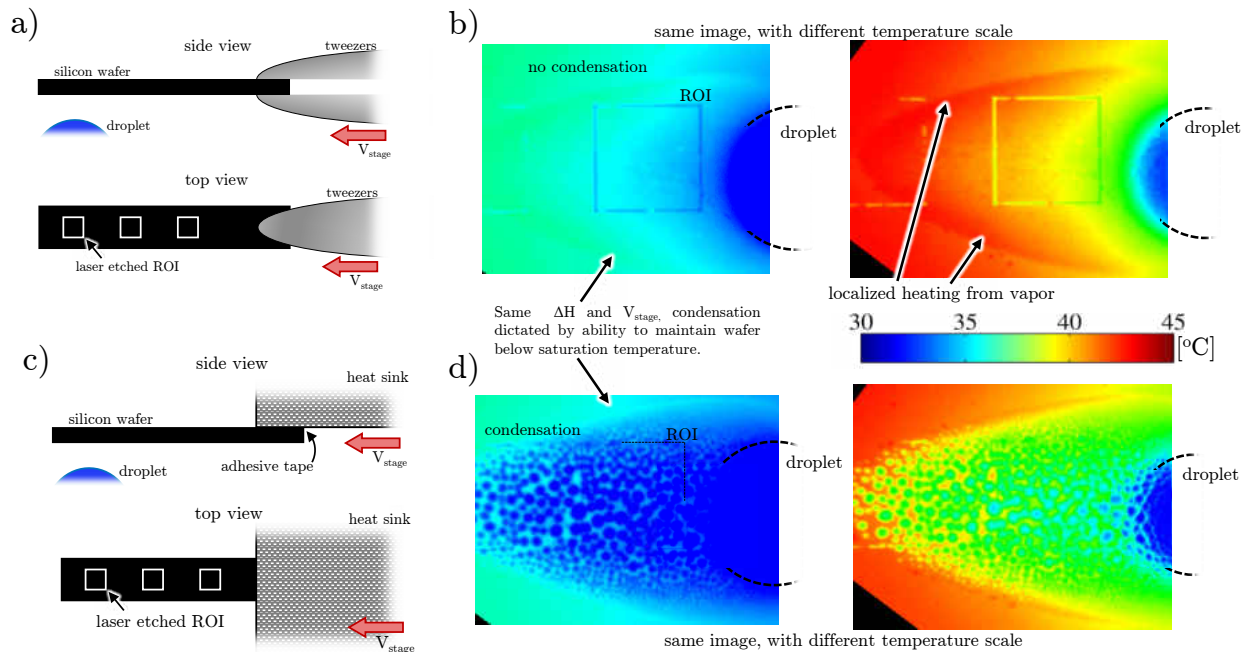


Figure 5.4: A heat sink must be attached to the Si wafer to maintain its temperature below the dew point. Without a sufficient heat sink (a), condensation will not form on the substrate (b). A heat sink (c) assists in maintaining a sub-dew point temperature (room temperature) to promote condensation (d); thus depositing GO.

5.5. Re-evaluation of Condensation Rates Versus Substrate Height

This section expands on the preliminary results presented in Section 4.2.2, specifically Fig. 4.4. It was realized an approximate *figure of merit* will be highly beneficial in regards to the scalability and reproducibility of this technique. While previous results (Fig. 4.4) were sufficient for preliminary ‘proof-of-concept’ work, the time permitted for detailed analysis. Additionally, the laser etched ROI’s (a concept implemented post-section 4.2.2) became crucial for defining a reference location to accurately compare condensation amount at multiple translation speeds. To measure the condensation rates, an image analysis script built in the ImageJ software [130] is used. For these experiments, an EVD procedure (see Section 4.1.3) is replicated, replacing the evaporating GO solution with pure DI water. A series of experiments, varying the translation speed while keeping the height difference (ΔH) constant, are performed (see Fig. 5.5).

Using a laser etched Si wafer (see Fig. 5.1), the ROI is tracked using the IR camera. The Si wafer is position so the ROI translates centered about the droplets apex. Once the ROI passes over the evaporating droplet (specifically, once the back side of the ROI square is $\sim 500\mu\text{m}$ beyond the droplet radius), an IR image is captured (see Fig. 5.5b). A series of image manipulations (cropping, applying filters, etc.) are performed in ImageJ to determine each condensate contact line and calculates the contact area of each. The sequence of image analyses is overviewed in Fig. 5.5b. Proceeding, the droplet is assumed circular to calculate the equivalent contact radius. The contact angle is assumed constant for each (experimentally measured to be $40\pm 1^\circ$). Therefore, the volume of each droplet (also summed to find the approximate total volume of water condensed within the ROI) is calculated using Eq. (3.1). Based on the total volume condensed during the duration the ROI is ‘exposed’ to condensation (length of ROI ($1500\mu\text{m}$) divided by the translation speed), the condensation rate is calculated per unit area (within a $1.5\times 1.5\text{mm}$ square ROI).

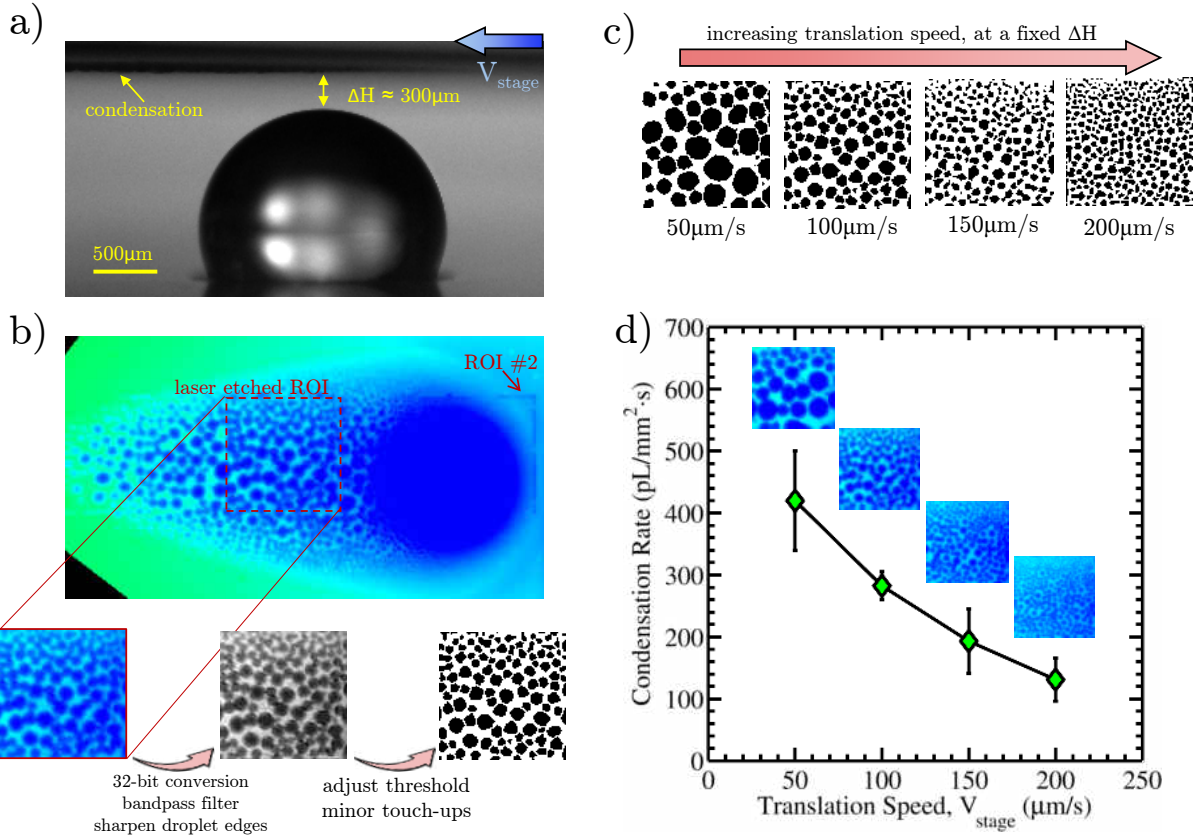


Figure 5.5: (a) Substrate translating over a steady-state evaporating droplet, with $\Delta H \approx 300\mu\text{m}$. (b) From IR image (located above droplet), image analysis procedure (using a ImageJ script [130]) used for detecting condensate droplets. (c) Comparison of condensation (radii and number of droplets) based on substrate translation speed (at a fixed ΔH of (a)). (d) Images from (c) are used to estimate the condensation rate, plotted vs. translation speed. Results show condensation rate is independent of substrate translation speed.

A sample set of images is shown in Fig. 5.5 of condensation formed within the same ROI and height difference. As the translation speed is increased, an increase in number of droplets with a smaller contact area can be clearly seen. The total volume, although not apparent, decreases with increasing speed. The increased translation speed ‘exposes’ the ROI to the vapor convection of the droplet over a shorter duration. With this, the condensation rate is *dependent* of substrate translation speed as shown in Fig. 5.5. This supports the initial hypothesis (e.g., Fig. 4.4), that condensation rate is dependent on both substrate height difference (ΔH) and substrate translation speed.

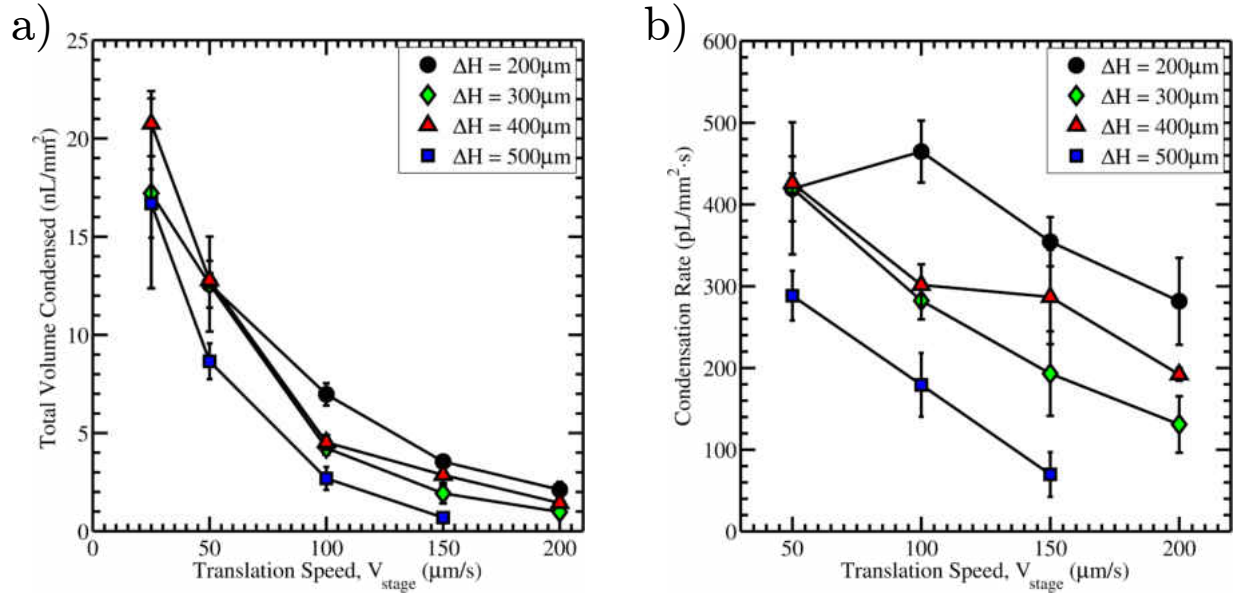


Figure 5.6: a) Total volume of vapor condensed on the translating wafer at multiple height differences. b) based on the total volume condensed and the translation speed, the condensation rate is calculated. Results show height difference and translation speed both have an influence on the condensation rate.

Further testing includes repeating this series of tests at multiple ΔH to supporting the height dependence on condensation rate. The total volume of vapor condensed follows a hyperbolic trend (agreeing with ones intuition, see Fig. 5.6a). While the trends for each ΔH seem to cross each other at slower translation speeds (e.g., higher condensation rate at $\Delta H=400\mu\text{m}$ compared to $\Delta H=300\mu\text{m}$), the larger error bars is attributed to this. Shown in Fig. 5.6a, the total volume of vapor condensed onto the substrate follows predicted trends. As the substrate approaches a ‘stall’, the condensation will continuously accumulate (to a volume of $V \rightarrow \infty$). Increasing the translation speed high enough will mitigate any nucleation coalescence, thus seemingly eliminating condensation. When calculating the condensation rates at various height differences, Fig. 5.6b shows a condensation rate dependence on both translation speed and height difference. As hypothesized from preliminary results (see Section 4.2.2), a conclusion is made on a height and speed dependence on the condensation rate.

5.6. Improved Deposition Results

With the improved experimental setup detailed throughout this chapter, the deposition quality made a significant improvement. The greatest limitation in quality deposits is believed to be both (1) the stability of the GO dispersion, and (2) the condensate size on the Si wafer. Using a highly stable GO dispersion mitigated the agglomeration during an EVD, and results show a significant improvement in the deposition concentration (see Figs. 5.7 and 5.8). Controlling the condensation rate/size (a combination of (i) translation speed, V_{stage} and (ii) height difference between droplet apex and Si substrate, ΔH) will affect both uniformity and concentration/thickness of the deposit. This is well demonstrated between the results in Figs. 5.7 and 5.8.

Figure 5.7 overviews an EVD using Solution C with parameters: translation speed, $V_{stage} = 50\mu\text{m/s}$ and height difference, $\Delta H = 500\mu\text{m} \pm 120\mu\text{m}$. The condensate formed within the ROI (see dashed lines, Fig. 5.7b) is large because of the droplet coalescence that occurs during a lower translation speed (higher condensation rate, see Fig. 5.6). Viewing the GO deposited (see Figs. 5.7c and 5.7d), a significant improvement in concentration is demonstrated over previous depositions with Solution B' (see Fig. 4.10). The Raman scans show expected magnitudes of the D-, G-, and 2D-bands; comparable with the other results presented previously and validate the Sulfite functional groups have no effect on GO Raman activity. The structure of the 2D-band leads to the assumption the images flakes are bulk (>10 layers).

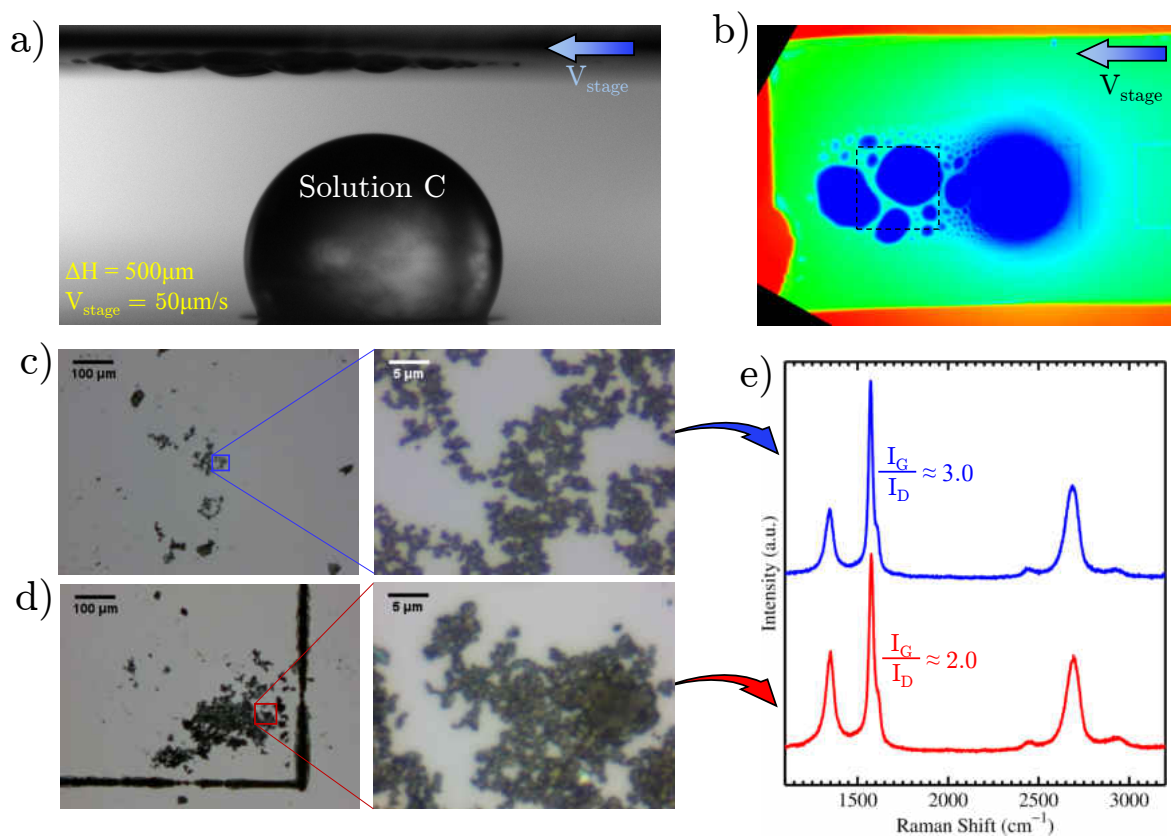


Figure 5.7: a) EVD experiment using Solution C, $V_{stage} = 50\mu\text{m/s}$, and $\Delta H = 500\mu\text{m} \pm 120\mu\text{m}$. b) Above IR image of (a). A significant amount of GO is shown in (c) and (d); with (c) near the center of the ROI and (d) top right corner of the ROI in the IR image (b). Raman results (e) show deposits are GO.

As shown in Figs. 5.7c and 5.7d, the deposited GO lacks uniformity within the ROI; presumably due to larger condensate reverting back to the capillary flow as with drop casting (see Fig. 4.8). To support this conclusion, these results are compared to another EVD with parameters: translation speed, $V_{stage} = 100\mu\text{m/s}$ and height difference, $\Delta H = 300\mu\text{m} \pm 80\mu\text{m}$; mitigating droplet coalescence (see Fig. 5.8b). An overview of the entire ROI is shown in Fig. 5.8c. A zoomed in image shows that the flakes are still fairly cluttered, but these size flakes are more dispersed over the entire ROI. While it is possible that monolayer GO is deposited throughout the ROI (which went undetected due to lack of proper equipment such as AFM, SEM or TEM), further work on controlling the condensation size remains the main argument

for idealizing EVD. Additionally, non-monolayer deposits could be a result of the solutions using in this work, where monolayer production with EVD becomes possible for a different synthesis/solution. Nevertheless, a large contribution has been presented in development of EVD for depositing GO, and opens a great number of future studies/development in large scale production of 2D materials.

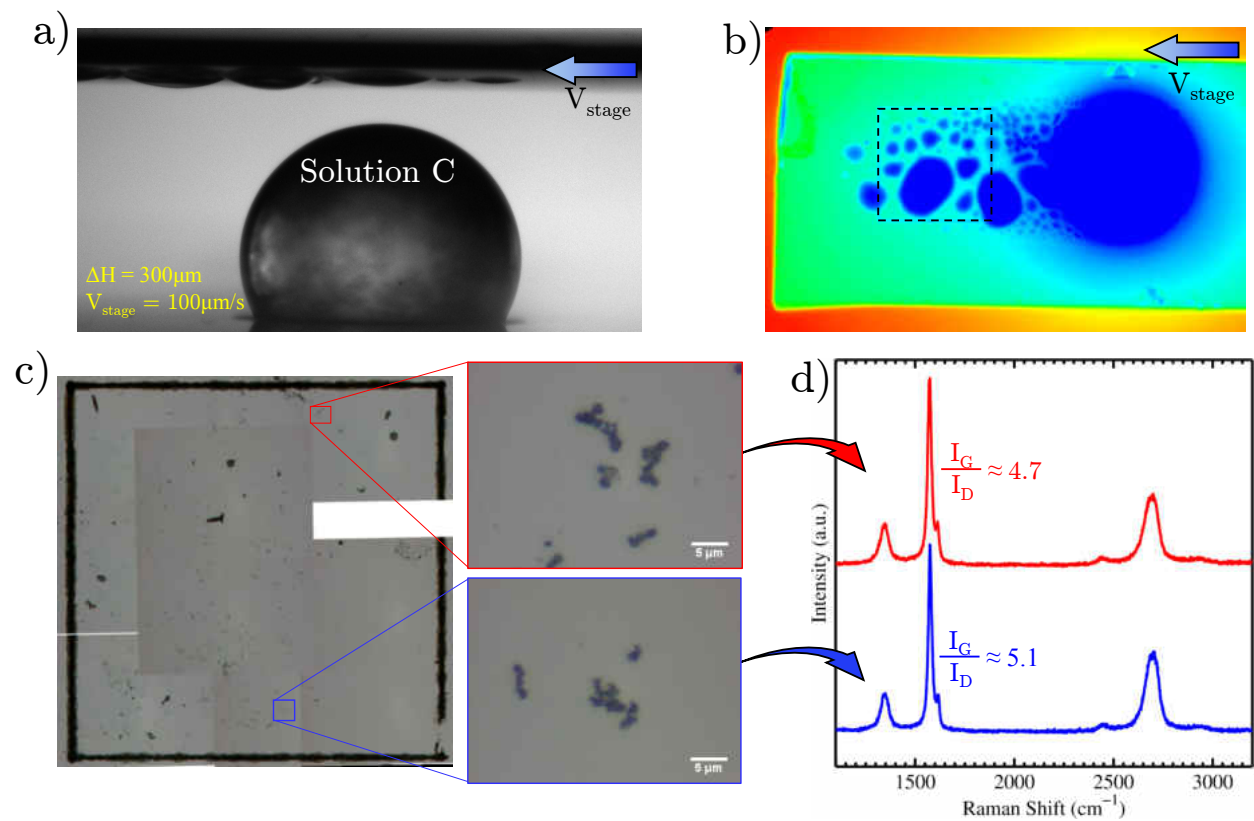


Figure 5.8: a) EVD experiment using Solution C, $V_{\text{stage}} = 100\mu\text{m/s}$, and $\Delta H = 300\mu\text{m} \pm 80\mu\text{m}$. b) Above IR image of (a). c) Deposition is less concentrated compared to Fig. 5.7, but more disperse. Raman results (d) show the deposited flakes are GO and comparable to Fig. 5.7e.

CHAPTER 6: CONCLUSIONS

6.1. Overview

A new technique is presented for depositing atomically-thin/2D materials to arbitrary substrates, termed Evaporative Vapor Deposition (EVD). This work has focused on forming thin film graphene oxide (GO) on silicon wafers. A droplet of a GO solution dispersed in water is formed on a heated polymer substrate. From past work [97, 102], the droplets contact line dynamics are controlled by a laser patterned trench. A fluid channel located within the substrate allows continuous supply of GO solution to the droplet using a computer controlled syringe pump, controlling the droplets contact angle. Carefully selecting the pump rate, the inlet rate is matched to the droplets evaporation rate to form a constant volume steady-state evaporating droplet [97].

A silicon wafer is translated through the vapor field of the evaporating GO droplet using a computer controlled translation stage. A large thermal mass (heat sink) is attached to the wafer to regulate the temperature of the Si wafer, maintaining it below the dew point to induce condensation. Dropwise condensation formed on the silicon wafer is monitored using both optical and infrared cameras. The condensation rate is calculated to be within $\sim 50\text{pL}/\text{mm}^2\text{s} - 500\text{pL}/\text{mm}^2\text{s}$ and dependent on both (1) height difference between the droplet's apex and substrate surface and (2) substrate translation speed. The wafer translation speed dictates the condensate droplet size and quantity (i.e., total volume). Nano-sized GO flakes carried through the vapor phase are captured in the condensate, depositing on the translating wafer. Deposition rate is discovered to be dependent on the stability of the solution and droplet condensate size. For example, deposition remained limited for solutions which agglomerated over a short period of time. For highly stable well-dispersed solutions

(i.e., Solution D, see Table 4.1), the amount deposited significantly increased. Additionally, highly concentrated deposition regions were found for larger droplets (i.e., slow translation speed resulting in significant droplet coalescence). Keeping droplet condensate small is hypothesized to produce more uniform material deposits.

Characterization with Raman spectroscopy show expected shifts for graphene/graphite. Preliminary results show various quality deposits (e.g., FLG shown in Fig. 4.10 to different defect concentrations shown in Fig. 4.9). The deposition occurs at low temperatures ($<100^{\circ}\text{C}$) allowing direct deposition to arbitrary substrates; an advantage over CVD. Additionally, increasing the vapor convection field (either increasing the size or number of droplets) increases the deposition region – demonstrating scalability. This presented EVD demonstrates a promising technique toward formation of large scale 2D materials with applications to developing new technologies.

6.2. Future Work

There is a large number of experiments which can really expand the characterization and development of Evaporative Vapor Deposition; unfortunately, time did not permit to work on them. First, expanding on the characterization of the graphene deposited with AFM, XPS, SEM/TEM, etc. are in the works but scheduled after the completion of this thesis. Raman spectroscopy provided great results, but limited to determining the thickness of the deposited graphene. Additionally, a large advantage to EVD is the low temperature deposition over CVD. XPS can compare the surface functionality of the EVD deposited GO and compare to the solution itself, and test whether these functionalities are lost (in the case of CVD, the extreme temperature strip the synthesized GO of various functionalities which are needed for some technologies).

A second important line of experiments of this work (also, are scheduled to be performed after the completion of this thesis) includes deposited various materials. Molybdenum disulfide (MoS_2) is another high interest monolayer materials which can be liquid exfoliated [44]. Monolayer Lithium Cobalt Oxide (LiCoO_2) has interest in energy storage (e.g., battery development), which is also in the process of being dispersed in a DI water solution at the completion of this thesis. This series of experiments will demonstrate the versatility of EVD, not limiting to the formation of GO. For updates/progress on this work, I refer the reader to search for a peer-reviewed manuscript publication proceeding the completion of this thesis.

It is highly suggested to perform EVD within a clean room. There was a consistent battle with contamination (e.g., dust) when exposing the wafer during deposition. The quality of monolayer graphene (or other monolayer materials) is severely compromised with contamination of dust, a main limiting factor to keeping this work as a ‘proof-of-concept.’ All characterization techniques (XPS, AFM, and Raman) become difficult to study with contaminants, which will significantly reduce/eliminate when performed in a clean room.

Another important aspect of the developed EVD technique is the scalability, which was not explored directly. All experiments used the same size droplet ($R \cong 1200\mu\text{m}$), thus depositing over similar lateral dimensions. There are various methods for depositing on a larger scale, including: (1) increasing the droplet size, (2) creating a series of droplets for increasing the depth of deposition, and (3) a matrix of droplets. This requires additional substrate fabrication techniques, mainly creating a large number of fluid channels within the substrate. The fabrication techniques using in this work are not ideal for fabricating such substrates, but there are various methods (e.g., photolithography) left to the reader to investigate for creating such arrays of fluid channels for increasing the scale of EVD deposition.

A large portion of this work is empirical. The ability for a vapor to carry nanoparticles has been demonstrated, yet the mechanism remains unknown. The presence of a vapor phase

cage structure of water may be entrapping nanoparticles, although only liquid phase cage structures have been reported. Whether or not a cage structure exists in the vapor phase, the mechanism for vapor to carry nanoparticle opens an interesting topic for theorists to investigate.

REFERENCES

- [1] A. K. Geim and K. S. Novoselov. The Rise of Graphene. *Nature Materials*, 6(3):183–191, 2007.
- [2] V. Nicolosi, M. Chhowalla, M. G. Kanatzidis, M. S. Strano, and J. N. Coleman. Liquid Exfoliation of Layered Materials. *Science*, 340(6139), 2013.
- [3] K. I. Bolotin, K. Sikes, Z. Jiang, M. Klima, G. Fudenberg, J. Hone, P. Kim, and H. Stormer. Ultrahigh Electron Mobility in Suspended Graphene. *Solid State Communications*, 146(9):351–355, 2008.
- [4] A. A. Balandin, S. Ghosh, W. Bao, I. Calizo, D. Teweldebrhan, F. Miao, and C. N. Lau. Superior Thermal Conductivity of Single-Layer Graphene. *Nano Letters*, 8(3):902–907, 2008.
- [5] C. Lee, X. Wei, J. W. Kysar, and J. Hone. Measurement of the Elastic Properties and Intrinsic Strength of Monolayer Graphene. *Science*, 321(5887):385–388, 2008.
- [6] W. Boggs, A. Cook, R. Gore, K. Harris, and M. Jasiukowicz. NASA LSP Vapor Migration Test Equipment Design. In *Proceedings of the 2013 Conference on Thermal and Fluid Analysis Workshop (TFAWS)*, 2013.
- [7] Carbon Nanotube Sensors for Gas Detection. http://www.nasa.gov/centers/ames/research/technology-onepagere/gas_detection.html, 2008. Online; accessed Aug. 2014.
- [8] J. T. Robinson, F. K. Perkins, E. S. Snow, Z. Wei, and P. E. Sheehan. Reduced Graphene Oxide Molecular Sensors. *Nano Letters*, 8(10):3137–3140, 2008.
- [9] F. K. Perkins, A. L. Friedman, E. Cobas, P. Campbell, G. Jernigan, and B. T. Jonker. Chemical Vapor Sensing with Monolayer MoS₂. *Nano Letters*, 13(2):668–673, 2013.
- [10] H. J. Yoon, J. H. Yang, Z. Zhou, S. S. Yang, M. M.-C. Cheng, et al. Carbon Dioxide Gas Sensor Using a Graphene Sheet. *Sensors and Actuators B: Chemical*, 157(1):310–313, 2011.
- [11] K. S. Novoselov, A. K. Geim, S. V. Morozov, D. Jiang, Y. Zhang, S. V. Dubonos, I. V. Grigorieva, and A. A. Firsov. Electric Field Effect in Atomically Thin Carbon Films. *Science*, 306(5696):666–669, 2004.
- [12] S. Stankovich, D. A. Dikin, R. D. Piner, K. A. Kohlhaas, A. Kleinhammes, Y. Jia, Y. Wu, S. T. Nguyen, and R. S. Ruoff. Synthesis of Graphene-Based Nanosheets via Chemical Reduction of Exfoliated Graphite Oxide. *Carbon*, 45(7):1558–1565, 2007.
- [13] X. Li, W. Cai, J. An, S. Kim, J. Nah, D. Yang, R. Piner, A. Velamakanni, I. Jung, E. Tutuc, et al. Large-Area Synthesis of High-Quality and Uniform Graphene Films on Copper Foils. *Science*, 324(5932):1312–1314, 2009.
- [14] P. R. Wallace. The Band Theory of Graphite. *Physical Review*, 71(9):622, 1947.
- [15] J. McClure. Diamagnetism of Graphite. *Physical Review*, 104(3):666, 1956.
- [16] N. D. Mermin. Crystalline Order in Two Dimensions. *Physical Review*, 176(1):250, 1968.
- [17] L. Landau and E. Lifshitz. Statistical Physics, Part I. *Course of Theoretical Physics*, 5:468, 1980.
- [18] J. Evans, P. Thiel, and M. C. Bartelt. Morphological Evolution During Epitaxial Thin Film Growth: Formation of 2D Islands and 3D Mounds. *Surface Science Reports*, 61(1):1–128, 2006.

- [19] J. Venables, G. Spiller, and M. Hanbucken. Nucleation and Growth of Thin Films. *Reports on Progress in Physics*, 47(4):399, 1984.
- [20] J. C. Meyer, A. K. Geim, M. Katsnelson, K. Novoselov, T. Booth, and S. Roth. The Structure of Suspended Graphene Sheets. *Nature*, 446(7131):60–63, 2007.
- [21] P. Blake, E. Hill, A. C. Neto, K. Novoselov, D. Jiang, R. Yang, T. Booth, and A. Geim. Making Graphene Visible. *Applied Physics Letters*, 91(6):063124, 2007.
- [22] V. Singh, D. Joung, L. Zhai, S. Das, S. I. Khondaker, and S. Seal. Graphene Based Materials: Past, Present and Future. *Progress in Materials Science*, 56(8):1178–1271, 2011.
- [23] S. Horiuchi, T. Gotou, M. Fujiwara, T. Asaka, T. Yokosawa, and Y. Matsui. Single Graphene Sheet Detected in a Carbon Nanofilm. *Applied Physics Letters*, 84(13):2403–2405, 2004.
- [24] L. M. Viculis, J. J. Mack, and R. B. Kaner. A Chemical Route to Carbon Nanoscrolls. *Science*, 299(5611):1361–1361, 2003.
- [25] S. Gilje, S. Han, M. Wang, K. L. Wang, and R. B. Kaner. A Chemical Route to Graphene for Device Applications. *Nano Letters*, 7(11):3394–3398, 2007.
- [26] J. Paredes, S. Villar-Rodil, A. Martinez-Alonso, and J. Tascon. Graphene Oxide Dispersions in Organic Solvents. *Langmuir*, 24(19):10560–10564, 2008.
- [27] H. C. Schniepp, J.-L. Li, M. J. McAllister, H. Sai, M. Herrera-Alonso, D. H. Adamson, R. K. Prud’homme, R. Car, D. A. Saville, and I. A. Aksay. Functionalized Single Graphene Sheets Derived from Splitting Graphite Oxide. *The Journal of Physical Chemistry B*, 110(17):8535–8539, 2006.
- [28] S. Stankovich, D. A. Dikin, G. H. Dommett, K. M. Kohlhaas, E. J. Zimney, E. A. Stach, R. D. Piner, S. T. Nguyen, and R. S. Ruoff. Graphene-Based Composite Materials. *Nature*, 442(7100):282–286, 2006.
- [29] V. C. Tung, M. J. Allen, Y. Yang, and R. B. Kaner. High-throughput Solution Processing of Large-Scale Graphene. *Nature Nanotechnology*, 4(1):25–29, 2008.
- [30] Y. Zhu, S. Murali, W. Cai, X. Li, J. W. Suk, J. R. Potts, and R. S. Ruoff. Graphene and Graphene Oxide: Synthesis, Properties, and Applications. *Advanced Materials*, 22(35):3906–3924, 2010.
- [31] S. Stankovich, R. D. Piner, X. Chen, N. Wu, S. T. Nguyen, and R. S. Ruoff. Stable Aqueous Dispersions of Graphitic Nanoplatelets via the Reduction of Exfoliated Graphite Oxide in the Presence of Poly(Sodium 4-Styrenesulfonate). *Journal of Materials Chemistry*, 16(2):155–158, 2006.
- [32] A. Lerf, H. He, M. Forster, and J. Klinowski. Structure of Graphite Oxide Revisited. *The Journal of Physical Chemistry B*, 102(23):4477–4482, 1998.
- [33] H. He, J. Klinowski, M. Forster, and A. Lerf. A New Structural Model for Graphite Oxide. *Chemical Physics Letters*, 287(1):53–56, 1998.
- [34] T. Nakajima and Y. Matsuo. Formation Process and Structure of Graphite Oxide. *Carbon*, 32(3):469–475, 1994.
- [35] D. Lee, L. De Los Santos V, J. Seo, L. L. Felix, A. Bustamante D, J. Cole, and C. Barnes. The Structure of Graphite Oxide: Investigation of its Surface Chemical Groups. *The Journal of Physical Chemistry B*, 114(17):5723–5728, 2010.

- [36] W. S. Hummers Jr and R. E. Offeman. Preparation of Graphitic Oxide. *Journal of the American Chemical Society*, 80(6):1339–1339, 1958.
- [37] N. I. Kovtyukhova, P. J. Ollivier, B. R. Martin, T. E. Mallouk, S. A. Chizhik, E. V. Buzaneva, and A. D. Gorchinskiy. Layer-by-Layer Assembly of Ultrathin Composite Films from Micron-sized Graphite Oxide Sheets and Oolycations. *Chemistry of Materials*, 11(3):771–778, 1999.
- [38] J. Wang, X. Wang, C. Xu, M. Zhang, and X. Shang. Preparation of Graphene/Poly(vinyl alcohol) Nanocomposites with Enhanced Mechanical Properties and Water Resistance. *Polymer International*, 60(5):816–822, 2011.
- [39] M. Herrera-Alonso, A. A. Abdala, M. J. McAllister, I. A. Aksay, and R. K. Prud’homme. Intercalation and Stitching of Graphite Oxide with Diaminoalkanes. *Langmuir*, 23(21):10644–10649, 2007.
- [40] S. Stankovich, R. D. Piner, S. T. Nguyen, and R. S. Ruoff. Synthesis and Exfoliation of Isocyanate-Treated Graphene Oxide Nanoplatelets. *Carbon*, 44(15):3342–3347, 2006.
- [41] S. Park and R. S. Ruoff. Chemical Methods for the Production of Graphenes. *Nature Nanotechnology*, 4(4):217–224, 2009.
- [42] J. T. Robinson, F. K. Perkins, E. S. Snow, Z. Wei, and P. E. Sheehan. Reduced Graphene Oxide Molecular Sensors. *Nano Letters*, 8(10):3137–3140, 2008.
- [43] J. D. Fowler, M. J. Allen, V. C. Tung, Y. Yang, R. B. Kaner, and B. H. Weiller. Practical Chemical Sensors from Chemically Derived Graphene. *ACS Nano*, 3(2):301–306, 2009.
- [44] K.-K. Liu, W. Zhang, Y.-H. Lee, Y.-C. Lin, M.-T. Chang, C.-Y. Su, C.-S. Chang, H. Li, Y. Shi, H. Zhang, et al. Growth of Large-Area and Highly Crystalline MoS₂ Thin Layers on Insulating Substrates. *Nano Letters*, 12(3):1538–1544, 2012.
- [45] S. J. Chae, F. Güneş, K. K. Kim, E. S. Kim, G. H. Han, S. M. Kim, H.-J. Shin, S.-M. Yoon, J.-Y. Choi, M. H. Park, et al. Synthesis of Large-Area Graphene Layers on Poly-Nickel Substrate by Chemical Vapor Deposition: Wrinkle Formation. *Advanced Materials*, 21(22):2328–2333, 2009.
- [46] Q. Yu, J. Lian, S. Siriponglert, H. Li, Y. P. Chen, and S.-S. Pei. Graphene Segregated on Ni Surfaces and Transferred to Insulators. *Applied Physics Letters*, 93(11):113103, 2008.
- [47] K. S. Kim, Y. Zhao, H. Jang, S. Y. Lee, J. M. Kim, K. S. Kim, J.-H. Ahn, P. Kim, J.-Y. Choi, and B. H. Hong. Large-Scale Pattern Growth of Graphene Films for Stretchable Transparent Electrodes. *Nature*, 457(7230):706–710, 2009.
- [48] Y. Lee, S. Bae, H. Jang, S. Jang, S.-E. Zhu, S. H. Sim, Y. I. Song, B. H. Hong, and J.-H. Ahn. Wafer-Scale Synthesis and Transfer of Graphene Films. *Nano Letters*, 10(2):490–493, 2010.
- [49] S. Lee, K. Lee, and Z. Zhong. Wafer Scale Homogeneous Bilayer Graphene Films by Chemical Vapor Deposition. *Nano Letters*, 10(11):4702–4707, 2010.
- [50] A. Ciesielski and P. Samori. Graphene Via Sonication Assisted Liquid-Phase Exfoliation. *Chemical Society Reviews*, 43(1):381–398, 2014.
- [51] Y. Hernandez, V. Nicolosi, M. Lotya, F. M. Blighe, Z. Sun, S. De, I. McGovern, B. Holland, M. Byrne, Y. K. Gun’Ko, et al. High-Yield Production of Graphene by Liquid-Phase Exfoliation of Graphite. *Nature Nanotechnology*, 3(9):563–568, 2008.

- [52] H. G. Jeon, Y. H. Huh, S. H. Yun, K. W. Kim, S. S. Lee, J. Lim, K.-S. An, and B. Park. Improved Homogeneity and Surface Coverage of Graphene Oxide Layers Fabricated by Horizontal-Dip-Coating for Solution-Processable Organic Semiconducting Devices. *Journal of Materials Chemistry C*, 2(14):2622–2634, 2014.
- [53] J. Kim, L. J. Cote, F. Kim, W. Yuan, K. R. Shull, and J. Huang. Graphene Oxide Sheets at Interfaces. *Journal of the American Chemical Society*, 132(23):8180–8186, 2010.
- [54] C.-J. Shih, A. Vijayaraghavan, R. Krishnan, R. Sharma, J.-H. Han, M.-H. Ham, Z. Jin, S. Lin, G. L. Paulus, N. F. Reuel, et al. Bi- and Trilayer Graphene Solutions. *Nature Nanotechnology*, 6(7):439–445, 2011.
- [55] R. D. Deegan, O. Bakajin, T. F. Dupont, G. Huber, S. R. Nagel, and T. A. Witten. Capillary Flow as the Cause of Ring Stains from Dried Liquid Drops. *Nature*, 389(6653):827–829, 1997.
- [56] M. Dicuungco, S. Dash, J. A. Weibel, and S. V. Garimella. Effect of Superhydrophobic Surface Morphology on Evaporative Deposition Patterns. *Applied Physics Letters*, 104(20):201604, 2014.
- [57] A. Askounis, K. Sefiane, V. Koutsos, and M. E. Shanahan. Effect of Particle Geometry on Triple Line Motion of Nano-Fluid Drops and Deposit Nano-Structuring. *Advances in Colloid and Interface Science*, 2014.
- [58] K. Sefiane. Patterns from Drying Drops. *Advances in Colloid and Interface Science*, 206:372–381, 2014.
- [59] P. J. Yunker, T. Still, M. A. Lohr, and A. Yodh. Suppression of the Coffee-Ring Effect by Shape-Dependent Capillary Interactions. *Nature*, 476(7360):308–311, 2011.
- [60] Y.-R. Kang, Y.-L. Li, and M.-Y. Deng. Precise Unzipping of Flattened Carbon Nanotubes to Regular Graphene Nanoribbons by Acid Cutting Along the Folded Edges. *Journal of Materials Chemistry*, 22(32):16283–16287, 2012.
- [61] D. V. Kosynkin, A. L. Higginbotham, A. Sinitskii, J. R. Lomeda, A. Dimiev, B. K. Price, and J. M. Tour. Longitudinal Unzipping of Carbon Nanotubes to form Graphene Nanoribbons. *Nature*, 458(7240):872–876, 2009.
- [62] L. Jiao, L. Zhang, X. Wang, G. Diankov, and H. Dai. Narrow Graphene Nanoribbons from Carbon Nanotubes. *Nature*, 458(7240):877–880, 2009.
- [63] B. Partoens and F. Peeters. From Graphene to Graphite: Electronic Structure Around the K Point. *Physical Review B*, 74(7):075404, 2006.
- [64] H. Cao, Q. Yu, R. Colby, D. Pandey, C. Park, J. Lian, D. Zemlyanov, I. Childres, V. Drachev, E. A. Stach, et al. Large-Scale Graphitic Thin Films Synthesized on Ni and Transferred to Insulators: Structural and Electronic Properties. *Journal of Applied Physics*, 107(4):044310, 2010.
- [65] K. S. Novoselov, D. Jiang, F. Schedin, T. J. Booth, V. V. Khotkevich, S. V. Morozov, and A. K. Geim. Two-Dimensional Atomic Crystals. *Proceedings of the National Academy of Sciences of the United States of America*, 102(30):10451–10453, 2005.
- [66] K. Novoselov, A. K. Geim, S. Morozov, D. Jiang, M. K. I. Grigorieva, S. Dubonos, and A. Firsov. Two-Dimensional Gas of Massless Dirac Fermions in Graphene. *Nature*, 438(7065):197–200, 2005.

- [67] C. Gómez-Navarro, R. T. Weitz, A. M. Bittner, M. Scolari, A. Mews, M. Burghard, and K. Kern. Electronic Transport Properties of Individual Chemically Reduced Graphene Oxide Sheets. *Nano Letters*, 7(11):3499–3503, 2007.
- [68] C.-Y. Su, Y. Xu, W. Zhang, J. Zhao, X. Tang, C.-H. Tsai, and L.-J. Li. Electrical and Spectroscopic Characterizations of Ultra-Large Reduced Graphene Oxide Monolayers. *Chemistry of Materials*, 21(23):5674–5680, 2009.
- [69] S. Ghosh, I. Calizo, D. Teweldebrhan, E. Pokatilov, D. Nika, A. Balandin, W. Bao, F. Miao, and C. N. Lau. Extremely High Thermal Conductivity of Graphene: Prospects for Thermal Management Applications in Nanoelectronic Circuits. *Applied Physics Letters*, 92(15):151911–151911, 2008.
- [70] J. H. Seol, I. Jo, A. L. Moore, L. Lindsay, Z. H. Aitken, M. T. Pettes, X. Li, Z. Yao, R. Huang, D. Broido, et al. Two-Dimensional Phonon Transport in Supported Graphene. *Science*, 328(5975):213–216, 2010.
- [71] T. Schwamb, B. R. Burg, N. C. Schirmer, and D. Poulikakos. An Electrical Method for the Measurement of the Thermal and Electrical Conductivity of Reduced Graphene Oxide Nanostructures. *Nanotechnology*, 20(40):405704, 2009.
- [72] Y. K. Koh, M.-H. Bae, D. G. Cahill, and E. Pop. Heat Conduction Across Monolayer and Few-Layer Graphenes. *Nano Letters*, 10(11):4363–4368, 2010.
- [73] J. C. Meyer, C. Kisielowski, R. Erni, M. D. Rossell, M. Crommie, and A. Zettl. Direct Imaging of Lattice Atoms and Topological Defects in Graphene Membranes. *Nano Letters*, 8(11):3582–3586, 2008.
- [74] A. C. Ferrari, J. C. Meyer, V. Scardaci, C. Casiraghi, M. Lazzeri, F. Mauri, S. Piscanec, D. Jiang, K. S. Novoselov, S. Roth, and A. K. Geim. Raman Spectrum of Graphene and Graphene Layers. *Physical Review Letters*, 97(18):187401, 2006.
- [75] A. Gupta, G. Chen, P. Joshi, S. Tadigadapa, and P. C. Eklund. Raman Scattering from High-Frequency Phonons in Supported n-Graphene Layer Films. *Nano Letters*, 6(12):2667–2673, 2006.
- [76] Y. K. Koh, M.-H. Bae, D. G. Cahill, and E. Pop. Reliably Counting Atomic Planes of Few-Layer Graphene ($n > 4$). *ACS Nano*, 5(1):269–274, 2010.
- [77] S. Reich and C. Thomsen. Raman Spectroscopy of Graphite. *Philosophical Transactions of the Royal Society of London. Series A: Mathematical, Physical and Engineering Sciences*, 362(1824):2271–2288, 2004.
- [78] F. Tuinstra and J. L. Koenig. Raman Spectrum of Graphite. *The Journal of Chemical Physics*, 53(3):1126–1130, 1970.
- [79] E. M. Ferreira, M. V. Moutinho, F. Stavale, M. Lucchese, R. B. Capaz, C. Achete, and A. Jorio. Evolution of the Raman Spectra from Single-, Few-, and Many-Layer Graphene with Increasing Disorder. *Physical Review B*, 82(12):125429, 2010.
- [80] A. Eckmann, A. Felten, A. Mishchenko, L. Britnell, R. Krupke, K. S. Novoselov, and C. Casiraghi. Probing the Nature of Defects in Graphene by Raman Spectroscopy. *Nano Letters*, 12(8):3925–3930, 2012.
- [81] T. Young. An Essay on the Cohesion of Fluids. *Philosophical Transactions of the Royal Society of London*, 95:65–87, 1805.

- [82] M. Potash and P. Wayner. Evaporation from a Two-Dimensional Extended Meniscus. *International Journal of Heat and Mass Transfer*, 15(10):1851–1863, 1972.
- [83] W.-J. Chung, J.-W. Oh, K. Kwak, B. Y. Lee, J. Meyer, E. Wang, A. Hexemer, and S.-W. Lee. Biomimetic Self-Templating Supramolecular Structures. *Nature*, 478(7369):364–368, 2011.
- [84] P. Abgrall and A. Gue. Lab-on-Chip Technologies: Making a Microfluidic Network and Coupling it into a Complete Microsystem – A Review. *Journal of Micromechanics and Microengineering*, 17(5):R15, 2007.
- [85] V. Srinivasan, V. K. Pamula, and R. B. Fair. An Integrated Digital Microfluidic Lab-on-a-Chip for Clinical Diagnostics on Human Physiological Fluids. *Lab on a Chip*, 4(4):310–315, 2004.
- [86] M. G. Pollack, R. B. Fair, and A. D. Shenderov. Electrowetting-Based Actuation of Liquid Droplets for Microfluidic Applications. *Applied Physics Letters*, 77(11):1725–1726, 2000.
- [87] K. H. Kang. How Electrostatic Fields Change Contact Angle in Electrowetting. *Langmuir*, 18(26):10318–10322, 2002.
- [88] J. D. Wehking and R. Kumar. Droplet Actuation in an Electrified Microfluidic Network. *Lab on a Chip*, 15(3):793–801, 2015.
- [89] V. A. Ganesh, H. K. Raut, A. S. Nair, and S. Ramakrishna. A Review on Self-Cleaning Coatings. *Journal of Materials Chemistry*, 21(41):16304–16322, 2011.
- [90] T. Krupenkin and J. A. Taylor. Reverse Electrowetting as a New Approach to High-Power Energy Harvesting. *Nature Communications*, 2:448, 2011.
- [91] S. A. Putnam, A. M. Briones, J. S. Ervin, M. S. Hanchak, L. W. Byrd, and J. G. Jones. Interfacial Heat Transfer During Microdroplet Evaporation on a Laser Heated Surface. *International Journal of Heat and Mass Transfer*, 55(23):6307–6320, 2012.
- [92] P. C. Wayner. The Effect of Interfacial Mass Transport on Flow in Thin Liquid Films. *Colloids and Surfaces*, 52:71–84, 1991.
- [93] J. L. Plawsky, M. Ojha, A. Chatterjee, and P. C. Wayner Jr. Review of the Effects of Surface Topography, Surface Chemistry, and Fluid Physics on Evaporation at the Contact Line. *Chemical Engineering Communications*, 196(5):658–696, 2008.
- [94] S. A. Putnam, A. M. Briones, L. W. Byrd, J. S. Ervin, M. S. Hanchak, A. White, and J. G. Jones. Microdroplet Evaporation on Superheated Surfaces. *International Journal of Heat and Mass Transfer*, 55(21):5793–5807, 2012.
- [95] W. Deng and A. Gomez. Electrospray Cooling for Microelectronics. *International Journal of Heat and Mass Transfer*, 54(11):2270–2275, 2011.
- [96] J. Kim. Spray Cooling Heat Transfer: The State of the Art. *International Journal of Heat and Fluid Flow*, 28(4):753–767, 2007.
- [97] H. Voota, K. Gleason, and S. Putnam. Steady State Water Droplet Evaporation. *unpublished*, 2015.
- [98] R. D. Deegan, O. Bakajin, T. F. Dupont, G. Huber, S. R. Nagel, and T. A. Witten. Contact Line Deposits in an Evaporating Drop. *Physical Review E*, 62(1):756, 2000.

- [99] B. Park and M.-y. Han. Organic Light-Emitting Devices Fabricated Using a Premetered Coating Process. *Optics Express*, 17(24):21362–21369, 2009.
- [100] Private Communications with Shawn A. Putnam.
- [101] R. W. Fox, A. T. McDonald, and P. J. Pritchard. *Introduction to Fluid Mechanics*. John Wiley & Sons, 2006.
- [102] K. Gleason and S. A. Putnam. Microdroplet Evaporation with a Forced Pinned Contact Line. *Langmuir*, 30(34):10548–10555, 2014.
- [103] K. Gleason. Experimental and Numerical Investigations of Microdroplet Evaporation with a Forced Pinned Contact Line. *Honors Undergraduate Thesis*, May 2014. University of Central Florida.
- [104] K. Gleason and S. A. Putnam. Simulating the Evaporation of Pinned Water Microdroplets with Implementation of a Surface Concentration Distribution. In *Thermal and Thermomechanical Phenomena in Electronic Systems (ITherm), 2014 IEEE Intersociety Conference on*, pages 1222–1227. IEEE, 2014.
- [105] C. Bourges-Monnier and M. Shanahan. Influence of Evaporation on Contact Angle. *Langmuir*, 11(7):2820–2829, 1995.
- [106] P.-G. De Gennes. Wetting: Statics and Dynamics. *Reviews of Modern Physics*, 57(3):827, 1985.
- [107] J. Stauber, S. Wilson, B. Duffy, and K. Sefiane. On the Lifetimes of Evaporating Droplets. *Journal of Fluid Mechanics*, 744:R2, 2014.
- [108] E. F. Crafton and W. Black. Heat Transfer and Evaporation Rates of Small Liquid Droplets on Heated Horizontal Surfaces. *International Journal of Heat and Mass Transfer*, 47(6):1187–1200, 2004.
- [109] T. A. Nguyen and A. V. Nguyen. Increased Evaporation Kinetics of Sessile Droplets by Using Nanoparticles. *Langmuir*, 28(49):16725–16728, 2012.
- [110] C. Extrand. Water Contact Angles and Hysteresis of Polyimide Surfaces. *Journal of Colloid and Interface Science*, 248(1):136–142, 2002.
- [111] P. G. Pittoni, C.-C. Chang, T.-S. Yu, and S.-Y. Lin. Evaporation of Water Drops on Polymer Surfaces: Pinning, Depinning and Dynamics of the Triple Line. *Colloids and Surfaces A: Physicochemical and Engineering Aspects*, 432:89–98, 2013.
- [112] H. Eral, D. 't Mannetje, and J. Oh. Contact Angle Hysteresis: A Review of Fundamentals and Applications. *Colloid and Polymer Science*, 291(2):247–260, 2013.
- [113] L. Gao and T. J. McCarthy. How Wenzel and Cassie Were Wrong. *Langmuir*, 23(7):3762–3765, 2007.
- [114] M. Lotya, Y. Hernandez, P. J. King, R. J. Smith, V. Nicolosi, L. S. Karlsson, F. M. Blighe, S. De, Z. Wang, I. McGovern, et al. Liquid Phase Production of Graphene by Exfoliation of Graphite in Surfactant/Water Solutions. *Journal of the American Chemical Society*, 131(10):3611–3620, 2009.
- [115] S. Wang, Y. Zhang, N. Abidi, and L. Cabrales. Wettability and Surface Free Energy of Graphene Films. *Langmuir*, 25(18):11078–11081, 2009.
- [116] S. D. Park, S. W. Lee, S. Kang, I. C. Bang, J. H. Kim, H. S. Shin, D. W. Lee, and D. W. Lee. Effects of Nanofluids Containing Graphene/Graphene-Oxide Nanosheets on Critical Heat Flux. *Applied Physics Letters*, 97(2):023103, 2010.

- [117] F. Kim, L. J. Cote, and J. Huang. Graphene Oxide: Surface Activity and Two-Dimensional Assembly. *Advanced Materials*, 22(17):1954–1958, 2010.
- [118] Y. Si and E. T. Samulski. Synthesis of Water Soluble Graphene. *Nano Letters*, 8(6):1679–1682, 2008.
- [119] D. Li, M. B. Müller, S. Gilje, R. B. Kaner, and G. G. Wallace. Processable Aqueous Dispersions of Graphene Nanosheets. *Nature Nanotechnology*, 3(2):101–105, 2008.
- [120] Private Communications with Shashank Saraf.
- [121] Z. Pan, S. Dash, J. A. Weibel, and S. V. Garimella. Assessment of Water Droplet Evaporation Mechanisms on Hydrophobic and Superhydrophobic Substrates. *Langmuir*, 29(51):15831–15841, 2013.
- [122] S. Dash and S. V. Garimella. Droplet Evaporation Dynamics on a Superhydrophobic Surface with Negligible Hysteresis. *Langmuir*, 29(34):10785–10795, 2013.
- [123] E. D. Palik. *Handbook of Optical Constants of Solids*, volume 3. Academic Press, 1998.
- [124] J. Henrie, S. Kellis, S. Schultz, and A. Hawkins. Electronic Color Charts for Dielectric Films on Silicon. *Optics Express*, 12(7):1464–1469, 2004.
- [125] M. Pimenta, G. Dresselhaus, M. S. Dresselhaus, L. Cancado, A. Jorio, and R. Saito. Studying Disorder in Graphite-Based Systems by Raman Spectroscopy. *Physical Chemistry Chemical Physics*, 9(11):1276–1290, 2007.
- [126] M. Hanchak, M. Vangsness, L. Byrd, J. Ervin, and J. Jones. Profile Measurements of Thin Liquid Films Using Reflectometry. *Applied Physics Letters*, 103(21):211607, 2013.
- [127] B. Chichkov, C. Momma, S. Nolte, F. Von Alvensleben, and A. Tünnermann. Femtosecond, Picosecond and Nanosecond Laser Ablation of Solids. *Applied Physics A*, 63(2):109–115, 1996.
- [128] D. Von der Linde, K. Sokolowski-Tinten, and J. Bialkowski. Laser– Solid Interaction in the Femtosecond Time Regime. *Applied Surface Science*, 109:1–10, 1997.
- [129] W. Kern et al. Handbook of Semiconductor Wafer Cleaning Technology. *New Jersey: Noyes Publication*, pages 111–196, 1993.
- [130] T. Ferreira and W. Rasband. ImageJ User Guide: ImageJ/Fiji 1.46r. Available Online: <http://imagej.nih.gov/ij/docs/guide/index.html>, 2012.